

REPORT DOCUMENTATION PAGE			Form Approved OMB NO. 0704-0188		
<p>The public reporting burden for this collection of information is estimated to average 1 hour per response, including the time for reviewing instructions, searching existing data sources, gathering and maintaining the data needed, and completing and reviewing the collection of information. Send comments regarding this burden estimate or any other aspect of this collection of information, including suggestions for reducing this burden, to Washington Headquarters Services, Directorate for Information Operations and Reports, 1215 Jefferson Davis Highway, Suite 1204, Arlington VA, 22202-4302. Respondents should be aware that notwithstanding any other provision of law, no person shall be subject to any penalty for failing to comply with a collection of information if it does not display a currently valid OMB control number.</p> <p>PLEASE DO NOT RETURN YOUR FORM TO THE ABOVE ADDRESS.</p>					
1. REPORT DATE (DD-MM-YYYY) 08-06-2012		2. REPORT TYPE Final Report		3. DATES COVERED (From - To) 1-Oct-2005 - 30-Sep-2011	
4. TITLE AND SUBTITLE Next Generation Large Mode Area Fiber Technologies for High Power Fiber Laser Arrays			5a. CONTRACT NUMBER W911NF-05-1-0572		
			5b. GRANT NUMBER		
			5c. PROGRAM ELEMENT NUMBER 615097		
6. AUTHORS Almantas Galvanauskas, Stefan Heinemann, Peter Dragic			5d. PROJECT NUMBER		
			5e. TASK NUMBER		
			5f. WORK UNIT NUMBER		
7. PERFORMING ORGANIZATION NAMES AND ADDRESSES University of Michigan - Ann Arbor Regents of the University of Michigan 3003 S. State St Ann Arbor, MI 48109 -1274			8. PERFORMING ORGANIZATION REPORT NUMBER		
9. SPONSORING/MONITORING AGENCY NAME(S) AND ADDRESS(ES) U.S. Army Research Office P.O. Box 12211 Research Triangle Park, NC 27709-2211			10. SPONSOR/MONITOR'S ACRONYM(S) ARO		
			11. SPONSOR/MONITOR'S REPORT NUMBER(S) 48976-PH-HEL.1		
12. DISTRIBUTION AVAILABILITY STATEMENT Approved for Public Release; Distribution Unlimited					
13. SUPPLEMENTARY NOTES The views, opinions and/or findings contained in this report are those of the author(s) and should not be construed as an official Department of the Army position, policy or decision, unless so designated by other documentation.					
14. ABSTRACT This program has successfully accomplished its main objective in that large core single-mode Ge-doped and Yb-doped CCC fibers have been developed as a platform for monolithically-integrated building blocks (individual laser channels) of high power beam-combined fiber laser arrays. Robust single-mode performance of CCC fibers with core sizes of up to ~60µm has been rigorously demonstrated. Various CCC fiber based high power lasers have been also demonstrated, including 600W SBS-free single-frequency linearly-polarized cw fiber MOPA system, mJ					
15. SUBJECT TERMS large mode area fibers, chirally-coupled core fibers high power fiber lasers, high power beam-combined fiber laser arrays, Stimulated Brillouin Scattering suppression, high brightness pump diodes					
16. SECURITY CLASSIFICATION OF:			17. LIMITATION OF ABSTRACT UU	15. NUMBER OF PAGES	19a. NAME OF RESPONSIBLE PERSON Almantas Galvanauskas
a. REPORT UU	b. ABSTRACT UU	c. THIS PAGE UU			19b. TELEPHONE NUMBER 734-615-7166

Report Title

Next Generation Large Mode Area Fiber Technologies for High Power Fiber Laser Arrays

ABSTRACT

This program has successfully accomplished its main objective in that large core single-mode Ge-doped and Yb-doped CCC fibers have been developed as a platform for monolithically-integrated building blocks (individual laser channels) of high power beam-combined fiber laser arrays. Robust single-mode performance of CCC fibers with core sizes of up to ~60µm has been rigorously demonstrated. Various CCC fiber based high power lasers have been also demonstrated, including 600W SBS-free single-frequency linearly-polarized cw fiber MOPA system, mJ pulsed and high-power ultrashort-pulse CPA systems. Accurate numerical modeling tools for designing CCC structures have been developed. Fabrication of CCC fibers reached such a degree of maturity that they have become available commercially. Furthermore, this program resulted in a successful demonstration of SBS suppression in acoustic-guidance tailored fibers with up to 13dB SBS threshold increase, which to our knowledge constitutes one of the largest SBS suppression achieved to date. UUIC group also performed an extensive study of SBS gain coefficient magnitude and spectrum in a variety of fiber glass materials. This program has developed high brightness diode laser pumps, based on broad-stripe single-emitter diode arrays that are beam shaped using micro-optics and coupled into 100µm (up to 130W) or 200µm core (up to 700W) 0.2NA delivery fibers.

Enter List of papers submitted or published that acknowledge ARO support from the start of the project to the date of this printing. List the papers, including journal references, in the following categories:

(a) Papers published in peer-reviewed journals (N/A for none)

Received Paper

TOTAL:

Number of Papers published in peer-reviewed journals:

(b) Papers published in non-peer-reviewed journals (N/A for none)

Received Paper

TOTAL:

Number of Papers published in non peer-reviewed journals:

(c) Presentations

Number of Presentations: 0.00

Non Peer-Reviewed Conference Proceeding publications (other than abstracts):

Received Paper

TOTAL:

Number of Non Peer-Reviewed Conference Proceeding publications (other than abstracts):

Peer-Reviewed Conference Proceeding publications (other than abstracts):

Received Paper

TOTAL:

Number of Peer-Reviewed Conference Proceeding publications (other than abstracts):

(d) Manuscripts

Received Paper

TOTAL:

Number of Manuscripts:

Books

Received Paper

TOTAL:

Patents Submitted

Patents Awarded

Awards

Graduate Students

<u>NAME</u>	<u>PERCENT SUPPORTED</u>	Discipline
Chi-Hung Liu	0.90	
Ming-Yuan Cheng	0.80	
Kai-Hsiu Liao	0.90	
Craig Swan	0.90	
Matt Rever	0.30	
Xiuquan Ma	1.00	
Cheng Zhu	0.60	
Caglar Yavuz	1.00	
Hedge Ravi	1.00	
Tsai Wei	1.00	
Chao Zhang	0.75	
C.G. Carlson	1.00	
FTE Equivalent:	10.15	
Total Number:	12	

Names of Post Doctorates

<u>NAME</u>	<u>PERCENT SUPPORTED</u>
Guoqing Chang	1.00
Leo Siiman	0.30
Shenghong Huang	1.00
FTE Equivalent:	2.30
Total Number:	3

Names of Faculty Supported

<u>NAME</u>	<u>PERCENT SUPPORTED</u>	National Academy Member
Almantas Galvanauskas	0.10	
Herb Winful	0.10	
Natasha Litchinitser	0.25	
Peter Dragic	0.10	
FTE Equivalent:	0.55	
Total Number:	4	

Names of Under Graduate students supported

<u>NAME</u>	<u>PERCENT SUPPORTED</u>
FTE Equivalent:	
Total Number:	

Student Metrics

This section only applies to graduating undergraduates supported by this agreement in this reporting period

The number of undergraduates funded by this agreement who graduated during this period:	0.00
The number of undergraduates funded by this agreement who graduated during this period with a degree in science, mathematics, engineering, or technology fields:.....	0.00
The number of undergraduates funded by your agreement who graduated during this period and will continue to pursue a graduate or Ph.D. degree in science, mathematics, engineering, or technology fields:.....	0.00
Number of graduating undergraduates who achieved a 3.5 GPA to 4.0 (4.0 max scale):.....	0.00
Number of graduating undergraduates funded by a DoD funded Center of Excellence grant for Education, Research and Engineering:.....	0.00
The number of undergraduates funded by your agreement who graduated during this period and intend to work for the Department of Defense	0.00
The number of undergraduates funded by your agreement who graduated during this period and will receive scholarships or fellowships for further studies in science, mathematics, engineering or technology fields:	0.00

Names of Personnel receiving masters degrees

<u>NAME</u>	
Zack George	
Total Number:	1

Names of personnel receiving PHDs

<u>NAME</u>	
Chi-Hung Liu	
Ming-Yuan Cheng	
Kai-Hsiu Liao	
Craig Swan	
Matt Rever	
Xiuquan Ma	
Hedge Ravi	
Hedge Ravi	
Tsai Wei	
C.G. Carlson	
Total Number:	10

Names of other research staff

NAME

PERCENT_SUPPORTED

FTE Equivalent:

Total Number:

Sub Contractors (DD882)

Inventions (DD882)

Scientific Progress

Technology Transfer

**Next Generation Large Mode Area Fiber Technologies
for High Power Fiber Laser Arrays**

US Army Research Office grant W911NF0510572

FINAL REPORT

Submitted by

A. Galvanauskas, PI of the project, *University of Michigan*

Phone: (734)615-7166, Fax: (734)763-487, e-mail almantas@umich.edu

(Co-PIs of the project: H. Winful, *University of Michigan*, P. Dragic, *University of Illinois*, E. Honea, *Aculight Corporation*, S. Heinemann, *Fraunhofer USA*, B. Samson, *NUFERN*)

Foreword

This program was primarily concerned with demonstrating, exploring and developing large core fiber technology as a technological platform that would greatly facilitate power scaling of multi-kW fiber laser arrays. From the beginning of the program it was understood that main requirements for such fibers are the following: (i) large core sizes (for reducing nonlinearities at high power operation) with robust single transverse mode output, (ii) robust polarization at the output, (iii) increased SBS threshold, to facilitate high power narrow-linewidth (preferably below SBS bandwidth of ~ 40 MHz) operation of individual laser channels in coherently-combined arrays, (iv) suitability for monolithic integration (compatibility with splicing and coiled packaging) and, most importantly, compatibility with all-fiber pump coupling.

Technical approach was based on two key innovations: (i) chirally-coupled core (CCC) fiber geometry to achieve robust single-mode operation in large-core fibers which are compatible with standard fusion splicing and packaging procedures; and (ii) SBS suppression through tailoring acoustic-wave guidance and damping in optical fibers. This program also had developed high brightness diode laser pumps, based on broad-stripe single-emitter diode arrays that are beam shaped using micro-optics and coupled into $100\mu\text{m}$ or $200\mu\text{m}$ core 0.2NA delivery fibers.

As it is described in detail in this report, the key objective of the program has been successfully achieved in that we designed, fabricated and demonstrated robust single-mode (and robustly polarized) operation of very large core ($55\mu\text{m}$ - $64\mu\text{m}$ core diameter) CCC fibers. Further outcomes of the program include development of theoretical understanding of CCC structures, development of unique numerical tools that enabled accurate modeling of CCC fiber properties and thus were critical in successfully designing large-core CCC structures, development of CCC fiber fabrication techniques (this has been achieved with multiple custom-fiber manufacturers), initial commercialization of CCC fibers, and even initial demonstration of monolithic pump combiners and pigtailed isolators using CCC fibers. Sum of these outcomes establishes foundations of CCC fiber technology. This demonstrated $\sim 60\mu\text{m}$ diameter single-mode core fibers in all-glass and bending-compatible structures constitute the largest-core flexible fibers to date, which are superior to $40\mu\text{m}$ core flexible PCF LMA in terms of core size and suitability for integration and are superior to PCF rods in terms of integration and kW power scaling.

Furthermore, this program resulted in a successful demonstration of SBS suppression in acoustic-guidance tailored fibers with up to 13dB SBS threshold increase, which to our knowledge constitutes one of the largest SBS suppression achieved to date. UUIIC group also performed an extensive study of SBS gain coefficient magnitude and spectrum in a variety of fiber glass materials.

High brightness pump diode development by Fraunhofer USA for this program has always been at the forefront of the highest pump-diode brightness achieved in the field. The concept is based on using beam-shaping micro-optics to transform multiple beams from single-emitter arrays into a single beam, that is then coupled into a delivery fiber. This approach combines reliability of the telecom-grade pump diodes with the high-brightness format compatible with monolithic all-fiber pumping of multi-kW integrated fiber amplifier or laser modules. For example, the demonstrated modules with $700\text{W}/200\mu\text{m}/0.2\text{NA}$ delivery fibers enable up to $\sim 4\text{kW}$ pumping in 7x1:1 combiner geometry.

Table of Contents

Statement of the problem studied	3
Initial Objectives of the Project (stated at the project start)	3
Main overall accomplishments	3
Summary of the most important results	5
1. Chirally Coupled Core Fiber Technology	5
<i>Main Research Events During the Project</i>	5
<i>Large Core Single-Mode CCC Fibers</i>	7
<i>Polarization Properties of CCC fibers</i>	14
<i>Development of CCC Fiber Theoretical Description and Numerical Modeling Tools</i>	19
<i>CCC Fiber Fabrication Development and CCC Fiber Technology Commercialization, Demonstration of CCC Fiber Based Components for Monolithic Integration</i>	23
<i>Demonstration of ~600W SBS-free 35μm Core CCC Based Fiber MOPA System</i>	24
<i>Demonstration of Other Fiber Laser Systems Based on CCC Fibers</i>	33
<i>Other Functionalities in CCC Fibers: Demonstration of SRS-Suppression in CCC Fibers</i> ...	33
<i>Summary and Future Possibilities</i>	36
<i>References for Section 1</i>	39
2. Suppression of SBS in Optical Fibers and its Exploration	41
<i>Abstract/Executive Summary</i>	41
<i>Detailed Narrative</i>	42
A. <i>SBS</i>	42
B. <i>Other Work</i>	52
<i>References for Section 2</i>	54
3. High Brightness Pump Diode Development	58
Appendix A	64
I. <i>Additional Analysis and Derivation for Choosing the Helical Reference Frame in CCC Structure</i>	64
II. <i>Additional Analysis and Derivation for Analytical Expression of Eigenmodes in CCC Structure</i>	66
III. <i>Additional Analysis and Derivation of General Quasi-Phase-Matching (QPM) Conditions</i>	68
<i>References for Appendix A</i>	71

Statement of the problem studied

Initial Objectives of the Project (stated at the project start)

Development of new fiber technologies to enable multi-kW (1-kW to 10-kW) narrow-linewidth (<100-MHz) monolithic fiber lasers for use in beam-combined high-power fiber laser arrays:

- Development of Chirally-Coupled Core (CCC) fiber technology for single-mode fibers with core sizes $\gg 30\text{-}\mu\text{m}$. Such large-core single-mode fibers should be compatible with mode-distortion free splicing and compactly-coiled packaging thus establishing a new technological platform for monolithic and compact multi-kW all-fiber systems.
- Development of Brillouin scattering suppression techniques using engineered interactions between guided acoustic and optical waves in large-core fibers to enable narrow-linewidth operation at multi-kW power levels.
- Demonstration of 1-3-kW narrow-linewidth single-fiber systems using these new fiber technologies.

Main overall accomplishments of this program to date are:

- Established Chirally-Coupled-Core fiber technology with robust single-mode operation and with core sizes $\gg 30\mu\text{m}$:
 - a. Designed and fabricated Ge and Yb doped CCC fibers with core sizes up to $55\mu\text{m}$ - $64\mu\text{m}$.
 - b. Rigorously demonstrated robust single-mode operation for fibers with core sizes of $55\mu\text{m}$ and $60\mu\text{m}$.
 - c. Demonstrated linearly polarized output from these fibers, and demonstrated resilience of output polarization to external mechanical and thermal perturbations.
 - d. Developed accurate numerical modeling tools for designing and comprehensive theory for understanding of CCC fibers.
 - e. Demonstrated and developed CCC fiber fabrication techniques with the two independent commercial fiber manufacturers – NUFERN and NKT Photonics (Crystal Fibre). Other manufacturers have been able to fabricate commercial grade CCC fibers, but outside of this JTO MRI program. Manufacturing of CCC fiber reached commercially-viable yields with 100's of meters of CCC fiber per production run.
- Experimentally demonstrated various high power fiber laser systems based on CCC fiber platform, validating expected performance of these fibers at high powers and pulse energies:
 - f. Demonstrated up to $\sim 600\text{W}$ average power single-frequency cw SBS-free CCC fiber laser MOPA system
 - g. Demonstrated up to $140\text{W}/1\text{mJ}$ 10ns-pulsed CCC based fiber laser
 - h. Demonstrated 200W average power and 350fs duration ultrashort-pulse chirped-pulse amplification system based on CCC fibers.
- Explored SBS suppression techniques based on acoustic-wave and material-properties engineering in optical fibers. Experimentally demonstrated $\sim 12\text{dB}$ SBS suppression in $\sim 10\mu\text{m}$

mode-field-diameter core acoustically-engineered fibers (the highest SBS suppression ever demonstrated). Explored impact of fiber-material composition on SBS threshold.

- Developed high radiance single-emitter diode array systems for pumping high-power fiber laser systems. Up to 700W from 200 μ m/0.2NA delivery fiber has been demonstrated, constituting one of current state-of-the-art results for narrow spectral-bandwidth pump sources. 12 units have been delivered with total cumulative pumping power of ~4kW.

Based on the demonstrated success of the CCC fiber concept a spin-off company **Arbor Photonics, Inc.** has been established with the goal of commercializing CCC fiber based laser technology and thus expediting the transfer of this technology to practical use. Arbor Photonics is targeting development of high power pulsed and cw fiber laser systems and laser subsystems for a wide range of applications in industrial material processing, semiconductor and microelectronics laser processing, as well as defense applications.

Developed high-brightness pump diodes have been commercialized by VISOTEK/Fraunhofer USA.

Summary of the most important results

1. Chirally Coupled Core Fiber Technology

Main Research Events During the Project

Development of large-core fibers with robust single-mode performance was the cornerstone of this program. Therefore, it is very useful to review the sequence of the main research events in CCC fiber development during the program. This program started in late 2005 (October 2005). Initial progress was very rapid – we had successfully demonstrated single-mode 33 μm core Ge-doped and Yb-doped CCC fibers and CCC based fiber lasers during the first three year main period of the program. During the fourth year (2-year extension period) we had encountered unexpected challenges in that new phenomena occurring in CCC fibers were identified, which were difficult to include into any existing fiber modeling tool (or even any existing computational approach) in order to design larger-core CCC fibers. During Y5 we succeeded in developing completely new and unique numerical modeling tools (as well as the complete theory of CCC structures), which enabled us to design large-core CCC fibers with robust single-mode performance. A Y6 no-cost extension has been requested and granted by ARO to complete the fabrication and testing of these large-core designs, and successful fabrication and demonstration of robust single-mode performance of up to 60 μm core CCC fibers have been achieved during that year, successfully concluding the large-core CCC demonstration and development program. In more detail:

- We had fabricated the first $\sim 33\mu\text{m}$ core Ge-doped (passive) CCC fibers and demonstrated their robust single-mode performance in 2006 (Y1 of the program). The first CCC sample was fabricated in April 2006 by NUFERN and was operating robustly single-mode at $\sim 1550\text{nm}$. By October 2006 the first Ge-doped 33 μm core CCC operating robustly single-mode in Yb-doped $\sim 1\mu\text{m}$ wavelength range has been fabricated (NUFERN) and tested (University of Michigan).
- During 2007 (Y2 of the program) we had fabricated the first Yb-doped double-clad 33 μm core CCC fiber and demonstrated its single-mode operation at $\sim 1064\text{nm}$ (April 2007), as well as efficient operation as a laser and an amplifier with overall power and gain performance being the same as with conventional 30 μm core Yb-doped DC LMA fibers fabricated by NUFERN.
- During the rest of 2007 and 2008 (Y2 and Y3 of the program) we had built and tested a variety of cw, pulsed and femtosecond-pulse laser systems based on CCC fibers (University of Michigan). Additional runs by NUFERN of 33 μm core Yb-doped DC CCC fibers supported these multiple experiments. However, the geometry of only 250 μm diameter polymer-coated (NA = 0.45) double-clad fiber was limiting power scaling to up to $\sim 300\text{W}$ for cw and $\sim 200\text{W}$ for nanosecond-pulsed and femtosecond CCC based fiber lasers. The limitation was associated with (i) difficulty to couple sufficient pump power into such a small cladding/low NA with existing pump sources and (ii) burning the polymer coating at the highest pump powers due to limited cladding size as well. To overcome these difficulties the 33 μm core design was scaled-up to 39 μm core size (30 μm MFD) and two versions of Yb-doped double-clad fibers with (i) 400 μm diameter polymer (NA = 0.45) coating, and (ii) 260 μm diameter air-clad (NA = 0.6) were fabricated by Crystal Fibre (currently NKT Photonics). This enabled to further pursue one of the key program objectives of

power-scaling of single-frequency SBS-free fiber MOPA as a building block for fiber-laser arrays. In 2010 we demonstrated up to 511W from a single-frequency (line-width \ll SBS bandwidth) air-clad CCC fiber laser MOPA, which in 2011 was further scaled up to \sim 600W.

- We identified CCC modeling challenges after the first attempts to design and fabricate 50 μ m diameter CCC fibers in 2008. First 50 μ m core Yb-doped CCC with 4 side-cores was fabricated by Crystal Fibre in early 2008 (Y3 of the program). A different design of 50 μ m core Ge-doped CCC with a single side core was fabricated by NUFERN end of 2008 (Y4 of the program). Both CCC structures did not work as model predicted and, therefore, did not achieve single-mode operation in \sim 1 μ m wavelength range (although the single-side CCC was close to a single mode operation, producing a dual mode, with all other HOM suppressed). To determine the cause of discrepancy we devised a new CCC characterization approach using broad-band supercontinuum source, which by the end of 2008 – early 2009 (Y4 of the program) established that quasi-phase matching in CCC structures does occur, but at substantially larger number of wavelengths that it should have been according to the original CCC theory/model based on geometrical-only perturbations. We discovered that CCC performance was also strongly affected by the large linear and circular birefringence occurring in the small gap between the central and the side cores.
- The remainder of 2009 (Y4 and Y5 of the program) we devoted to develop a full understanding of CCC structures, which entailed a complete rework of the theory and the numerical modeling approach. The challenge was that none of the existing numerical approaches based on beam propagation could account for rotating linear and circular birefringence perturbations occurring in CCC fibers.
- The numerical model was developed by the end of 2009 – early 2010 (Y5 of the program). During Spring of 2010 we had calibrated this new model vs performance of multiple CCC fiber samples and designs (both Ge- and Yb-doped) that we possessed at that time from a variety of different fabrication runs and established an accurate agreement between the model and the actual experimentally-observed performance. After that (mid 2010 – Y5 of the program) we proceeded to design large-core CCC structures and encountered a design “bottleneck” in suppressing HOM at larger core sizes. We succeeded in overcoming this limitation at the end of 2010 by finding a new design solution in CCC geometry with multiple side cores.
- During year 2011 (a no-cost extension year of the program) we proceeded to fabricating the new large-core design with Crystal Fibre. We chose Crystal Fibre due to two factors: (i) their technological approach of stacking Yb-doped rods to produce well controlled and homogeneous cores of $>50\mu$ m in diameter, and (ii) our previous experience with them during Y4, that demonstrated their capability in achieving high precision in fiber-preform fabrication. In summer of 2011 different design variations of 50 μ m, 55 μ m and 60 μ m diameter Ge-doped core CCC fibers with 8 side-cores were successfully fabricated and experimentally demonstrated to perform robustly single-mode. This design then was reproduced in 55 μ m core Yb-doped triple-clad CCC fibers that were delivered to the University of Michigan in January 2012. Preliminary experiments with these Yb-doped 55 μ m core CCC fibers confirmed robust single-mode performance and successfully tested their use in fiber laser and amplifiers, thus completing the

primary objective of this program to demonstrate robustly single-mode fibers with core sizes $>>30\mu\text{m}$ of conventional LMA fibers.

Large Core Single-Mode CCC Fibers

By the conclusion of the program we have designed and fabricated a series of large-core Ge-doped and Yb-doped CCC fibers, which include $50\mu\text{m}$, $55\mu\text{m}$, $60\mu\text{m}$ and $64\mu\text{m}$ core fibers with different helix periods for exploring different design variations and their effect on single-mode performance. CCC fibers with Ge-doped cores have central-core NA = 0.068 and side core NA = 0.088, and different helix periods in the range from 5mm to 6.3mm. Fabricated Yb-doped CCC fibers are based on the identified the best Ge-doped design and have core size of $55\mu\text{m}$ with NA = 0.072 and side-core NA = 0.088 and helix period of 5.3mm. For facilitating high-power pumping these Yb-doped CCC fibers have an octagonally-shaped triple-clad structure with all-glass inner cladding of $330\mu\text{m}$ diameter and NA = 0.22, and an outer $390\mu\text{m}$ cladding with polymer coating and NA = 0.45. Using rigorous modal characterization methods we demonstrated robust single-mode operation in $\sim 1\mu\text{m}$ Yb-doped fiber range of all $55\mu\text{m}$, $60\mu\text{m}$ core fibers and with lengths of only $\sim 1.5\text{m}$. Some of tested $50\mu\text{m}$ core experimental design variations were also performing single-mode, but only at lengths longer than $\sim 2\text{m}$. In addition, CCC fiber with a core diameter of $64\mu\text{m}$ has been shown to operate robustly single-mode at $\sim 1.4\mu\text{m}$ wavelengths, indicating potential of CCC large-core fibers of operating single-mode in different wavelength ranges. An example of a cross section of a Ge-doped $60\mu\text{m}$ core CCC and its comparison to conventional $125\mu\text{m}$ telecom-grade single-mode fiber is shown in Fig. 1(a), and cross section of $55\mu\text{m}$ core triple-clad Yb-doped fiber is shown in Fig. 1(b). For these large cores a balanced design of CCC structures with 8 identical helix-side cores has been chosen, shown in this figure. Increase of side core number allowed to overcome core-size scaling limitations of a single-side design and to significantly relax fabrication tolerances. For example, single-side designs require center-to-side separation to be rather small of $\sim 2\mu\text{m}$ to $3\mu\text{m}$. With multiple side-core designs we relaxed this tolerance to $5\mu\text{m}$ - $10\mu\text{m}$, thus substantially facilitating fabrication process. Dramatic improvement in performance occurs due to the substantial increase in the number of available leaky side-core modes that extract HOM from the central core. We have identified that in a single-side core design a certain “bottleneck” occurs in that all HOM of the central core are coupled into the same side-core mode. This can result in back-coupling of some of the power back from the side-core mode into HOM of the central core thus saturating the HOM suppression. Increasing size of the central core leads to increasing HOM number and, therefore, this “bottleneck” becomes increasingly pronounced. We identified a design solution to this problem. By introducing multiple side cores we discovered that this bottleneck can be effectively removed by providing a multitude of independent parallel channels for the central-core HOM to leak-out through the side core modes into the cladding.

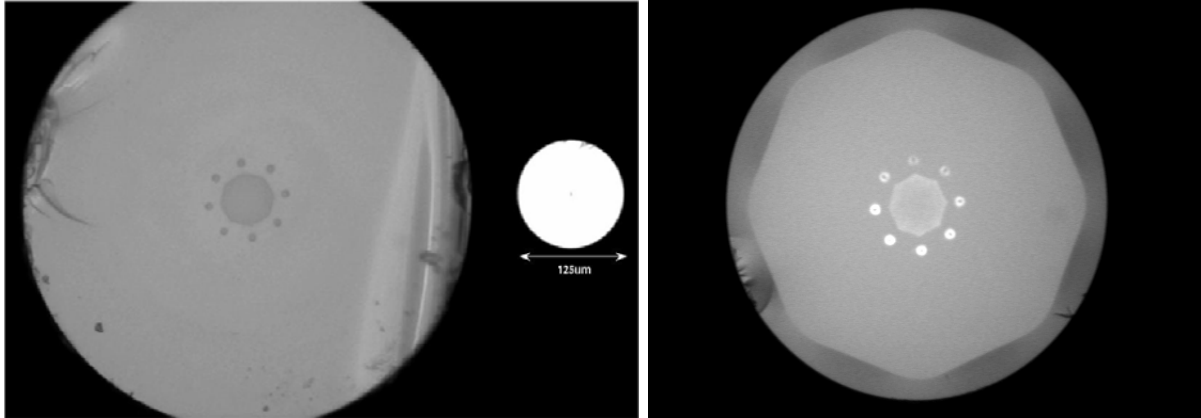


Fig. 1. (a) Cross-section of 60 μm -core CCC fiber (left-hand image) and comparison to a standard 125 μm clad single-mode fiber (right-hand image). (b) Cross-section of 55 μm core Yb-doped triple-clad fiber. The structure has inner all-glass (fluorine-doped silica) cladding with 0.22NA, and outer fluoro-acrylate polymer cladding with 0.45NA.

Rigorous characterization of single-mode performance was a critically important part of the technology demonstration. Indeed, it is appropriate here to emphasize, that our objective was not only to increase the core size, but to achieve that while preserving pure and robust single-mode operation in a fiber which is completely compatible with monolithic integration, as expressed in fiber all-glass structure suitable for standard laser fusion techniques and fiber flexibility due to large NA of the central core to maintain fiber packaging advantages. Characteristically, our modal characterization did not rely on M^2 measurements of the fiber output beam, since it is well understood by now [1] that such beam-quality measurement is ambiguous with respect to single-mode performance of a fiber and cannot be used as a criterion defining single-mode performance. Instead we based our CCC fiber modal characterization on so-called Spatially and Spectrally (S^2) Resolved measurements, originally developed by OFS [2]. We used this approach in two different ways. First, we used broad-band spatially resolved spectral observation using Optical Spectrum Analyzer (OSA) to *qualitatively* determine degree of single mode performance, by observing presence or absence of spectral beating patterns. Absence of beating patterns indicates the pure single-mode performance, while presence of beating patterns indicates presence of higher-order modes at the fiber output [2, 3], as described in more detail below. Second, using S^2 measurements we could *quantitatively* measure the HOM content at the fiber output, thus providing with a solid reference for comparing performance of different fibers. For example we could compare performance of a large-core CCC with that of a standard LMA, as described in more detail further in the text.

Measurement setup for this modal-content characterization is shown in Fig. 2. Details of the setup are given in the figure caption. For modal characterization in Yb-doped fiber gain wavelength-range we used a single-mode fiber broad-band ASE source, with output from a standard single-mode fiber. Spatially and Spectrally Resolved measurements were performed at the test-fiber output with a standard (MFD = 6.2 μm at $\sim 1\mu\text{m}$) single-mode fiber, connected to an OSA. As is shown in the Fig. 2, we could achieve

variable mode-mismatched excitation at the test-fiber input and we could also sample across complete beam at the test-fiber output.

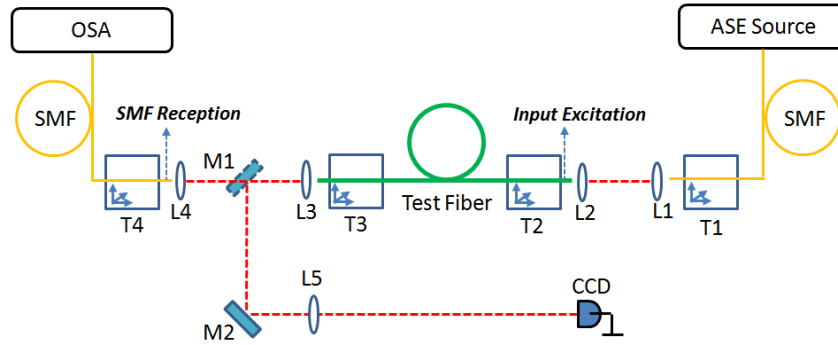


Fig. 2. Setup for modal beating and S^2 measurements used to *qualitatively* and *quantitatively* characterize modal content at the output of the test fiber. Broadband ASE source is launched through SMF into the test fiber at “Input Excitation”, where the modal excitation can be adjusted by translation stages T1 and T2. Another SMF is used to receive the beam coming out of the test fiber at the position of “SMF Reception”, so T3 and T4 can adjust the SMF to sample different parts of the beam. By adding an automatic 2-dimensional scan on T4, this setup can perform S^2 measurements. Flip mirror M1 and mirror M2 with the focusing lens L5 are used to record the near field image of the output beam with the CCD camera. L1, L2, L3, L4, L5 are lenses. OSA is a computer-controlled optical spectrum analyzer which receives the broadband signal captured by the SMF on T4 and then transfers data to a computer, for further quantitative analysis.

Qualitative demonstration of a pure SM output from a 55 μm core Ge-doped CCC fiber is shown in Fig. 3(b). This demonstration used a single-mode fiber as a spatial filter for sampling different portions of the test-fiber output beam. For this purpose output beam was deliberately focused to a spot much larger than single-mode fiber MFD of 6.2 μm . For reference, we also used a standard 20 μm LMA fiber as a reference-test fiber. This LMA is currently an industrial standard for monolithic commercial systems [4, 5]. Measured modal performance of this reference fiber is shown in Fig. 3(a). Both tested samples were of equal length of 1.5m. Structure parameters of the tested two samples are the following:

- 20 μm core Ge-doped LMA with core NA = 0.065. MFD is 18 μm and the core is dual-mode (supports LP_{01} and LP_{11} modes).
- 55 μm core Ge-doped CCC with core NA = 0.068. MFD is 42 μm and the central core would support 17 modes, if there would be no side cores.

Details of the measurement are given in the figure caption. The test result is apparent here, indicating that standard 20 μm LMA fiber output, even when its input excitation is optimized for a fundamental mode throughput, does contain traces of the only higher-order mode that this fiber supports. In contrast, 55 μm core CCC test shows that when its input is optimized for maximum transmission, no higher-order modal content is observable for this length, despite the fact that the central-core nominally should support 17 modes.

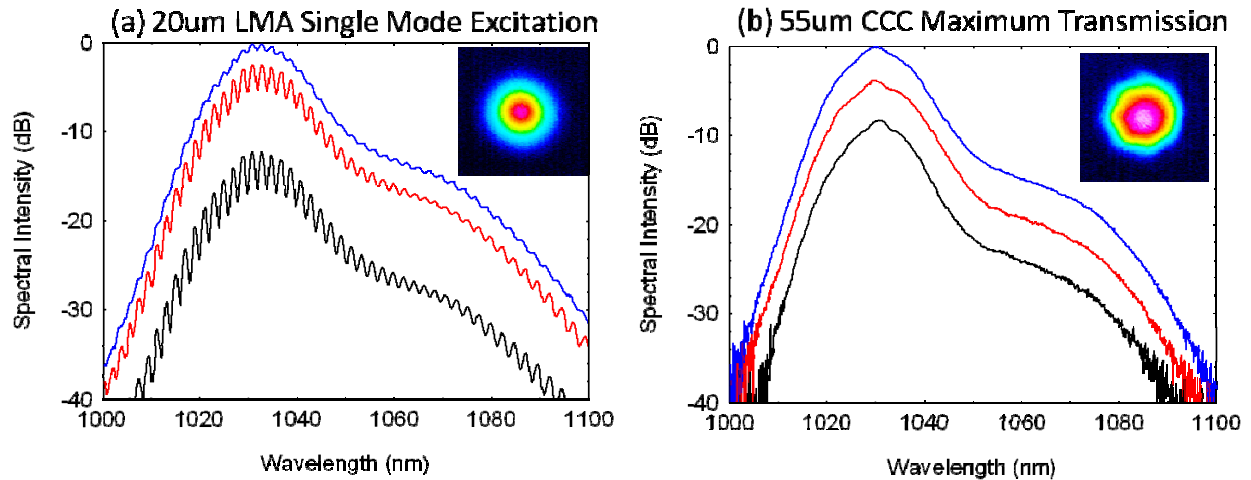


Fig. 3. Performance comparison between industry-standard 20µm LMA fiber and 55µm CCC fiber under 50cm diameter loosely coiled condition. A 6.2µm mode field diameter SMF is used to receive light at different parts of a beam with around 40µm mode field diameter for both 20µm LMA fiber under single-mode excitation condition and 55µm CCC fiber under maximum transmission input-excitation conditions. Blue curve corresponds to the signal received by the SMF at the peak center of the beam profile. Red curve corresponds to the signal received by the SMF at intensity -3dB down position comparing to the peak center of the beam profile, and the black curve corresponds to the intensity -10dB down position. (a) Transmission spectrum of 20µm LMA fiber at different parts of the beam profile. It shows the further away from the peak center of the beam profile, the more pronounced spectral beating observed, which is consistent with the fact that the fundamental mode has more distribution in the center whereas the HOM have more distribution in the wings of the modal profile. (b) Despite slightly octagonal shape of the 55µm CCC fiber output modal profile defined by the octagonal shape of the fabricated central core, there are no observable modal beatings across the entire beam profile, which means it is a pure single mode beam.

Qualitative demonstration of robustness of single-mode output from the same sample of 55 µm core CCC fiber is shown in Fig. 4(b), where broad-band transmission through a 1.5 m long CCC fiber piece is measured for 4 different input misalignment positions. For comparison, Fig. 4(a) shows the same test performed with the same sample of 1.5 m long standard 20 µm-core LMA fiber. Fig. 4(a) clearly shows excitation-dependent spectral “beating”, which is caused by modal interference in the LMA core. Fig. 4(b) clearly shows complete absence of such spectral beating in a CCC fiber at all input-misalignments, hence indicating robust single-mode content of the tested CCC fiber sample.

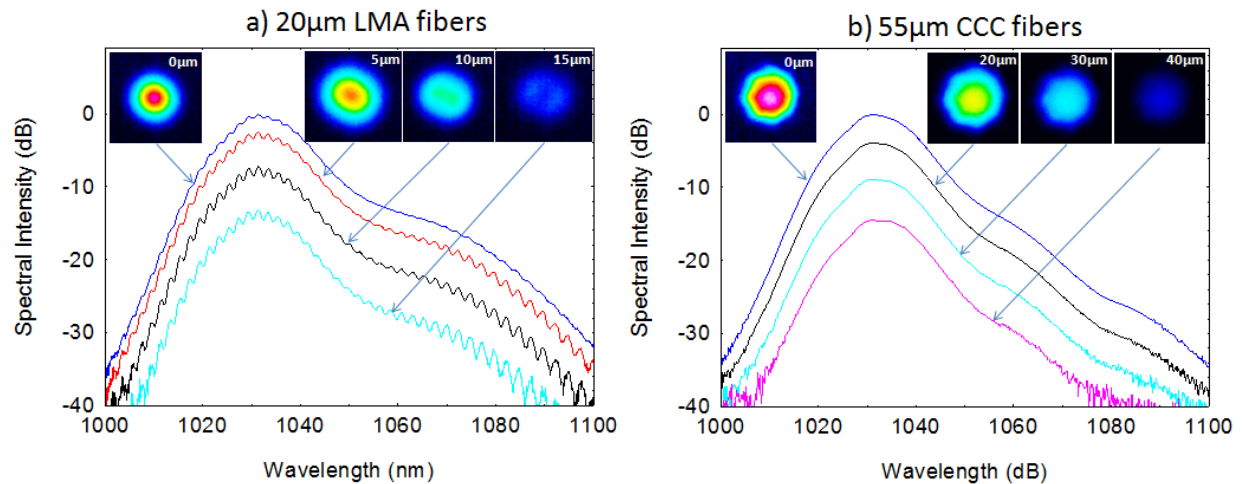


Fig. 4. Experimental demonstration of robust effectively-single-mode output from 1.5 m long 55 μm core CCC fiber. Figure (b) shows broad band spectra measured for four three different misalignment positions (relative transverse positions of the fiber input) of the CCC fiber. Figure (a) shows the same test performed with a 1.5m long 20 μm core LMA fiber. Spectra are measured with a single-mode fiber monitor placed after each fiber, which is spatially filtering the output beam and therefore can detect modal interference. Absence of modal interference in the 55 μm core CCC fiber is evident, despite the fact that its core size supports 17 modes. In contrast 20 μm core LMA fiber which has only two transverse modes shows presence of both transverse modes, strongly depending on the excitation conditions.

Quantitative characterization of 55 μm core CCC fiber modal performance and its comparison to that of the 20 μm LMA is shown in Fig. 5. Fig. 5(a) shows result of S^2 measurement for 3 meter long 20 μm LMA fiber at optimum single-mode excitation. After S^2 calculation and calibration, it shows approximately -16dB of LP_{11} modal content. Fig. 5 (b) shows output beam intensity distribution for the same 20 μm core LMA fiber with its input misaligned so that -3dB lower power is observed through a SM “sampling” fiber at the output of the test fiber (see the experimental arrangement in Fig. 2). In this case this -3dB misalignment for LMA fiber produces multimode output with 45% LP_{01} and 55% LP_{11} content (estimated by using profile fitting), which is too large for S^2 algorithm to work accurately. Fig. 5 (c) shows S^2 measurement for \sim 1.5m long 55 μm core CCC fiber, with no HOM content observable above the -20dB noise floor obtained after calibration of this particular measurement. Fig. 5 (d) shows S^2 measurement for the same 55 μm CCC fiber sample with input misaligned at -3dB power transmission compared with the maximum transmission, which means \sim 50% HOM excitation at the input is ensured. Nevertheless, fiber output still has no observable HOM content above the measurement -20dB noise floor. For these measurements CCC fiber is coiled to 50cm diameter, but coiling to 30cm diameter or keeping fiber straight produces identical results. The important conclusion here is that this S^2 measurement clearly shows that this 55 μm core CCC fiber passes TIA-455-80-C Industrial Standard for SM operation [6] which requires that HOM content at the fiber output would be below -20dB level, i.e. this large core fiber is single-mode according to the industry-accepted definition.

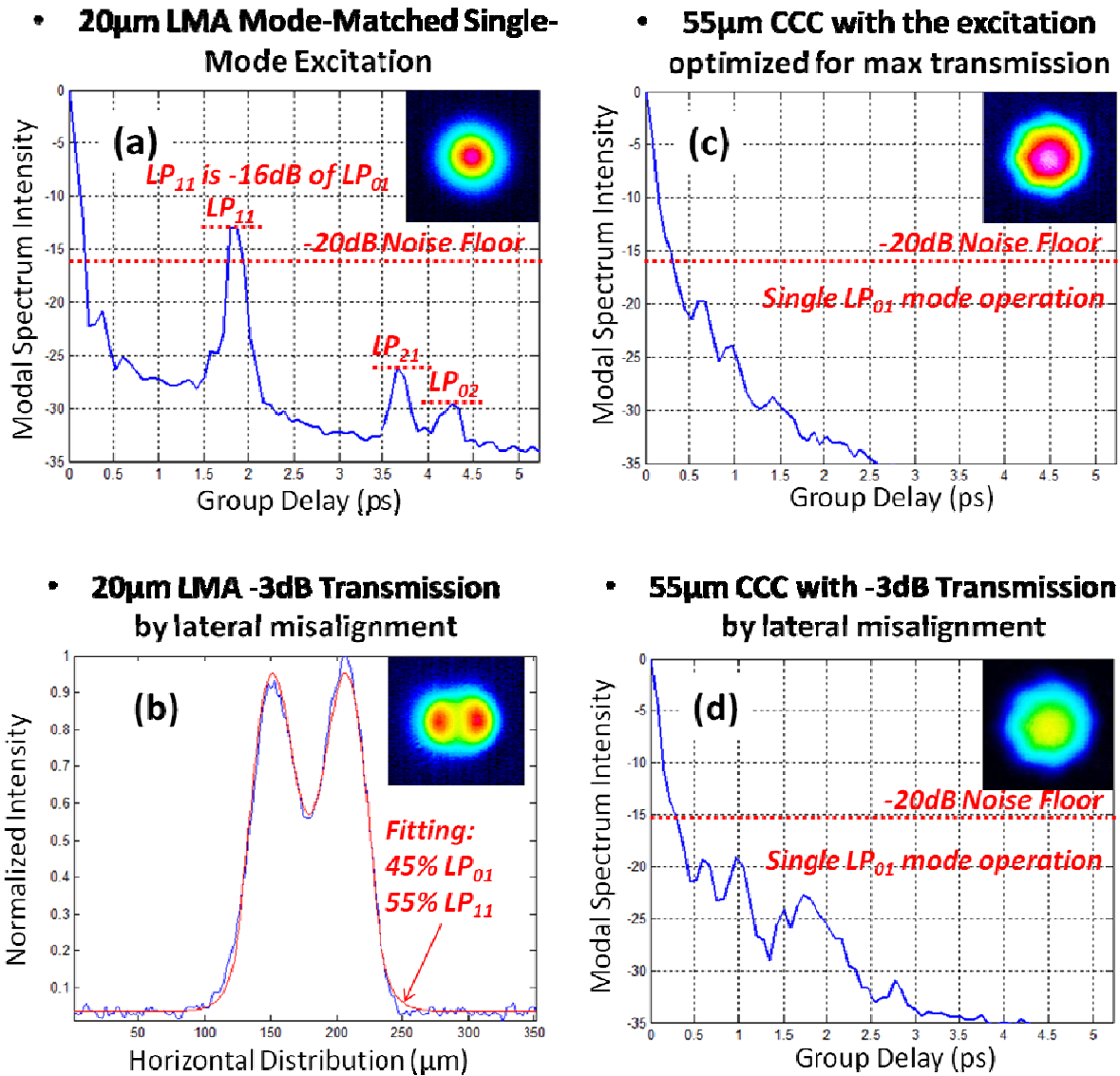


Fig. 5. Quantitative comparison between 20 μ m LMA fiber and 55 μ m CCC fiber. (a) Fourier transform of the beating spectrum obtained for the S^2 measurement of 3 meter long 20 μ m LMA fiber under the condition of single mode excitation. After the specific algorithm to extract the relative modal ratio and calibration of the imaging system, the peak of LP_{11} mode is calculated to be -16dB relative to the fundamental mode. (b) For the 20 μ m LMA fiber with -3dB down transmission through the “sampling” SM fiber at the test-fiber output, too much HOM content gets excited that the S^2 measurement would fail, so we use fitting method to determine the relative mode ratio in such a beam. The least square fitting method has shown excellent fitting to the beam profile, which gives around 55% power in LP_{11} mode and only 45% in fundamental mode. (c) Fourier transform of the beating spectrum obtained for the S^2 measurement of \sim 1.5m long 55 μ m CCC fiber under the condition of maximum transmission. There are no HOM peaks observed above -20dB noise floor, which is determined by the OSA sensitivity

and signal power captured by the SM fiber. (d) Fourier transform of the beating spectrum obtained for the S^2 measurement of the same 55 μm CCC fiber sample under the condition of -3dB transmission comparing with the maximum transmission condition. There are no HOM peaks observed above -20dB noise floor, which indicates strong HOM suppression through this ~ 1.5 meter long CCC fiber and single-mode output even for this strongly misaligned excitation, where at least 50% of power is expected to be in the HOM. For (c) and (d) measurements CCC fiber is coiled to 50cm diameter, but the same measurements performed with CCC fiber coiled to 30cm diameter or keeping the CCC fiber straight produces identical results.

The impact of this demonstrated single-mode performance at these large core sizes is summarized in Fig. 6, where current technological limitations of conventional and PCF LMA fibers is shown for reference. As it is shown in this figure, all existing monolithically-integrated commercial high power fiber lasers are based on conventional LMA fibers with core sizes not exceeding approximately 25 μm in diameter. The limitation is primarily associated with the fact that increasing LMA core size leads to progressively higher scattering between fundamental and higher-order modes (HOM) through a splice between two LMA fibers or through a processed LMA fiber component such as pump combiner. Consequently, it becomes increasingly difficult to maintain diffraction-limited output from an integrated LMA fiber system, although conventional LMA fibers with larger cores are used in free-space pumping configurations. PCF LMA fibers, although can provide with much larger cores, but have the technological limitations that make it challenging to use PCF fibers for monolithically-integrated lasers. Currently CCC fibers provide with robustly single-mode performance at core sizes achievable only with PCF rods, but CCC fibers are well suited for monolithic integration since they can be spliced using standard splicing equipment and can be coiled for packaging, since their HOM suppression properties are not sensitive to loose (30cm – 50cm diameter) coiling.

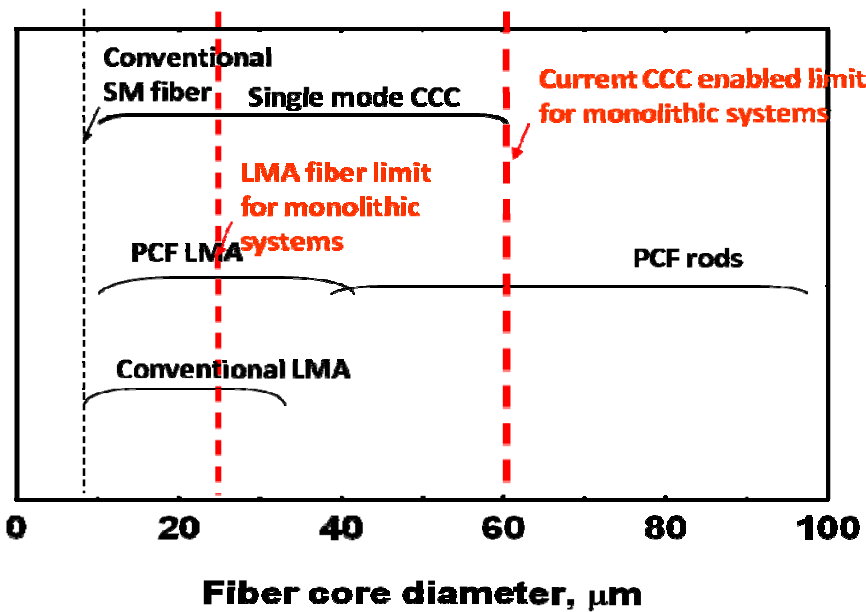


Fig. 6. Potential impact of currently achieved robustly single-mode 55 μm -60 μm core CCC fibers for integrated high power laser systems.

Polarization Properties of CCC fibers

Polarization properties of all successful designs of single-mode CCC fibers have been systematically investigated and it was discovered that all the tested fibers possess excellent polarization preservation properties. This discovery was much unexpected since all fabricated CCC fibers possess no strong intrinsic birefringence. Indeed, rapid spinning of the CCC fiber perform during its manufacturing process used to achieve short helix periods of only few-mm in effect “deletes” any residual weak birefringence [7] in the fiber that might otherwise been “frozen” in it during the fabrication. Example of polarization characterization of a 4m long piece of 60 μ m core CCC fiber is presented in Fig. 7, which shows polarization extinction at the fiber output measured as a function of $\lambda/2$ wave-plate angle at the fiber input. Experimental measurement configuration is shown on the right side of the figure. Two PER peaks of >20dB, correspond to the input polarizations parallel and perpendicular to the fiber coiling plane (which was in the plane of the optical table). Fiber was coiled to 50cm diameter. This measurement indicates presence of weak coiling-induced birefringence (on the order of 10^{-6}). Such weak birefringence could not be observed in a fiber with built-in locally-varying random varying thermal-stress produced birefringence usually imprinted in unspun fibers during fiber draw process. This shows that CCC fiber spinning during their draw removes any such locally-varying thermal stress effects and CCC fibers indeed posses robust low birefringence. This is further confirmed by PER measurements in CCC fiber samples that are kept straight, which show that output PER is high irrespective to any input polarization orientation, consistent with low birefringence fibers.

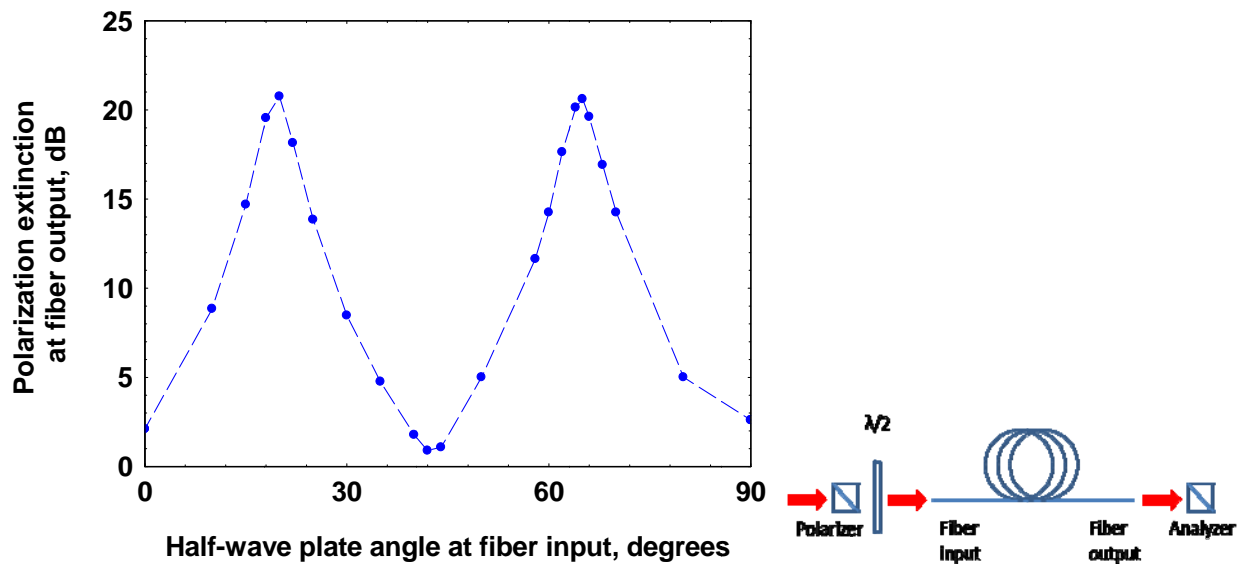


Fig. 7. Polarization extinction at the output of 4m long 60 μ m core CCC fiber as a function of the half-wave plate orientation at the test-fiber input. Experimental measurement setup is shown on the right. Polarization at the fiber output reaches two PER peaks of >20dB, separated from each other by 45° rotation of the input $\lambda/2$ waveplate. In the setup these two waveplate orientations corresponded to horizontal and vertical polarizations, with respect to the optical table surface, which was parallel to the CCC fiber coiling plane. Fiber coiling diameter was 50cm.

Most important result was that CCC fibers have shown very robust polarization output, which was impervious to external perturbations, such as external pressure or temperature variations (both locally or globally in the fiber). This has been particularly thoroughly characterized by Arbor Photonics, a company that has been spun-off from the University of Michigan to commercialize laser systems based on CCC fibers. The systematic experimental study of perturbation-insensitive performance of 35 μm core CCC fibers has been published in a joint publication between Arbor Photonics and University of Michigan in SPIE Photonics-West 2011 Conference Proceedings [8]. Here is the summary of the main findings.

The experimental setup used to make PER measurements is shown in Fig. 8. Linearly polarized light with a PER > 20 dB and center wavelength of 1053 nm was coupled into the fiber under test. The $\lambda/2$ waveplate at the input end was used to rotate the incident linear polarization state. Measurement of transmitted polarization state was made by rotating a thin film polarizer to obtain a maximum and minimum transmitted power as measured on the power meter. PER was then calculated using the following formula: $dB = 10 * \log_{10}(P_{max}/P_{min})$. The metal plate under the fiber was used to adjust the fiber temperature in order to evaluate the sensitivity of the fiber's polarization performance to temperature.

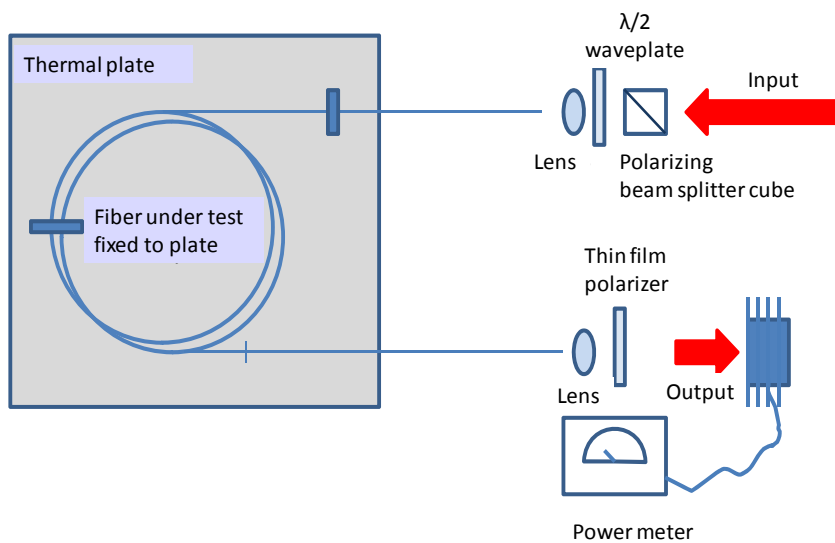


Fig. 8. Experimental arrangement for measuring PER at the output of a fiber under test.

Testing was performed on two different optical fibers: the first was a Yb-doped CCC fiber with a mode field diameter of 21 μm and a length of ~ 4 m; the second was a high-birefringence LMA fiber with a similar mode field diameter and length of ~ 1.5 m. In each case, the fiber was coiled in loops with ~ 30 cm diameter and placed upon a copper plate that was heated from room temperature of ~ 20 $^{\circ}\text{C}$ to a maximum temperature of 70 $^{\circ}\text{C}$.

The most extensive testing was performed on 30 μm core/250 μm clad CCC optical fiber. First, PER versus incident angle was measured for loops of 2 different diameters: 50 cm and 30 cm. Data from

those tests (Fig. 9) show that both conditions provide highest extinction ratio at 2 distinct incident angles, which correspond to the plane of the loops (horizontal) and perpendicular to the loops (vertical). The phase offset can be explained by imperfect registration of the waveplates, and by the fact that care was not taken to ensure that the fiber path between the input/output coupling stages and the thermal plate remained in a single plane. The geometric path of the fiber through space can cause a mode's polarization to rotate. This effect is purely geometric and is not a result of bend-induced stresses. The PER of the fiber is lowered when the polarization of the mode in the coiled section is not aligned parallel or perpendicular to the coil axis. Bend-induced birefringence causes the fiber coil to act as a low-order waveplate and alter polarization states that are not aligned along the slow or fast axis. The bend-induced birefringence increases proportional to $1/R^2$, so that the 30 cm coil has higher birefringence and a lower PER at the curve minimum. .

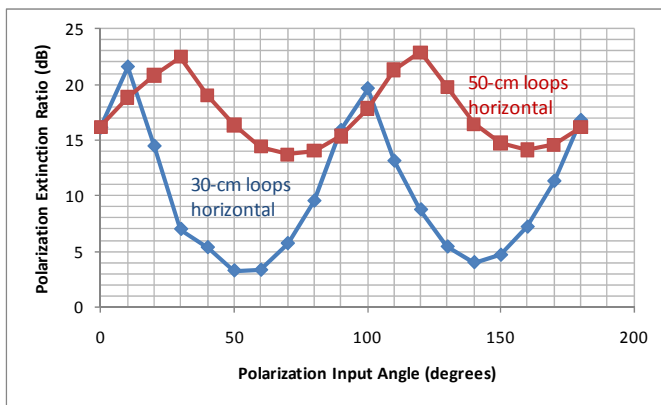


Fig. 9. PER vs input polarization state through CCC optical fiber. The data was taken with 2 different loop diameters.

The PER was remarkably stable with respect to mechanical perturbations. Significant localized pressure on the fiber had no measurable effect on the PER as did in-plane shuffling of the fiber coils. The coils could even be moved out-of-plane. The PER from the fiber coil was monitored as one 50 cm loop of the coil was raised from resting horizontally on the thermal plate to a vertical position. A minimum PER of 13 dB was measured for a 45 degree loop orientation. The PER recovered to ~20 dB as this loop was rotated to a vertical position. Note that the polarization analyzer and input polarization state remained fixed during this test.

In a typical fiber amplifier, the fiber is fixed and coiled over most of its extent, but also contains segments that are pigtails to components. These segments may follow some arbitrary path through the packaging with some ability to shift within a confined space. The above tests indicate that when packaged in such a manner, CCC fiber is sufficiently robust to mechanical perturbations that it will maintain a fixed linear polarization for the amplifier's output.

Tests to examine the PER stability over temperature were also performed. The plate was heated and a piece of foam was placed over the fiber loops to keep the temperature constant. The input $\lambda/2$ waveplate was set to the position with the highest PER and left in that position for the duration of the

test. The output thin film polarizer was set alternately to the positions for maximum and minimum transmission that were found at room temperature. The temperature range investigated was 20 – 70 °C.

The results shown in Figure 10 reveal that the PER was extremely robust, remaining above 20dB for all test conditions. It is worth repeating that during data collection, the angle on the thin film polarizer that was set for maximum and minimum power remained the same for each data point. This means that the polarization did not rotate.

Linear PER vs. Temperature

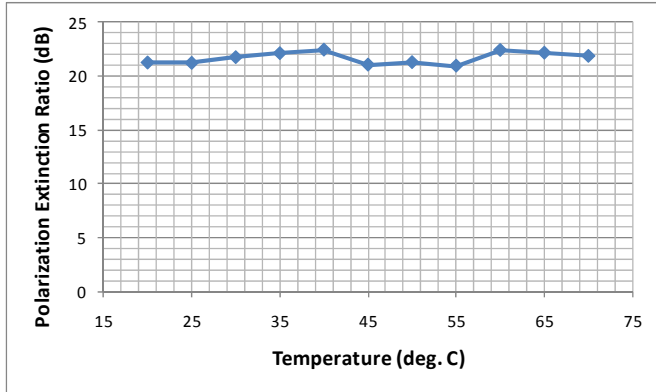


Fig. 10. As linearly polarized light is launched into a 4 meter length of coiled CCC fiber, the polarization state of transmitted light was monitored while the fiber was heated from 20°C to 70°C.

To further investigate the stability of the PER with temperature, localized thermal tests were performed by heating a short length (10 cm) of CCC fiber loops to a plate temperature of 50 °C. The amount of fiber exposed to the increased temperature was about 7% of the total fiber length. The PER remained fixed unchanged during this test, underscoring the exceptional stability of CCC fiber polarization maintaining performance.

Finally, polarization transmission of PM LMA with 25 μm core and 250 μm cladding and a length of 1.5 m was investigated as a comparison to CCC fiber. The experimental layout is the same as used for the CCC fiber tests (Figure 8). In order to produce single-mode injection from the free-space setup, a piece of passive CCC fiber with similar mode field diameter was spliced to the input end of the PM LMA. With this compound fiber setup, ~ 19.5 dB of PER was measured along one axis and ~ 23.5 dB on the other axis of the PM fiber at room temperature. Fig. 11 shows PER vs input polarization angle for the axis with 23.5 dB extinction.

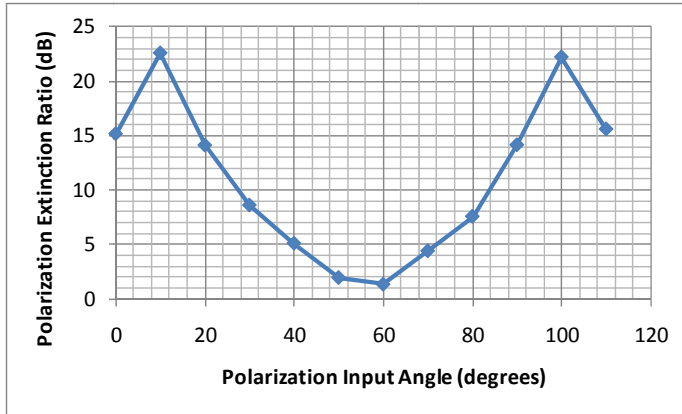


Fig. 11. PER output of PM LMA fiber at room temperature.

The PER of the PM LMA as the plate temperature is varied is graphed in Fig. 12, along with results from the CCC fiber (included for comparison). The PER data in the graph was taken with the thin film polarizer set to the positions for maximum and minimum transmission found at room temperature. The PER degraded as the temperature was raised. To determine if the polarization remained linear, the analyzer was also adjusted at each temperature to find maximum and minimum transmission. High PER could be recovered, which indicates that the output polarization remained linear but with a rotated orientation. The angles next to each data point on the PM LMA curve in Fig. 12 specify the amount that the analyzer was rotated to achieve the highest PER.

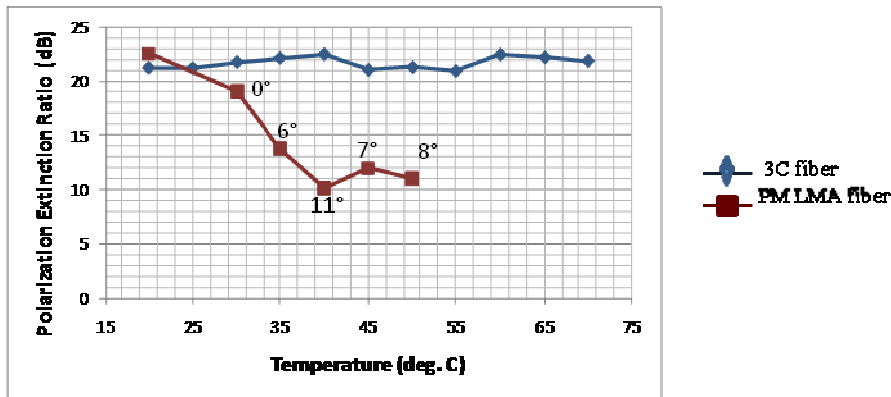


Fig. 12. Graph comparing the measured stability of the output polarization over a broad temperature range for CCC and standard PM LMA fibers.

These results indicate that the polarization state of the light from a PM LMA fiber does not stay constant, but can vary with temperature changes as small as 12 °C, even if the state of the input polarization and the fiber axis remain fixed.

This shows that CCC fibers have indeed very good polarization preservation properties, which, surprisingly, are more temperature stable compared to the measured temperature sensitivity of standard PM fibers based on thermal-expansion stress-rod produced high birefringence in an optical fiber. We believe that this polarization robustness of CCC fibers is primarily associated with the fact that

when random and strong thermal-stress produced local random-birefringence regions produced by fiber draw are effectively “deleted” by the rapid twist of the fiber during its draw, resulting homogeneous and isotropic fiber exhibits low sensitivity to external perturbations, due to the absence of these internal random birefringence perturbations. Also, the fact that CCC core is robustly single-mode helps polarization stability of the propagating beam in such a core.

Indeed we had tested CCC fiber polarization preservation under high power conditions and have shown that even at the tested powers of few hundred watts this polarization robustness is still maintained, as shown in the section further in the report which details high-power SBS-free single-frequency work with CCC fiber MOPA.

Development of CCC Fiber Theoretical Description and Numerical Modeling Tools

The critically important result of the program, which had eventually led to the success in demonstrating large-core single-mode CCC fibers, was the development of the fundamental theoretical understanding of the CCC fiber structures and, more importantly, the development of unique numerical methods for correctly and accurately simulating CCC fiber performance.

Main functionality of CCC structure is based on engineering properly modal interactions between center-core and side-core/cores modes. Challenge in describing modal interactions in CCC structure is primarily associated with the fact that side core is rotating along the central core, i.e. is not axial-coordinate invariant. Consequent, to address this difficulty we developed a theoretical approach based on using Maxwell’s Equations in Helical reference frame. In this helical frame CCC structure becomes in effect “unwound”, i.e. represented by straight center and side cores, thus allowing using conventional coupled-mode methods to deal with inter-core modal coupling in CCC fibers. Indeed, in this reference frame Maxwell’s equations can be expressed in a mathematical form identical to that in Cartesian coordinates, and the only difference between the two descriptions is solely captured by the transformed dielectric permittivity and magnetic permeability tensors expressed in this helical frame [9, 10]. For example, a conventional cylindrically-symmetric step-index fiber, which is piece-wise homogeneous and isotropic in Cartesian coordinates, in helical coordinates is described by inhomogeneous and anisotropic permittivity and permeability tensors [10]. Following this approach, we can obtain the eigenmodes of this CCC structure, and further solve for the exact QPM resonances. For abbreviation, we summarize the conclusion here, and detailed analysis can be found in the Appendix A. First, as has been pointed out, since the eigenmodes of this CCC structure must be symmetric with respect to helical translation, the modal fields are azimuthally invariant: most of them are circularly-polarized (i.e. characterized by spin angular momentum) optical-vortex (i.e. characterized by orbital angular momentum) modal fields, which has been confirmed rigorously by solving for the modal electric field in the helical reference frame. Second, in CCC fibers, the general phase matching condition between a central-core mode group $LP_{l_1 m_1}$ and side-core mode group $LP_{l_2 m_2}$ (see Appendix A) can be expressed as:

$$\beta_{l_1 m_1} - \beta_{l_2 m_2} \cdot \sqrt{1 + K^2 R^2} - \Delta m \cdot K = 0 \quad (1)$$

Here, $\beta_{l_1 m_1}$ and $\beta_{l_2 m_2}$ are the propagation constants of $LP_{l_1 m_1}$ and $LP_{l_2 m_2}$ in straight cores, and $\sqrt{1 + K^2 R^2}$ is a helical correction factor. The parameter Δm follows $\Delta m = \Delta l + \Delta s$: the values of Δl run through four possible modal number combinations $\Delta l = \pm l_1 \pm l_2$, and the values of Δs run through five numerical values $\Delta s = -2, -1, 0, +1, \text{ and } +2$. This equation gives the resonance positions (vertical dash lines) in Fig. 13-b which are explained in more detail below.

Fig. 13 presents the detailed comparison between CCC fiber theory, numerically simulated performance and experimental characterization, indicating very good agreement between them. In Fig. 13-a, wavelength-dependent loss for side-core LP_{11} and LP_{21} modes due to the frustration of the total internal reflection in a curved waveguide [11] is calculated using approach presented in [12]. Fig. 13-b shows the curves of calculated modal refractive indices for side-core modes LP_{11} and LP_{21} , and central-core fundamental mode LP_{01} , together with which two groups of vertical dashed color lines are plotted to represent QPM resonance positions: the blue group on the left for LP_{21} and the red group on the right for LP_{11} . These resonances are calculated from Eqn. (1) and labeled with parameter Δm , which are derived from our theoretical model. In Fig. 13-c, experimentally measured transmission spectrum has been obtained by launching a broad-band super-continuum laser source into the central 35 μm -diameter core of the 1.5m-long CCC fiber. Main observation here is that multiple resonances appear as transmission “dips”. Most important, the extension of these “dips” marked as the vertical light-grey dotted lines appear to exactly overlap with the calculated QPM resonances in Fig. 13-b. This verifies the fact that QPM coupling involving optical angular momentum indeed occurs. Further comparison between Fig. 13-a, 13-b and Fig. 13-c reveals that modal-interaction resonances are observed as transmission “dips” only at the wavelengths where a side-core mode experiences non-negligible losses, namely exceeding approximately 1dB/m loss. Modal interactions at wavelengths shorter than these 1dB/m-loss wavelengths (marked in Fig. 13-b by points A and B for side-core LP_{21} and LP_{11} modes respectively) still do occur, but do not result in observable central-core modal loss. This has been experimentally verified for the “lossless” resonance at 1030nm (see discussion of Fig. 14 below). In addition, Fig. 13-d shows numerically calculated transmission spectra of all central-core modes, and the comparison between Fig. 13-c and Fig. 13-d shows that all these “dips” belong to central-core fundamental mode, which also indicates the effective single-mode operation of this particular CCC sample (see details below).

Direct experimental demonstration and measurement of inter-core modal interactions involving modal angular momentum are presented in Fig. 14. We explored CCC fiber performance in the vicinity of low-loss 1030nm resonance marked in Fig. 13-b by line C-D. At this wavelength central-core fundamental LP_{01} and side-core LP_{11} are quasi-phase-matched, corresponding to $l_1 = 0, l_2 = -1, \Delta s = -2$ with the resulting $\Delta m = 0 - 1 - 2 = -3$, which can be easily verified by plugging the values of these numbers and propagation constants at 1030nm into Eq. (1). Fig. 14-a and Fig. 14-b show the output from the same 1.5m-long CCC fiber sample when only the central core is excited: one is measured at wavelengths outside the 1030nm resonance and the other is measured at the 1030nm resonance. One can see that outside the resonance output signal is observed only in the central-core, while at the resonance fiber output signal is observed in both the central core and side-core, thus directly confirming inter-core

modal interaction at 1030nm. Furthermore, central core output appears to be single-mode (as confirmed by more rigorous measurement described below), while side-core mode, observed at the resonance, exhibits a clear ring-like higher-order mode pattern, consistent with LP_{11} optical vortex. The later was further confirmed experimentally: we used a narrow linewidth laser operating at 1030 nm to excite the side core and, in addition, to produce a reference plane-wave, and the overlap of them will produce an interference pattern presented in Fig. 14-c, which indeed confirms that the side core output is an optical vortex with the topological charge $|1|$.

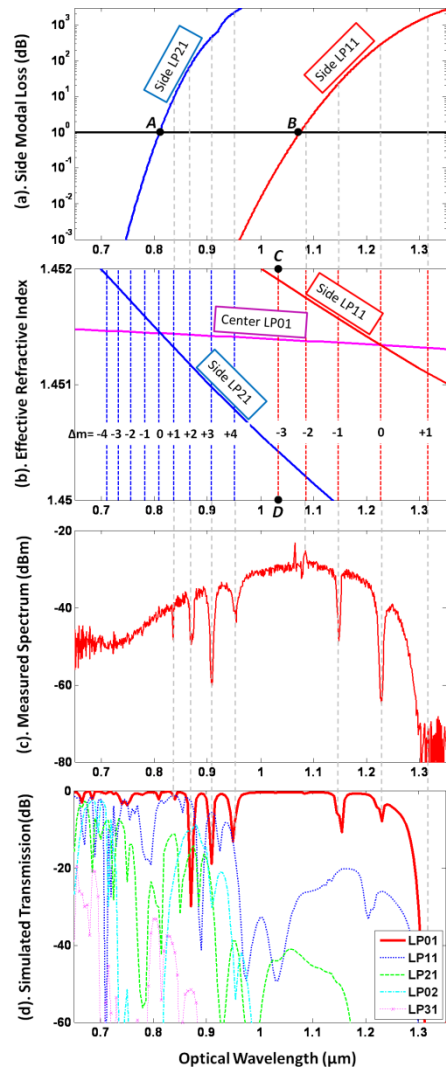


FIG. 13. Calculation and measurement of quasi-phase-matching (QPM) for 1.5m-long CCC fiber sample. (a) Calculated loss for side-core LP11 and LP21 modes as a function of wavelength. (b) Calculated refractive indices of interacting modes and calculated QPM resonance positions. (c) Experimentally observed transmission spectrum through CCC fiber central core. (d) Calculated transmission of different central-core modes.

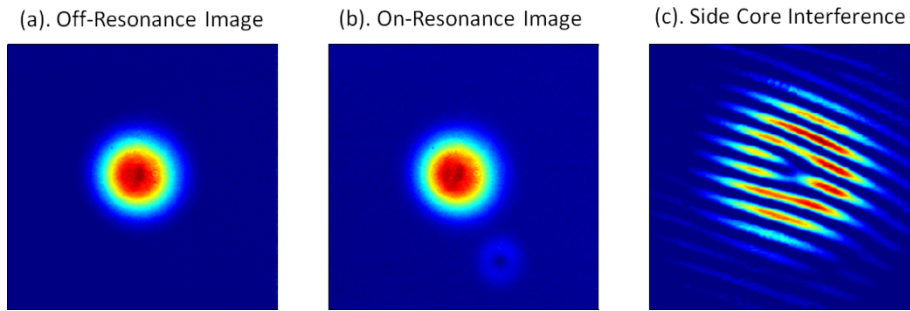


FIG. 14. Direct experimental demonstration and measurement of inter-core modal interactions involving modal angular momentum: (a) Output image outside the 1030nm resonance showing only central core. (b) Output image at the 1030nm resonance showing coupling from central core to side core. (c) Interference pattern showing optical vortex with topological charge $|1|$ [13].

Fig. 15 shows another example which compares model prediction and experimental observation for a 55 μm core Ge-doped CCC fiber. This structure is very different from the above design in that it contains 8 side cores, as shown in a fiber cross-section photos in Fig. 1 above. Use of multiple cores allows achieving core scalable HOM suppression and also significantly relaxes center-side core separation requirements from $\sim 2\mu\text{m}$ - $3\mu\text{m}$ in single-side designs to $\sim 7\mu\text{m}$ in the 8-side 60 μm central-core designs and even larger for larger core sizes. In Fig. 15 the measured core-transmission spectrum through 2m long fiber is presented together with the calculated LP₀₁ and LP₁₁ loss spectra for the same length of the fiber. Calculated LP₀₁ loss in the 1 μm to 1.1 μm spectral range is negligible ($\ll 1\text{dB}$) but abruptly increases at $\lambda > 1150\text{nm}$ to more than 100dB, while LP₁₁ loss is higher than 50dB and is relatively constant at all wavelengths above $\sim 1\mu\text{m}$. All other HOM, not shown here, have loss well exceeding that of LP₁₁ at all wavelengths in this plot. Observed core-transmission spectrum for $\lambda < 1150\text{nm}$ follows nearly perfectly the calculated LP₀₁ loss, thus indicating that all HOM are suppressed in this range. This agrees well with the measured robust single-mode characteristics in the 1-1.1 μm range using spectral beating measurement presented (for the same fiber, but for shorter 1.5m length) in Figures 3-5 above. Note, however, that in the region between 1200nm and 1300nm LP₀₁ loss exceeds that of LP₁₁, which is consistent with the observed “flat” top of the measured transmission spectrum in this region where LP₁₁ mode dominates in the fiber output.

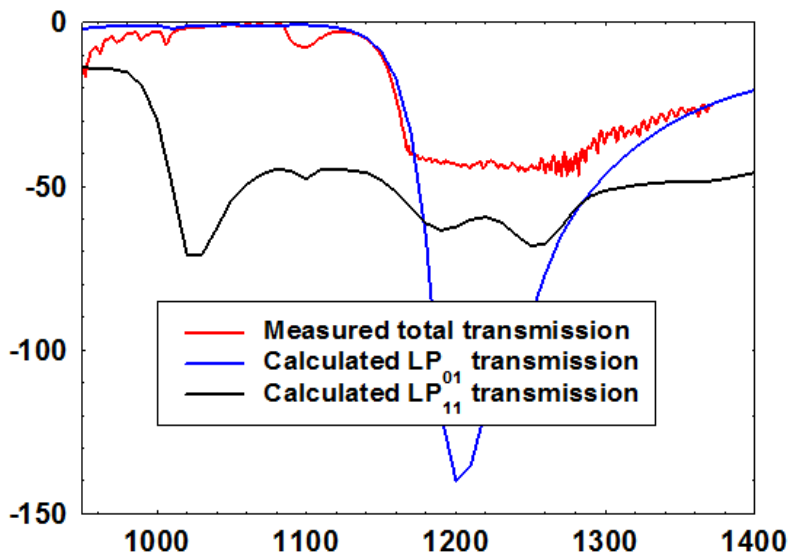


Fig. 15. Comparison between measured transmission of 2m long 55 μm core Ge-doped fiber and the calculated transmitted powers of LP₀₁ and LP₁₁ modes. Experimentally observed long-wavelength loss “step” at above $\sim 1150\text{nm}$ corresponds to the region of predicted high fundamental-mode loss, and is, therefore, dominated by the LP₁₁ transmission.

These two examples represent just two particular examples indicating a general agreement between model and experiments that has been consistently observed in CCC fibers of various designs that were fabricated during the JTO MRI program. This establishes a high degree of confidence in the accuracy and predictive capability of the CCC fiber numerical model developed in this program.

Numerical model for calculating CCC fiber mode-transmission properties is based on a fully-anisotropic Beam-Propagation Method developed specially for this project. The problem we had to solve was associated with the discovery in the mid-project of the quasi-phase-matched intermodal interactions in the CCC structure which were caused not only by the purely “geometrical” modal perturbations due to the presence of the side core/cores, but also by the linear-birefringence and circular-birefringence perturbations located in the spacing between the central and side cores (see more details in the above theoretical discussion as well as in Appendix A). All existing BPM algorithms and commercial software that we used in the initial stage of the project are essentially scalar methods (home-written scalar BPM initially and later BeamProp software package by RSoft) or Full/Semi-vectorial BPM algorithms (RSoft BeamProp). Either of these two approaches is not suitable for accounting for rotating linear birefringence and, more critically, for the local circular birefringence effects in CCC structures. Critical breakthrough in this program of achieving large-core single-mode CCC fibers was accomplished only after we succeeded in overcoming this formidable theoretical/numerical challenge. Essentially, we had to develop an entirely new numerical BPM algorithm, which is capable to account for a full birefringence (i.e. to account for *all nine* dielectric perturbation terms) including linear and circular birefringence. As such, this method has a more universal significance since it can be applied to any anisotropic electromagnetic-wave propagation problem in general. It would be too cumbersome to describe this method in detail in this Report, but we are currently developing a full paper on this topic that we are planning to publish in the future. At present, details of this method can only be found in a public domain in Xiuquan Ma’s Thesis (2011), available at the University of Michigan.

CCC Fiber Fabrication Development and CCC Fiber Technology Commercialization, Demonstration of CCC Fiber Based Components for Monolithic Integration

Another important outcome of the program is that fabrication of these novel fiber structures has been performed by several commercial fiber manufacturers and a company Arbor Photonics has been established as a spin-off from the University of Michigan to commercialize CCC fibers and CCC fiber based laser systems. This had established a pathway for this technology from university laboratory to practical use in a diversity of applications. Overall, CCC fibers have been successfully fabricated by four different commercial fiber manufacturers, each using very different fiber fabrication approaches. Two of these manufacturers have been engaged in this program. The first one is Nufern, which was successful in demonstrating the very first 35 μm core single-mode CCC Ge-doped and Yb-fibers using conventional MOCVD fiber-preform technology. Crystal Fibre was primarily engaged in the second half of the project, partly due to the superior precision and great flexibility achievable with their fabrication processes, but most importantly, due to their ability to produce transversely and longitudinally homogeneous fiber performs of very large-core fibers, using multiple-rod stacking techniques. Note that Arbor Photonics had developed additional commercial suppliers of CCC fibers to these two.

Success of implementing large-core CCC fibers with robust single-mode performance was achieved primarily due to very close interactions between University of Michigan and each of the fiber manufacturers. For example, interaction with Crystal Fibre was organized around biweekly teleconferences each reviewing progress and technical results of each perform and fiber fabrication step. On one hand, this allowed the fiber design team at UofM to closely monitor the actual fiber parameters and to take any design-corrective action immediately as need for it occurred during the fabrication process. On other hand, this close monitoring of fiber fabrication process provided with a detailed insight into what type of control and precision is achievable during fabrication, thus leading to new and highly successful design solutions optimized with respect to the actual fiber fabrication process. For example, multiple side design allows dramatically reducing required tolerances for the side-center core separation and relative positions. It turned out that the choice of 8 sides vs one side does not produce any added significant difficulty or cost increase to the fiber fabrication process, while relaxation of the positioning tolerances greatly facilitates reproducibility of each design and substantially reduces fabrication risks.

Since the main appeal of the all-glass and robustly single-mode large core CCC fibers is in enabling monolithic integration, we also demonstrated monolithic all-fiber components using CCC fibers. This has been done primarily through the collaboration with Arbor Photonics. This includes demonstration of monolithic pump combiners with 35 μ m core CCC fiber throughput and CCC fiber pigtailed optical isolators, both produced by commercial suppliers.

Demonstration of ~600W SBS-free 35 μ m Core CCC Based Fiber MOPA System

Within this program a variety of different fiber lasers have been demonstrated using fabricated double-clad Yb-doped CCC fibers. The most relevant with respect to the objectives of the program was the ~600W single-frequency SBS-free fiber MOPA demonstration, since it directly shows suitability of CCC fibers for high-power single-frequency building blocks for coherently-combined fiber laser arrays.

Spectral width of an output from each individual laser channel in a coherently-combined fiber laser array determines its coherence length. Fiber length mismatch between parallel fiber laser channels has to be much shorter than the coherence length, thus constraining spectral linewidth of each fiber channel in the coherently combined array to a few GHz at most [14, 15]. It is generally recognized that narrow-linewidth requirement constitutes the most difficult challenge since power of such narrow- bandwidth signals is limited by SBS, whose gain coefficient is more than two-orders of magnitude larger than of SRS (the limiting nonlinearity for broad-band signals) [16].

With present fiber technology monolithically-integrated systems can only be implemented using conventional LMA fibers, limited to ~25 μ m core diameter if single-mode operation has to be maintained [17]. As it has been shown experimentally [17] SBS-limited single-frequency (<< than SBS bandwidth of ~40MHz) operation in a monolithic 25 μ m core LMA system is limited to only 100W – 200W level. SBS onset can be mitigated by spectrally-broadening laser signal using EO phase modulation. SBS-limited laser power then can be increased over the single-frequency limit approximately proportionally to the ratio between modulation bandwidth and SBS bandwidth [16]. For fiber laser systems based on

conventional 25 μm LMA such spectral modulation allowed to reach up to $\sim 1\text{kW}$ of output power at several GHz linewidths [17], approximately the largest bandwidth still compatible with coherent combining. It is clear, however, that the SBS-limited power scalability each fiber-array “building block” is fundamentally determined by the SBS threshold of a single-frequency signal.

Our work focused on exploring the highest achievable SBS-free single-frequency cw laser power. Prior to this high-power work all fabricated double-clad CCC fiber geometries had 250 μm diameter polymer-coated (NA = 0.45) cladding, small size of which significantly limited pump powers that could be coupled into it. To overcome this limitation we had fabricated two different Yb-doped CCC fiber double-clad geometries, all optimized for high power pumping. One is 400 μm diameter polymer-clad (NA = 0.45) fiber, and another is 260 μm diameter air-clad (NA = 0.6) structure. Cross section examples of these two geometries are shown in Fig. 16. These two double-clad geometries had been selected in order to match the brightness of the multi-kW pump sources that were available for this program. As it is described in greater detail in the Fraunhofer USA section of the Final Report, for this experiment we had six high-brightness pump diodes, with individual power between 300W and 600W and each coupled into 200 μm diameter and NA = 0.2 delivery fiber. We have fabricated in the University of Michigan laboratory a close-packed seven-fiber array bundle for pumping the CCC fiber, each fiber in the bundle is spliceable to a pump-diode delivery fiber, thus providing with up to 2.1kW of total pump power that could be focused into 400 μm spot size with less than 0.45NA or into $\sim 260\mu\text{m}$ spot size with less than 0.6NA, i.e. compatible with both fabricated double-clad geometries. This allows us to use up to $\sim 2.1\text{kW}$ of total pump power with either of the two double-clad geometries.

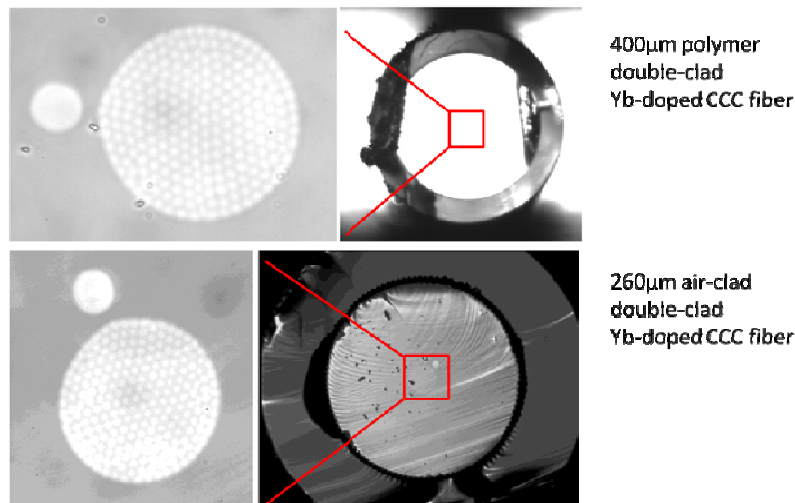


Fig. 16. Cross-sections of a 400 μm diameter polymer-clad (NA = 0.45) and 260 μm diameter air clad (NA = 0.6) fibers.

Our choice of these two double-clad geometries was due to our interest to explore and compare their performance at high pumping powers. Polymer-clad DC structures offer better heat removal from a fiber compared to air-clad structures, where the air-gap at the boundary between the inner and outer cladding constitutes a significant thermal barrier [18]. However, standard fluoro-acrylate polymer coating for pump-power guiding should be used at fiber surface temperatures below 80 $^{\circ}\text{C}$, while the

outer protective coating of an airclad fiber can withstand up to 200°C. Consequently, air-clad fiber could be operated at much shorter lengths and much higher longitudinal thermal gradients, both factors contributing to increasing the SBS-free output power. This consideration explains the difference in the pump cladding size for the two DC geometries. Indeed, polymer-clad 400µm diameter fiber at 975nm pump wavelength has cladding absorption of ~4.5dB/m, while the absorption of 260µm diameter air-clad is ~9dB/m. For a typical kW-pumped power-amplifier geometry used in laboratory experiments this leads to approximately 4-6 m long polymer-clad and 2-3 m long air-clad CCC fibers.

The CCC core structures were identical for both polymer-clad and air-clad fibers, with Yb/Al doped central core size of 37.2µm (MFD = 30µm) and NA = 0.069, Ge-doped side-core size 9.8µm and NA = 0.089, side-core to central-core separation of 3.5µm and helix period of 6mm. Predicted SBS-free power performance for this CCC fiber core in counter-pumped amplifier configuration is shown in Fig. 17. This figure shows SBS threshold for a single-frequency amplified signal as a function of fiber amplifier length for three different amplifier gain values of 20dB, 25dB and 30dB. Examination of this figure indicates that for 2m to 3m long air-clad CCC amplifier this single-frequency SBS threshold could be in the 600W to 1kW range, depending on the exact value of the amplifier gain. Note that this calculation does not include any effects associated with a longitudinal temperature distribution in the amplifier, resulting from longitudinally-varying thermal load due to the pump absorption. As it is well known [19] longitudinal temperature variation shifts local SBS stokes-wave frequency thus further increasing SBS threshold. This simple-model prediction was consistent with the results obtained in the actual experiment.

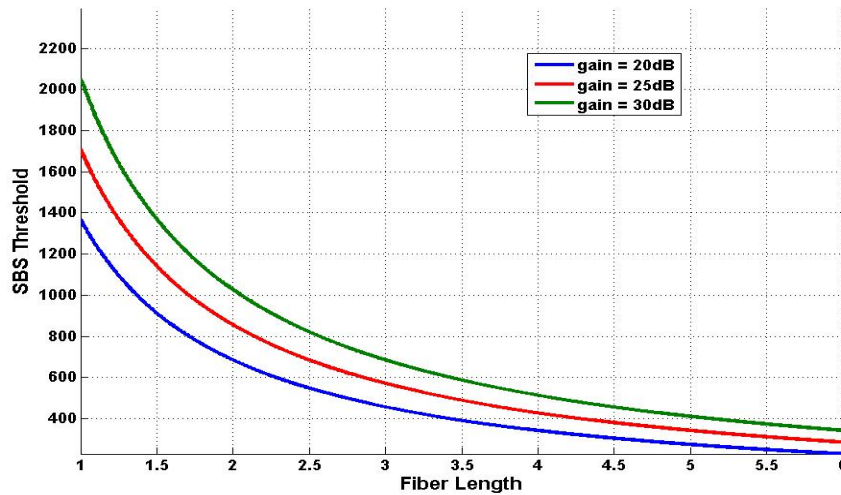


Fig. 17. SBS threshold dependence vs fiber amplifier length in a counter-pumped 30µm MFD core CCC amplifier for different signal total-gain values.

Experimental Setup for single frequency CW power scaling with CCC fiber is shown in Fig. 18. It consists of a single-frequency DBR laser diode source operating at 1064nm (Sacher Lasertechnik TEC 50 that has been provided by collaborators in this program from NGC (J. Rothenberg)), one stage single mode PM fiber pre-amplifier, one 5m long CCC Yb-doped double clad fiber preamplifier with 35µm core, 250µm

cladding and the last power amplification stage using CCC Yb-doped airclad fiber. Narrow bandpass filters are placed in between the stages to suppress ASE buildup. We used up to 2.2W signal power from CCC pre-amplifier to seed the 2.7m long CCC power amplifier. One wedge is placed before the final CCC power amplification stage to monitor the counter propagating signal in order to determine the onset of the SBS scattering. The final CCC power amplification stage is counter pumped with a pump combiner bundle consists with three 976nm fiber-pigtailed pump diodes spliced in. All six diodes were not used here since in this amplifier output power amplifier was limited by the fiber surface damage, not the pump power.

Fig. 18. Experimental setup of counter-pumped high power single-frequency, single-transverse mode and robust output polarization CCC fiber MOPA

Amplified power results for the counter-pumped amplifier configuration are shown in Fig. 19. Output power is plotted vs absorbed power since the pump diode wavelength was strongly varying with pump current from $\sim 966\text{nm}$ at low pumping to $\sim 974\text{nm}$ at high pumping. Power amplifier slope efficiency is 70% for 2.2W seed signal at the power amplifier input. Insert in the Fig. 19 shows expanded-scale plot of the counter-propagating (against amplified signal) power (measured at the SBS-monitoring port at the power amplifier input) as a function of MOPA output power. One can see that up to maximum 511W output achieved in this experiment no SBS onset has been observed, indicating potential for further average power scaling of single-frequency signal. Measured M^2 value of the output beam is 1.19 ± 0.06 , verifying single-mode performance of the system. Note that the output beam was not changing with the power-amplifier input misalignment, indicating that single-mode performance was intrinsic to the fiber and not the result of single-mode excitation. Also note that in this case we used M^2 measurement to determine output beam quality as opposed to the more rigorous methods described earlier. The reason is that the amplifier is operating with a narrow-linewidth output, incompatible with the S^2 based measurements of modal content. Output polarization of CCC fibers has been shown to be robust against temperature and mechanical perturbations of the CCC fiber amplifier [8]. As shown in Fig. 20 linearly

polarized output was preserved at the output of the MOPA system with PER of >15dB for all PER measurements performed in the power range of up to 200W of output power. No higher powers were tested due to the imitations in the PER measurement setup at that time.

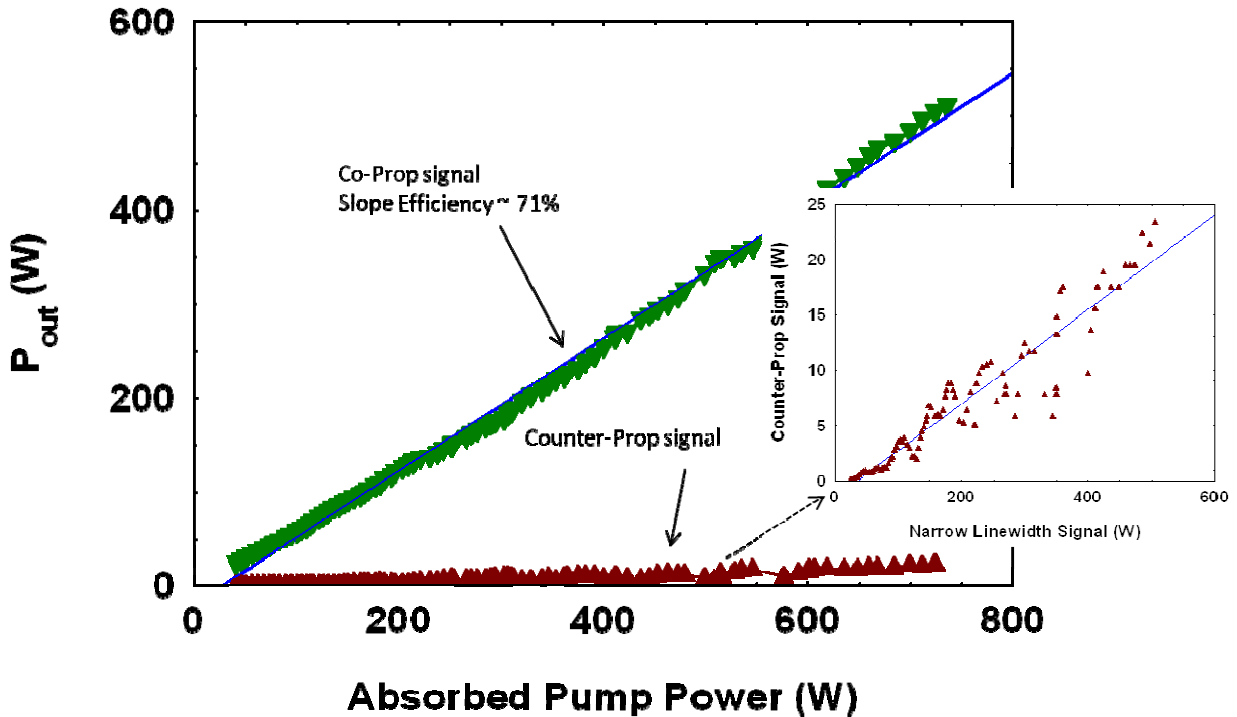


Fig. 19. SBS-free output power from a counter-pumped air-clad CCC fiber amplifier. MOPA output power is marked with green markers and counter-propagating signal for monitoring SBS presence or absence is marked with red markers. Insert shows the expanded-scale view of this monitoring signal plotted vs the amplified single-frequency signal power. Linear dependence indicates absence of SBS onset in the measured power range (up to 511W)

Achieved output power of 511W in this amplifier was limited by the surface damage systematically occurring as soon as we would reach this power level. The issue was that the air-clad pump end did not have an end-cap, a standard technique to protect the fiber-end facet from the surface damage [20]. The main challenge was to produce an end-cap that would (i) provide a geometry in which pump light could be coupled into the inner pump cladding and (ii) splicing of the end-cap would not disturb air-clad interface for pump light transmission. To overcome this challenge we explored various end-cap approaches for this air-clad fiber, two of them shown in the Fig. 21. In the first approach, shown on the left-hand of the figure, issues (i) and (ii) are addressed by using tapered end-cap so that the pump beam could directly couple into the inner air-clad cladding. This taper has been produced by splicing with a conventional telecom-type splicer a melted-glass ball to the end of the fiber and then polishing the output surface at an angle to prevent Fresnel-reflection back-coupling of the signal into the fiber core. This geometry, however, has two limitations. The ball end cap could be made only rather short (only a few hundred micrometers long), which proved to provide an insufficient protection from the surface

damage of the fiber. Also, the air-clad interface would be melted few-hundred microns-deep into the DC fiber, thus causing pump light scattering into the outer cladding, which was coated with the protective polymer. We found that though the amount of scattered light was only on the order of few percent, but at kW input pump powers this would constitute sufficient leaked-pump power to burn the outer protective polymer coating or the mounting adhesive of the fiber.

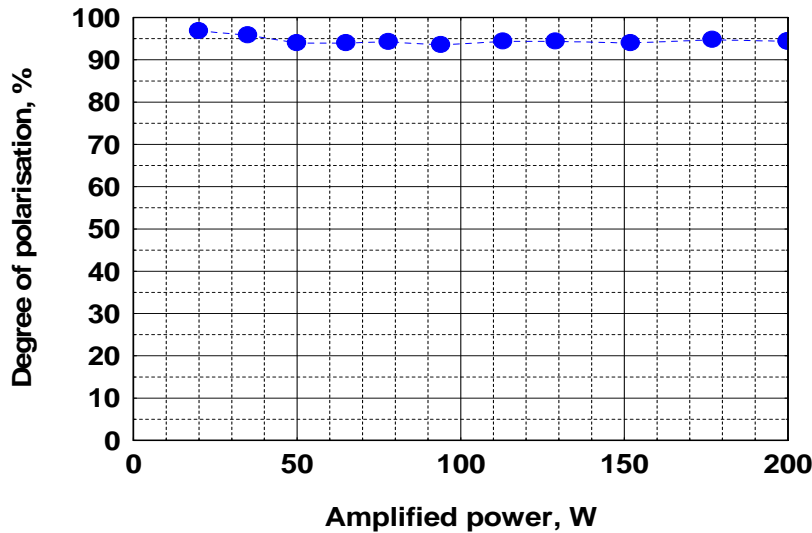


Fig. 20. Degree of polarization from a counter-pumped CCC fiber amplifier as a function of output power

The second approach, shown on the right-hand side of the Fig. 21, was based on using a CO₂ laser beam to splice the fiber to the bulk fused-silica piece to provide with a long end-cap. To avoid fusing air-clad interface in the splicing zone, which would serve as a similar scattering-barrier for the pump beam as in the previously described ball-cap geometry, we removed a short section (~1mm) of an outer cladding from the air-clad structure, as shown in the figure. In the end, this approach also turned out to be of limited use in high-power pumping since the air-clad removal would always produce a jagged-surface making the fiber extremely sensitive to any transverse pressure. The jagged-surface essentially would serve as a source of cracks, which would easily propagate through the fiber under any perturbation, producing an unwanted cleaving of the fiber.

Consequently, since the counter-pumped configuration of this air-clad fiber was limited by the surface damage at the pumped-end facet, we continued experiments with the co-pumped configuration in which un-pumped output was end-caped to prevent damage at high output powers and pumped fiber end through which the amplifier was also seeded was left without an end-cap. Although in general co-pumping leads to longer effective propagation length in an amplifier and, consequently, to lower SBS threshold, but in this case we found that the strong longitudinal temperature distribution along the fiber increased SBS threshold to a degree that completely offset the SBS threshold reduction due to the effective-length increase in this pumping configuration. Result of the co-pumped configuration power scaling is shown in Fig. 22, showing that approximately 600W SBS-free output power of amplified single-frequency signal has been reached. Again, we could not reach the SBS-limited power due to the facet damage, this time at the un-protected seeded and pumped end of the fiber. It was somewhat surprising

that this damage still occurred. We attribute that to the fact that core-air interface at the fiber end got really hot due to high heat load. This is consistent with our thermal simulations, which show that air clad fibers are in general susceptible to elevated in-core temperatures due to the significant thermal barrier at the air-cladding interface. Consequently, even though we increased output power further than in counter-pumped case, but limitations of the air-clad geometry did not allow reaching fiber-core-size limited performance.

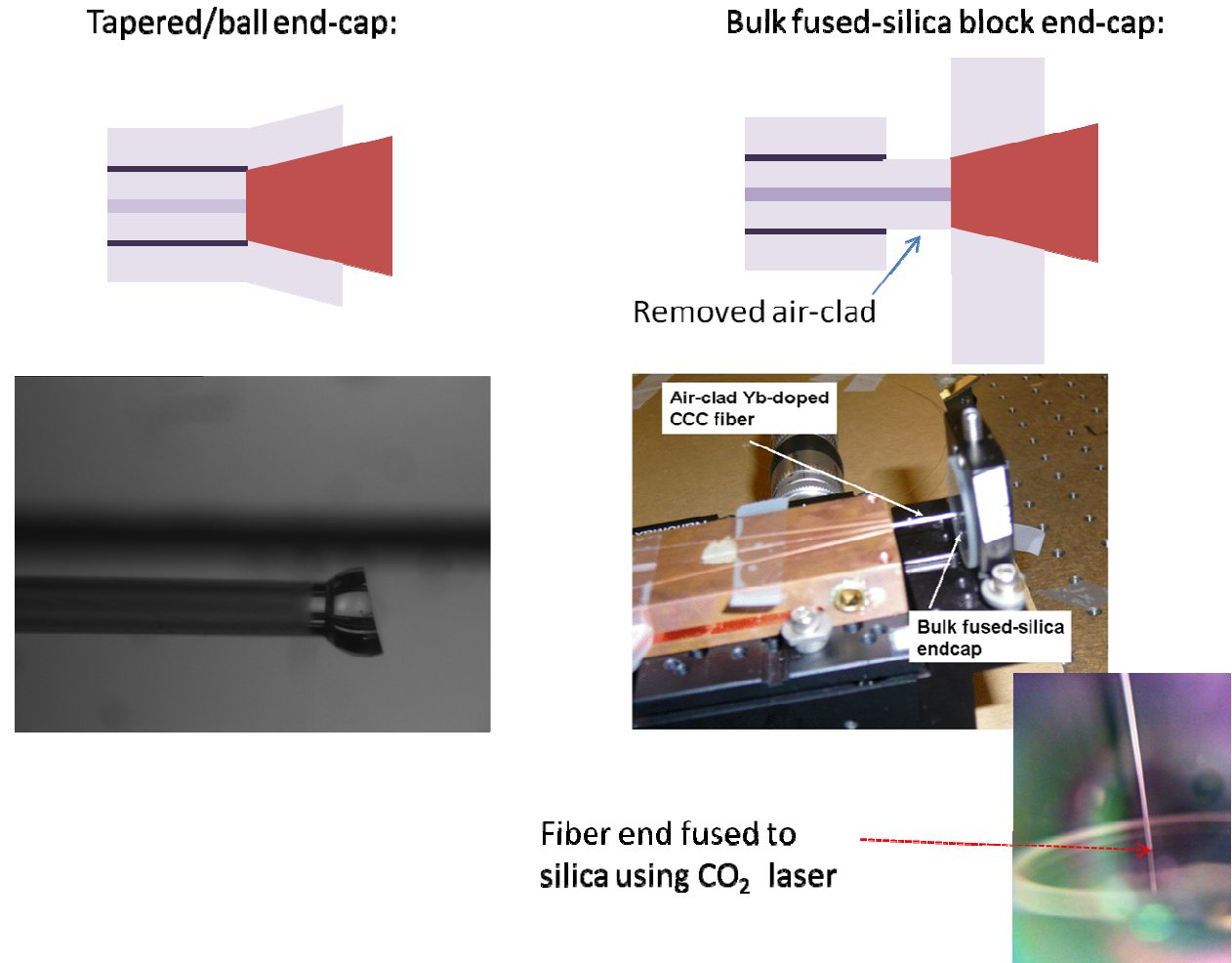


Fig. 21. Two examples of end-cap geometries for pump-end air-clad fibers. The left-hand figure shows a ball end cap, which allows the pump beam to be coupled directly into the inner cladding. The right-hand figure shows bulk-silica end cap which also allows to couple pump light directly into the inner cladding, but also allows achieving much longer end-cap lengths, thus permitting significant increase in the output-signal beam size, which is expanding after leaving the central core.

We also explored use of 400 μm polymer clad CCC fibers. For these fibers we could use standard end-cap geometry with a core-less 400 μm diameter fiber (exactly matching the pump-cladding size) spliced onto the DC-fiber end using a conventional fusion slicer, exploiting the fact that CCC structure is air-hole free. However, the limitation we encountered there was associated with the circular shape of the pump-

cladding. Previously, for 250 μ m cladding size of CCC fibers we found that the standard approach of breaking helical pump-ray paths in the cladding through octagonal-shaped cladding was not necessary. For this smaller cladding size side-core of the CCC structure would produce sufficient modal mixing in the cladding ensuring that all pump rays cross the central core and, therefore, are efficiently absorbed. Based on that experience we did not introduce octagonal shape for 400 μ m cladding. Unfortunately, we found that due to the large cladding size modal mixing due to CCC structure becomes insufficient. Complete pump absorption could in this large-cladding could only be achieved with high-brightness pump beams with NA = 0.2. For lower-brightness pump beams with NA \sim 0.45 up to half of the pump power would remain unabsorbed in this DC fiber. Consequently, 400 μ m polymer clad fibers were pump power limited by the maximum available power of up to \sim 600W from 200 μ m 0.2NA pump delivery fiber available for the experiments at that time, corresponding to only up to \sim 400W of achievable single-frequency output power from a 400 μ m clad CCC fiber MOPA.

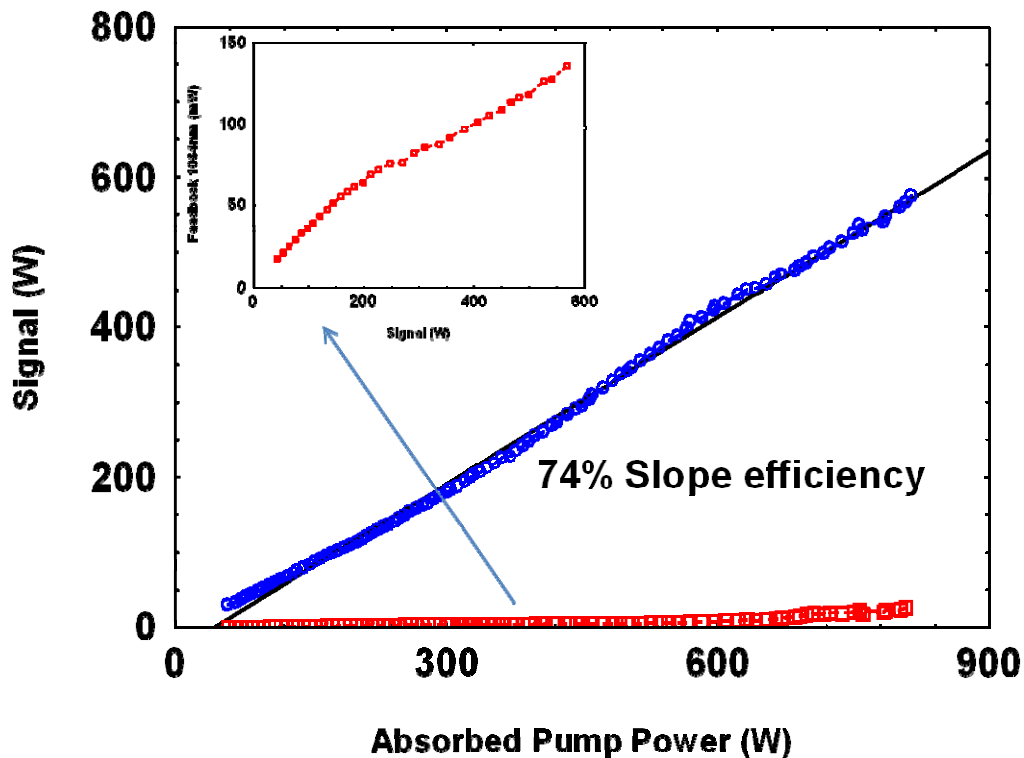


Fig. 22. SBS-free output power from a co-pumped air-clad CCC fiber amplifier. MOPA output power is marked with blue markers and counter-propagating signal for monitoring SBS presence or absence is marked with red markers. Insert shows the expanded-scale view of this monitoring signal plotted vs the amplified single-frequency signal power. Linear dependence indicates absence of SBS onset in the measured power range (up to \sim 600W)

In Fig. 23 this single-frequency CCC amplifier result is compared with other state-of-the-art achievements in the field. One can see that the demonstrated single-mode and linearly-polarized power is the highest among all reported narrow-linewidth power scaling results, for the bandwidths *below* the

SBS gain bandwidth. Note, however, that the achieved result has not been limited by the SBS threshold in 37 μm CCC core, but rather by the above described limitations coming from the specific issues in each of the two double-clad structure designs. One important conclusion was that an air-clad geometry is highly disadvantageous in that it is very difficult to implement into any practical fiber laser system. Based on the gained experience we designed next iteration Yb-doped CCC 55 μm core fibers as triple-clad structures described in the earlier sections of this report, containing an octagonal all-glass inner cladding with 0.2NA and round polymer-coated outer cladding with 0.45NA. Such structure ensures effective modal mixing for all pump rays within both claddings. Note that the octagonal inner cladding is also rotating with the helix period of the CCC structure, thus further facilitating pump mixing. This triple-clad structure retains all the advantages inherent in all-glass CCC structure in that it can be fusion spliced using standard equipment. Triple clad not only ensures complete pump absorption, but also confines large fraction of the pump power with all-glass inner cladding, thus reducing outer-polymer coating exposure to high optical intensities at multi-kW pump powers.

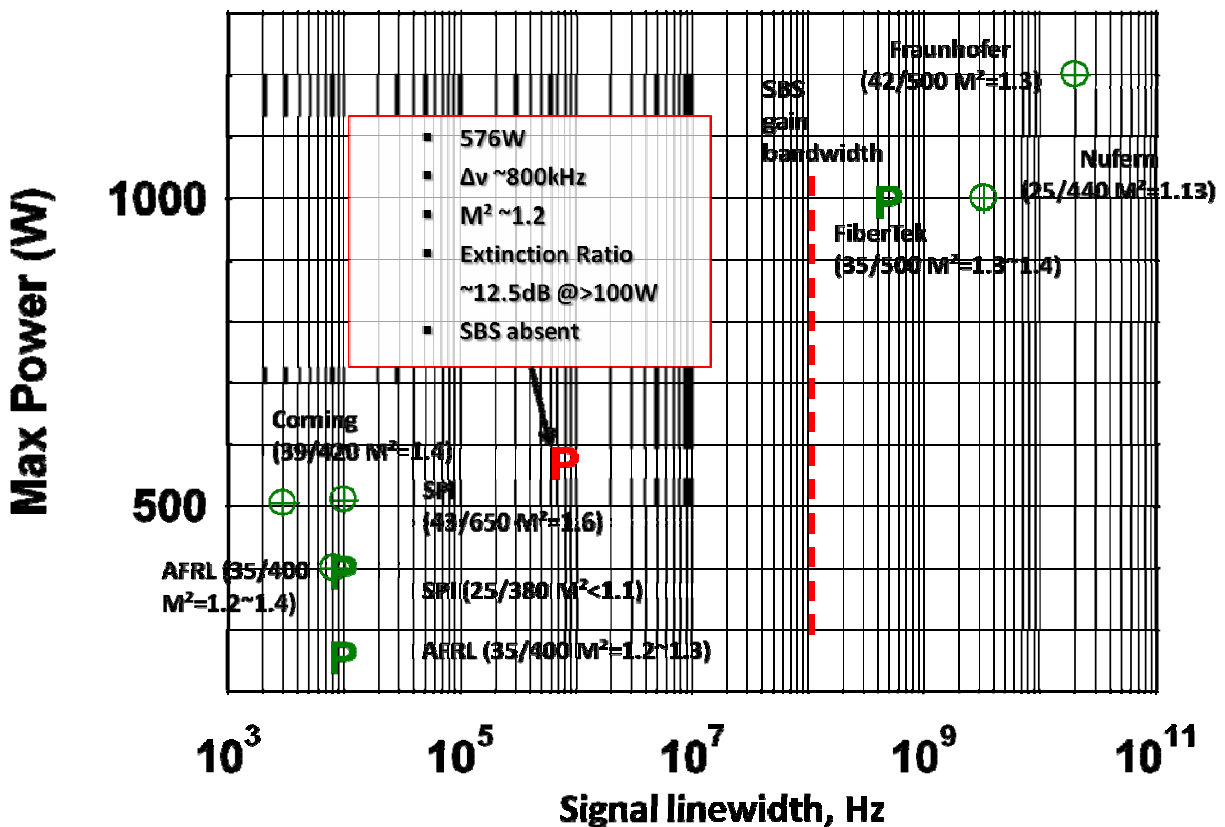


Fig. 23. Summary of the State-of-the-Art results in narrow-linewidth SBS-free power scaling with fiber amplifiers. Red dashed line indicates approximate SBS bandwidth. Marker P stands for the results with linearly polarized output and encircled cross stands for those with the un-polarized output.

Demonstration of Other Fiber Laser Systems Based on CCC Fibers

Variety of different fiber laser configurations including nanosecond pulsed millijoule energy MOPA with up to 140W average power output and 200W average power femtosecond pulse FCPA have been demonstrated based on CCC fibers. These systems have been described in detail in 2009 and 2009 Annual Reports and therefore will not be repeated here.

Other Functionalities in CCC Fibers: Demonstration of SRS-Suppression in CCC Fibers

We also have shown that functionality of CCC fibers extends well beyond just increasing the single-mode core size. We have demonstrated that spectral transmission characteristics of CCC fibers can be tailored in such a way that it can be used to suppress Stimulated Raman Scattering by designing fibers with loss-free transmission at the signal wavelength and large loss at the Stokes wavelength corresponding to Raman gain bandwidth. Two illustrative examples of such tailored CCC transmission spectrum matching the SRS gain bandwidth are shown in Fig. 24, representing 6m long 33- μm core and 4m long 60- μm core spectrally-tailored CCC fiber characteristics. One can observe from these two figures that the designed CCC fiber transmission spectrum matches the spectral profile of SRS gain coefficient in fused silica material [1] for pump wavelengths at around 1085nm and 1040nm respectively. In Fig. 24 (a), Stokes-wave peak loss at the peak of the Raman gain is $\sim 30\text{dB}$, while in Fig. 2 (b), the estimated Raman-suppressing Stokes-wave peak loss is as high as 45dB.

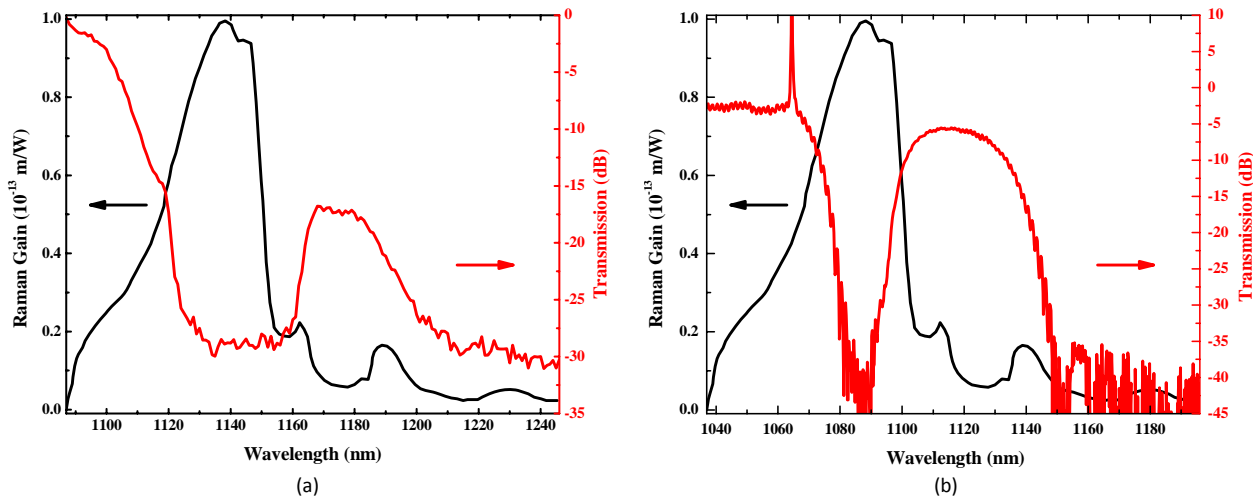


Fig. 24. (a) The 33 μm -core CCC fiber sample's transmission spectrum (red line) from 1087nm~1246nm and corresponding vertical axis on the right is shown to match the Raman Stokes gain spectrum (black line) for pump wavelength at 1087nm. (b) The 60 μm -core CCC fiber sample's transmission spectrum (red line) from 1037nm~1097nm and corresponding vertical axis on the right is shown to match the Raman Stokes gain spectrum (black line) of pump wavelength at 1040nm. Both figures are plotted as a function of wavelength and vertical axis on the left indicates Raman gain coefficient value for different wavelengths.

Results of experimentally demonstrated SRS suppression in 6m long 33 μ m core CCC fiber are shown in Fig. 26 and Fig. 27. The measured output spectra recorded after the test fiber for 1052nm (Fig 26 (a)) and 1087nm (Fig. 26 (b)) signals show the evolution of the output spectra versus different pumping peak powers at the two selected pump wavelengths respectively. We tested both these cases for input (into the test fiber) peak powers of up to 30kW. Significant difference in the measured spectral characteristics is easy to observe here, indicating significant SRS growth for 1052nm pumping and complete absence of observable SRS for 1087nm pumping. To quantify this difference we have integrated the spectral power of the total measured spectrum and at the wavelengths longer than the signal wavelength by 20nm for both signal wavelengths in Fig. 26 (a) and (b). The obtained fraction of the power in the long-wavelength portion with respect to the total power is plotted for both signals in Fig. 27. This clearly shows that SRS is indeed suppressed at all tested peak powers by the tailored loss profile of this CCC fiber, while without suppression SRS power appears to grow starting from few-kW peak powers. Note that one can also observe in Fig. 26 some amount of spectral broadening associated with non-phase-matched four-wave-mixing in the test fiber. Interestingly, this FWM induced spectral broadening also appears to be suppressed for 1087nm pumping due to the fact that this signal is “sandwiched” between two spectral transmission “dips”.

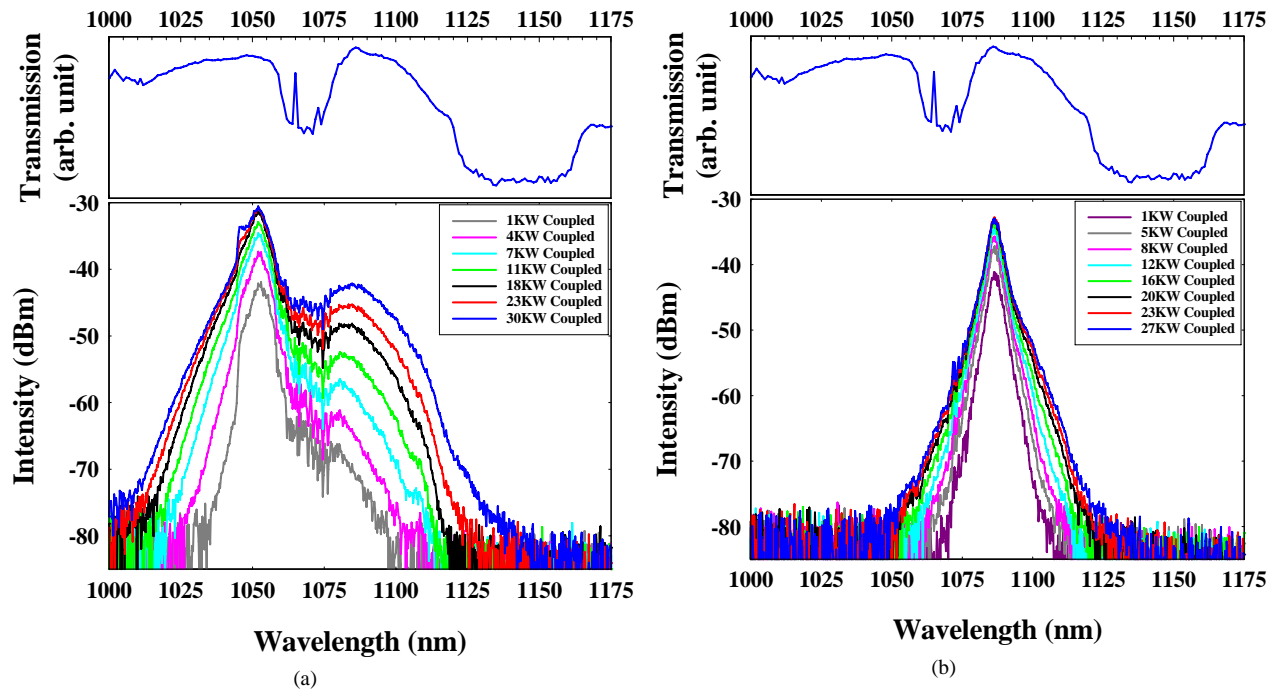


Fig. 26. Output Spectrum versus coupled input peak power. (a) 1052nm pump wavelength with 7nm bandwidth. (b) 1087nm pump wavelength with 4nm bandwidth. The inset shows the transmission spectrum of the tested CCC fiber. In both figures series of curves corresponds to the peak power of signal pulses increasing from 1kW progressively to ~30kW.

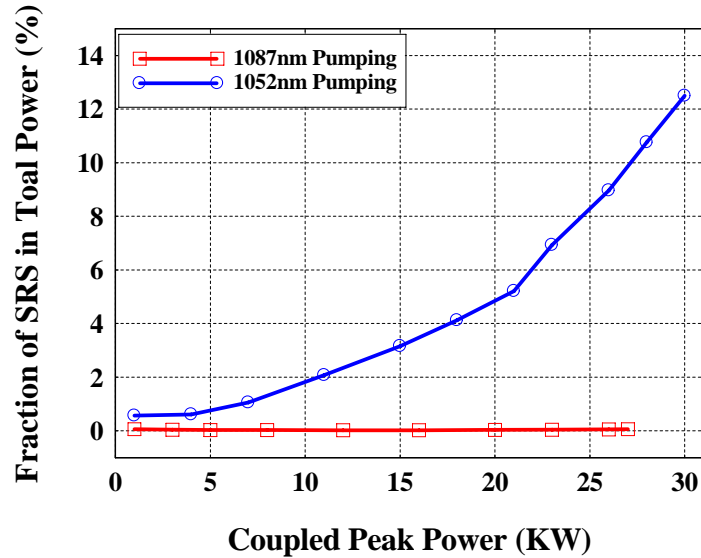


Fig. 27. The power fractions of the integrated components according to wavelength longer than 1075 nm in Fig 26 (a) and the integrated components according to wavelengths longer than 1110nm in Fig 26 (b) versus coupled peak power.

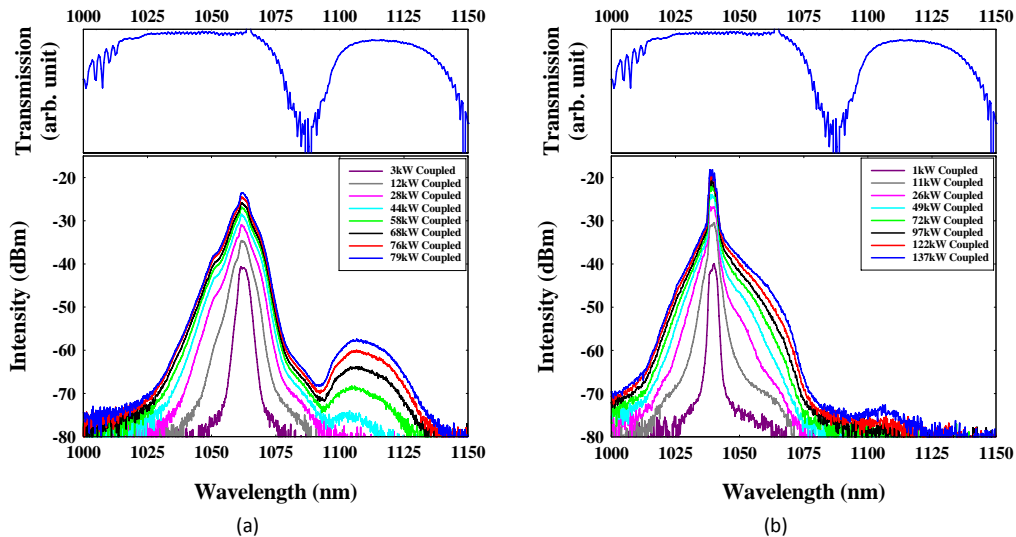


Fig. 28. Output Spectrum versus coupled input peak power measured for the 4m 60µm core CCC test sample. (a) 1060nm pump wavelength with 7nm bandwidth. (b) 1040nm pump wavelength with 4nm bandwidth. The inset shows the transmission spectrum of the tested 60µm CCC fiber.

Similarly, the 4m long 60µm-core CCC fiber sample was tested. The measured output spectra recorded after the test fiber for 1060nm (Fig 28 (a)) and 1040nm (Fig. 28 (b)) signals show the evolution of the output spectra versus different pumping peak powers at the two selected pump wavelengths respectively. For the experiment of 1060nm pumping, the peak powers coupled into the fiber is up to 80kW, while for 1040nm pumping, the coupled peak power is up to 140kW. The difference of these two power level is due to the varied achievable gain in Yb-doped fiber amplifiers. Significant SRS growth for 1060nm pumping and effective suppression of SRS suppression for 1040nm pumping was clearly

observed. To quantify this difference we have integrated the spectral power of the total measured spectrum and at the wavelengths longer than the signal wavelength by 35nm for both signal wavelengths in Fig. 28 (a) and (b). The obtained fraction of the power in the long-wavelength portion with respect to the total power is plotted for both signals in Fig. 29. Again, this clearly shows that SRS is indeed suppressed at all tested peak powers by the tailored loss profile of this CCC fiber, while without suppression SRS power appears to grow starting from 45-kW peak powers.

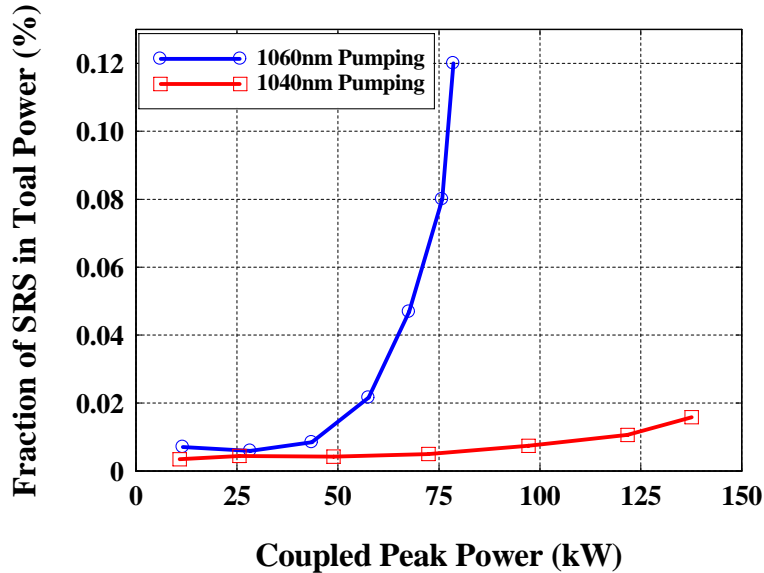


Fig. 29. The power fractions of the integrated components for wavelengths longer than 1095 nm in Fig 28 (a) and the integrated components for wavelengths longer than 1075nm in Fig 28 (b) versus coupled peak power.

Such SRS suppression together with general decrease in effective fiber-core nonlinearity due to the large modal size can significantly facilitate high power broad-band signal generation and delivery in multi-kW systems. SRS threshold is recognized as the dominant factor limiting the achievable or fiber-deliverable cw or pulsed power in broad-band systems. As we have shown theoretically [21] Stokes-wave suppression provides with length-independent SRS threshold (for long fiber lengths). Consequently, it enables long fiber amplifier or laser lengths, which can significantly facilitate heat dissipation in multi-kW pumped systems. Furthermore, length independence of SRS threshold in combination with high SRS-threshold power values in these large-core fibers can be particularly useful for long-fiber delivery of multi-kW optical power. For example, from Fig. 28 and Fig. 29 one can estimate that cw power of >50kW could be delivered with such SRS suppressing 60 μ m core CCC fiber with lengths from 4m to >10m.

Summary and Future Possibilities

In summary, it is clear that the demonstrated large core single-mode CCC fiber technology enables a significant increase in achievable cw SBS-free powers in parallel fiber amplification channels of a coherently combined fiber laser array. This is shown in Fig. 30 where the calculated achievable SBS-limited output power is plotted as a function of a fiber amplifier length for three different fiber core sizes and for two different signal bandwidths. Yb-doped fiber amplifier gain for all examples is assumed

to be 20dB, and an amplifier is counter-pumped - the most favorable pumping configuration which increases nonlinearity threshold by a factor of 2 – 3 times compared to a co-pumped configuration. Three fibers considered here are: 20 μm core standard LMA used in all standard industrial monolithically integrated lasers (black lines), 38 μm core CCC used in our experimental power scaling demonstration described in this report (blue lines), and 60 μm core CCC fiber that has been demonstrated at the end of the program (red lines). The two sets of curves correspond to *single-frequency* signal (with signal bandwidth $\Delta\nu_{\text{sig}}$ smaller than the SBS gain bandwidth $\Delta\nu_{\text{SBS}}$), lower set of three curves, and 1GHz signal bandwidth, upper set of curves. Note that the plotted results are consistent with the previously described 37.2 μm core CCC power scaling results as well as reported SBS-free power scaling results with 20 μm - 25 μm core LMA Yb-doped fibers. The main result that is evident from this figure is that the demonstrated large core CCC fibers enable *single-frequency* power scaling into >1kW range, and for 1GHz bandwidth signals into >10kW per laser channel range (for fiber amplifier lengths from few meters and up to \sim 10m, consistent with the heat dissipation constraints put on the fiber length at multi-kW pumping). This is a significant enhancement of the technological capability, consistent with the original program objectives. It is important to emphasize that the demonstrated CCC fiber technology is completely compatible with monolithic integration, a crucial requirement for practical implementation of a multiple-channel combined fiber laser arrays.

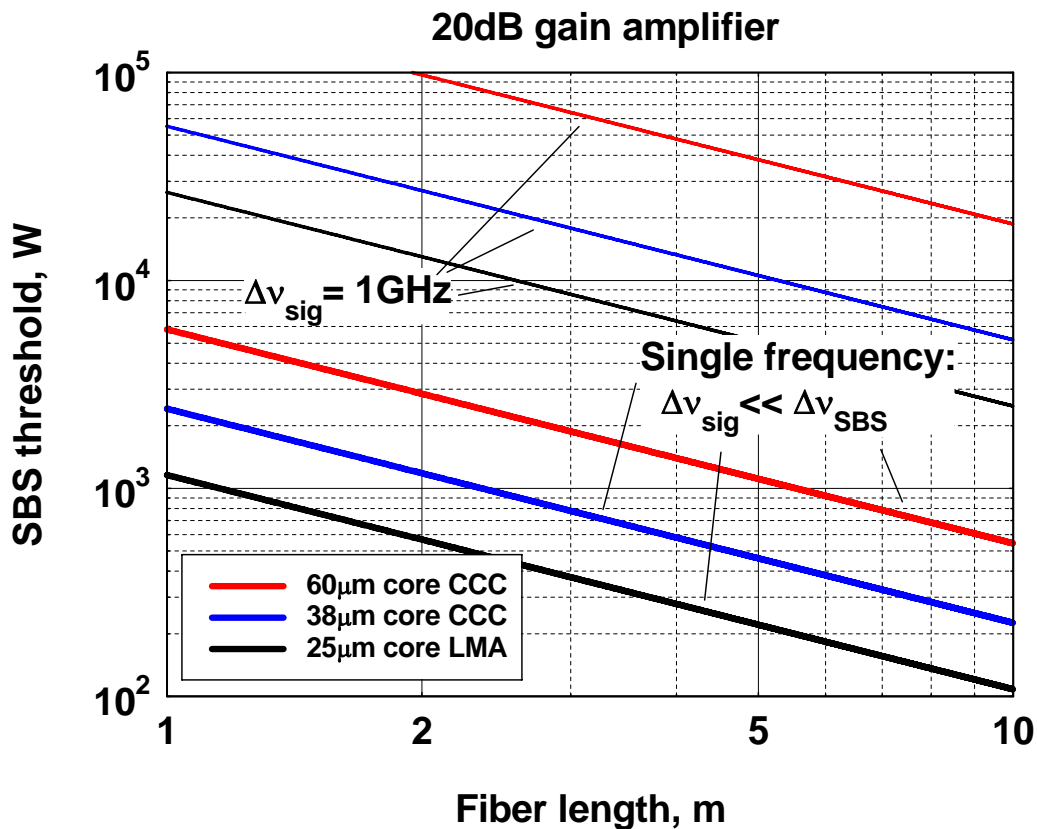


Fig. 30. Calculated SBS-limited output power achievable with 20dB counter-pumped Yb-doped fiber amplifiers as a function of fiber amplifier length. Calculation results are given for three different fibers and for two different signal linewidths, as indicated in the figure.

As for the future outlook for the CCC fiber technology we would like to note that the demonstrated single-mode core sizes do not constitute a core-size scaling limit. In fact, the fabricated 55 μm core fibers could have been simply scaled up to larger core sizes by using the original perform. This is illustrated in Fig. 31, which shows an example of numerically simulated modal characteristics of an 85 μm CCC fiber predicting robust single-mode performance. This fiber is the exact copy of the 55 μm single-mode core design, which has been described earlier in the report, except for the size (proportional increase of both central and side cores as well as the separation between them).

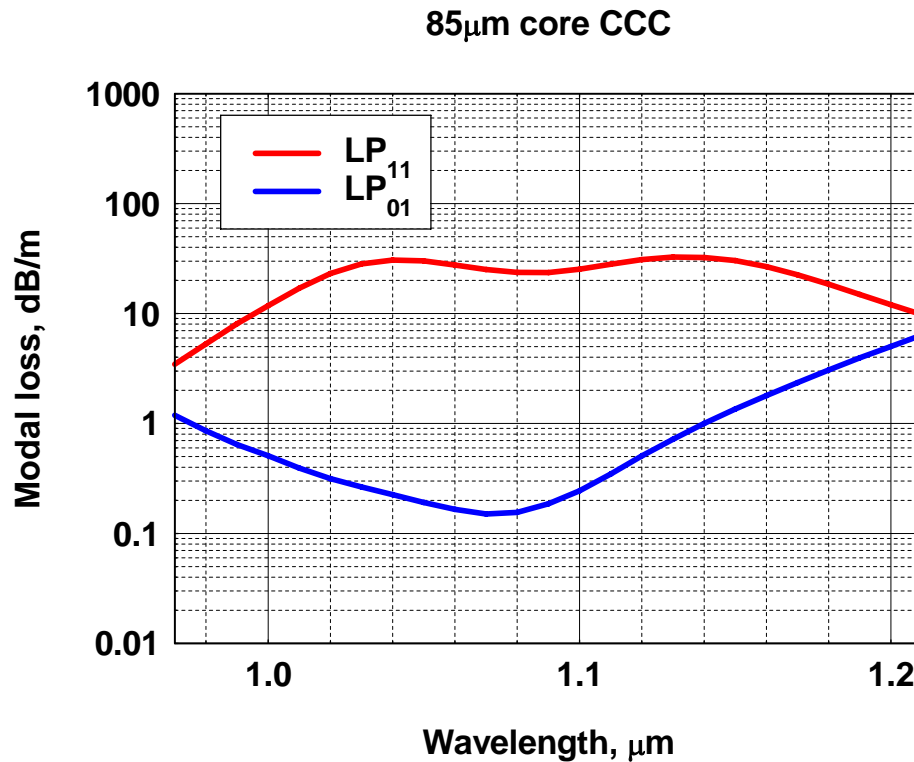


Fig. 31. Calculated modal leakage-loss for 85 μm core CCC fiber designed to operate in the $\sim 1\mu\text{m}$ wavelength range of Yb-doped fibers, indicating the predicted effectively single-mode performance. This example corresponds to the perform geometry which is identical to the actually fabricated 55 μm core CCC fiber that has been demonstrated to perform robustly single-mode.

This indicates a significant further potential for CCC fiber technology.

References for Section #1 “Chirally-Coupled Core Fiber Technology”

- [1] S. Wielandy, “Implications of Higher-Order Mode Content in Large-Mode-Area Fibers with Good Beam Quality,” *Optics Express* **15**, 15402 (2007).
- [2] J. W. Nicholson, A. D. Yablon, S. Ramachandran, and S. Ghalmi, “Spatially and spectrally resolved imaging of modal content in large-mode-area fibers,” *Opt. Express* **16**, 7233-7243 (2008).
- [3] Xiuquan Ma, Chi-Hung Liu, Guoqing Chang, and Almantas Galvanauskas, “Angular-momentum coupled optical waves in chirally-coupled-core fibers,” *Opt. Express*, **19**, 26515-26528 (2011).
- [4] www.ipgphotonics.com
- [5] High power laser handbook, Hagop Injeyan, Gregory D. Goodno, editors, New York : McGraw-Hill Professional, 2011. Chapter 18.
- [6] “TIA Standards, FOTP-80 IEC-60793-1-44 Optical Fibres - Part 1-44: Measurement Methods and Test Procedures - Cut-Off Wavelength.”
- [7] P. McIntyre and A. W. Snyder, “Light Propagation in Twisted Anisotropic Media: Application to Photoreceptors”, *J. Opt. Soc. Am.*, vol. 68, No. 2, 149 – 157 (1978)
- [8] Michelle L. Stock; Chi-Hung Liu; Andrey Kuznetsov; Gaston Tudury; Almantas Galvanauskas; Thomas Sosnowski, “Polarized, 100 kW peak power, high brightness nanosecond lasers based on 3C optical fiber”, *Proceedings of the SPIE, Volume 7914, Fiber Lasers VIII: Technology, Systems, and Applications*, [Jay W. Dawson](#), Editors, paper 79140U (2011).
- [9] J. L. Wilson, C. Wang, A. E. Fathy, and Y. W. Kang, “Analysis of rapidly twisted hollow waveguides,” *IEEE Trans. Microwave Theory Tech.* **57**,130-139 (2009).
- [10] A. Nichlet, F. Zolla, and S. Guenneau, “Modelling of twisted optical waveguides with edge elements,” *Eur. Phys. J. Appl. Phys.* **28**, 153-157 (2004).
- [11] A. W. Snyder, and J. D. Love, “Reflection at a curved dielectric interface—electromagnetic tunneling,” *IEEE Trans. Microwave Theory Tech.* **MTT-23**, 134-141 (1975).
- [12] D. Marcuse, “Curvature loss formula for optical fibers,” *J. Opt. Soc. Am.* **66**, 216-220 (1976).
- [13] U. Peschel, T. Peschel, and F. Lederer, “A compact device for highly efficient dispersion compensation in fiber transmission,” *Appl. Phys. Lett.* **67**, 2111-2113 (1995).
- [14] J. E. Rothenberg and G. D. Goodno, " Advances and Limitations in Beam Combination of Kilowatt Fiber Amplifiers," *Proc. of SPIE Vol. 7686*.
- [15] G. D. Goodno *et al.* “Active phase and polarization locking of 1.4kW fiber laser”, *Optics Letters* **35** (10), 1542 – 1544 (2010)
- [16] G. Agrawal, *Nonlinear Fiber Optics*, Academic Press (1995)

- [17] J. Edgecumbe *et al.*, “kW-Class, narrow-linewidth counter-pumped fiber amplifiers”, SSDLTR Proc., June (2010)
- [18] J. Limpert, T. Schreiber, A. Liem, S. Nolte, H. Zellmer, T. Peschel, V. Guyenot, and A. Tünnermann, “Thermo-optical properties of air-clad photonic crystal fiber lasers in high power operation,” Opt. Express, 11, 2982 – 2990 (2003).
- [19] C. Robin, I. Dajani, C. Vergien, C. Zeringue, and T. M. Shay, “Experimental and theoretical studies of single frequency PCF amplifier with output of 400W,” Proc. of SPIE 7580, 75801I-1 -7580I-11 (2010).
- [20] A. Galvanauskas *et al.*, US Patent 7,492,508 B2
- [21] 11. Xiuquan Ma, I-Ning Hu, and Almantas Galvanauskas, “Propagation-length independent SRS threshold in chirally-coupled-core fibers”, Opt. Express 19, 22575-22581 (2011).

2. Suppression of Stimulated Brillouin Scattering in Optical Fibers and its Exploration

Report by P. Dragic

Abstract/Executive Summary

UIUC's contribution to this program has resulted in 13 published journal papers, 3 papers still in preparation based on work performed during the program, and 3 conference presentations. One PhD and one MS student were supported as part of this program. Two undergraduate researchers were supported, while one of them is the lead author of one of the papers in preparation. He is currently applying to graduate school and intends to study the area of Optics and Photonics. This program also saw two cross-program collaborative efforts (with B. Ward formerly at the Air Force Academy and J. Ballato at Clemson), which were initiated at JTO MRI reviews and resulted in publications.

Our main proposed task was to perform basic research on stimulated Brillouin scattering (SBS) and on designs for its suppression in large mode area (LMA) fibers. We contemplated designs that utilized acoustic profiling methods. However, due to the tight manufacturing tolerances required with some designs, especially for fibers in LMA form, precise understanding of dopants' effect on fiber acoustic properties was necessary.

We found that the literature contained little or no empirical data that could be trusted for use in fiber design. Therefore, in order to confidently design compositional profiles, and with initial feedback from Nufern about the difficulty and uncertainty in fabricating these designs, we tasked ourselves with improving the understanding of dopants and how they influence the basic materials properties of optical fibers.

Then, given that some work in the RIFL program resulted in fiber designs similar to those already contemplated for this program, we instead investigated glasses whose material properties are desirable for SBS suppression. This leads to the possibility of implementing LMA fibers with a low SBS gain that is independent of the core diameter, and that do not require complex acoustic profiling. Work as part of this program has led to a number of firsts, including a very powerful model for material (bulk) and waveguide Brillouin scattering. Some of these accomplishments are outlined below.

We made the first-known measurement of the Brillouin gain spectrum (BGS) in a rare earth-doped fiber. Rare earths cause a large broadening of the BGS and a reduction of the Brillouin gain. We found a rule-of-thumb Brillouin gain coefficient (BGC) of $\sim 1.5 \times 10^{-11}$ m/W in a 'typical' Al co-doped Yb LMA fiber, to be much less than was previously reported.

We developed a model that calculates the Brillouin gain coefficient (BGC) as a function of dopant concentration. This resulted in a new explanation of the 'anomalous' broadening of the BGS in single mode fibers based on a viscous acoustic-wave damping model. We showed that the viscosity model can be used in a variety of mode solvers to predict measured BGS and BGC very accurately. We showed that the spectral width of silica in fiber form is not anomalous, but instead is right where it should be. This

led to an explanation of the dependence of the Brillouin spectral width on acoustic mode number in optical fiber. We showed that the model can be expanded to 100% dopant endpoints, demonstrating the 'first-principle' nature of the model.

Next, we demonstrated the model of the BGS and BGC expanded to ternary glass systems. We made the first in-fiber observation and explanation, to the best of our knowledge, of a breakdown in the 'wavelength-squared law' of the Brillouin spectral width.

Cross-program collaborative efforts led to the first measurements of the BGS in YAG-derived fibers. During this program, we discovered and demonstrated the first dopant since Al that increases the acoustic velocity when added to silica. This led to an expanded list of dopants that can be used to accurately design optical fiber acoustic properties. We also made the first Yb:YAG-derived fiber amplifier measurements.

With the model proving to be very powerful, more advanced work was performed. We demonstrated the first accurate simulation of temperature and strain-dependencies of any-order acoustic mode for arbitrary doping profiles. This is particularly important if strain or temperature distributions are to be utilized to further suppress SBS in high power fiber laser systems. We also provided the first elucidation, to the best of our knowledge, of the photoelastic constants (p_{11} and p_{12}) of bulk P_2O_5 .

Other work was performed in the area of glass defects in rare earth doped optical fibers. We showed that the presence of rare earth dopants increases the concentrations of various glass defects in fiber. We also later showed that the rare earths are coordinated to these defects. Finally, we found that the concentration of these defects depends on the dopant, and may explain why some rare-earth doped fibers (such as Er-doped) do not exhibit photodarkening.

We believe that our work during this program has made a significant contribution to the understanding of Brillouin scattering, and how dopants can be applied to very precisely design optical fibers. Our results suggest that LMA Yb-doped optical fibers at the multi-kiloWatt level are possible, with the correct glass composition. Future work would include more investigation of novel materials and dopants, and the implementation of designs, including the investigation of novel fiber fabrication methods for complex and advanced glass systems.

Detailed Narrative

Investigation of stimulated Brillouin scattering (SBS) was a majority part of the contribution by the University of Illinois at Urbana-Champaign (UIUC) to this program. Some work was also done in the area of optical fiber defects in rare earth-doped fibers. Additionally, some system-level ideas were advanced thanks to work done during this program. A detailed description of the work performed in these areas is presented in this section.

A. SBS

Stimulated Brillouin Scattering (SBS) limits maximum achievable optical power for narrow-spectrum signals in fiber optic systems [1,2]. Therefore, suppression of SBS is crucial for the realization of very

narrow linewidth (< 200MHz), high power fiber lasers. A conventional method to suppress SBS is to broaden the laser spectrum so that the signal's effective linewidth is greater than that of the Brillouin gain spectrum [3-5]. Assuming Lorentzian spectra, the Brillouin gain coefficient (BGC) \tilde{g}_B scales with signal bandwidth according to

$$\tilde{g}_B = \frac{\Delta\nu_B}{\Delta\nu_B + \Delta\nu_l} g_B \quad (1)$$

where $\Delta\nu_l$ is the laser linewidth, $\Delta\nu_B$ is the Brillouin linewidth and g_B is the Brillouin gain for a signal spectrum. When $\Delta\nu_l \gg \Delta\nu_B$, SBS is effectively suppressed and other nonlinear effects, such as stimulated Raman scattering (SRS) with a significantly higher threshold than SBS, set the power limit. However, this SBS suppression method is not always suitable.

Other methods based on the acoustic waveguide properties of optical fiber have also been proposed. For example, a fiber with a varying core size in an acoustic guiding fiber chirps the Brillouin gain spectrum and reduces the peak Brillouin gain constant [6]. Varying the index of refraction [7] and inducing varying stresses (or temperature) in the fiber [8] have a similar effect of broadening the Brillouin gain spectrum. However, to achieve a large degree of SBS suppression, these techniques require a very large non-uniformity along the fiber length. This is both difficult and expensive to implement, and can negatively influence key optical properties.

A more recent method based on manipulating the acoustic wave-guiding properties of optical fiber through reducing the acousto-optic overlap integral by 1) drawing acoustic waves from the core of the fiber to an outer fiber region [9] or 2) manipulating the overlap between the optical and acoustic waves, both confined to the core, to be much reduced [10]. These were methods that we proposed investigating as part of this program.

One way or another, each of the 'fiber' SBS-suppression methods described in the previous two paragraphs requires relatively precise knowledge of how dopants influence the SBS characteristics of a fiber. In each case, fiber design can be implemented utilizing an appropriate arrangement of dopants that have known properties when mixed. Therefore, in order to determine these dopant properties, we first developed a system that can be used to measure the Brillouin gain spectra.

1. Development of the Experimental Apparatus

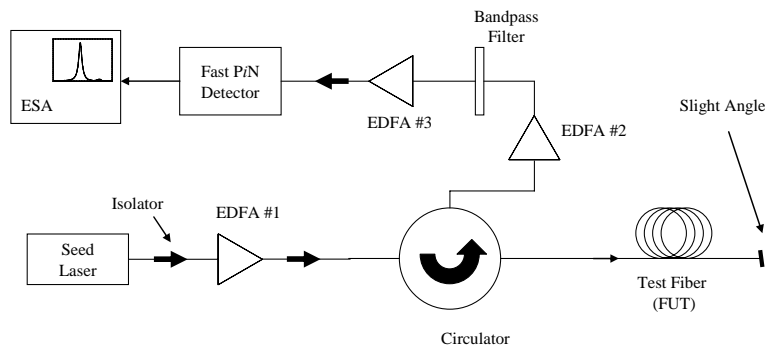


Fig. 1. Final apparatus developed to measure the Brillouin gain spectra of various fibers.

In order to capture precise Brillouin spectra, an optical heterodyne approach was adopted [11]. Fig. 1 shows a block diagram of the final experimental arrangement, after a considerable amount of optimization. An external-cavity laser diode seed (Agilent 81682A) operating at 15XX nm (tunable) is used. It has a measured spectral width of 85 kHz. Light from the seed laser is isolated and amplified by an in-house-built erbium doped fiber amplifier (EDFA).

The amplified seed signal is then passed through a circulator and then into the fiber under test (FUT). The Brillouin scattered (back-reflected) signal then passes through port 3 of the circulator and into a second EDFA. Output from the second stage then passes through a tunable bandpass filter to reject spontaneous emission from the second stage and is then amplified by a third and final amplifier stage with high gain. This signal is then sent into a fast detector (New Focus 1534) and then into an Agilent electrical spectrum analyzer.

In order to achieve a heterodyne measurement, some of the fundamental local-oscillator (LO) signal (the seeder) is still required. Therefore, in order to minimize the number of components used in the setup, the LO signal was taken by cleaving the output of the FUT at a slight angle to capture some (but not all) back-reflection. The Fresnel reflection from the end of the FUT was set to provide adequate signal to perform the heterodyne measurements, while not saturating the gain in the last amplifier.

To obtain these measurements, up to 100mW of power could be launched into the test fiber, However, depending on the testing case and fiber specifications, we were careful to avoid any gain narrowing effects in the BGS, so the launch power is always carefully limited. Fig. 2 shows a ‘typical’ high-quality Brillouin gain spectrum (BGS) obtained with the testing apparatus. We found that we could measure the BGS of fibers as short as ~1m and with core diameters up to at least 50 μ m. This system formed the backbone of our Brillouin scattering work.

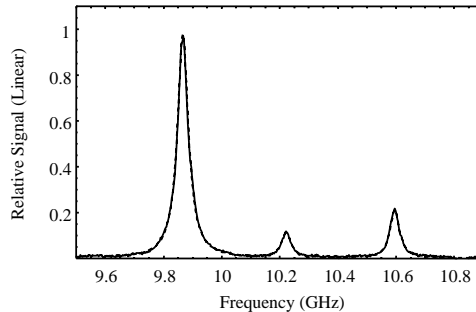


Fig. 2. ‘Typical’ high-quality BGS obtained from our measurement apparatus. This example is a heavily-Ge-doped silica fiber measured at 1555 nm.

In addition to this apparatus, a number of amplifiers were developed in order to test for the SBS threshold utilizing power transmission measurements, both at 15XX and 1064 nm. These were utilized throughout the program to determine the BGC for fibers under test. In addition, the layout described in Fig. 1 was adapted for use at 1064 nm for some measurements.

2. First Measurements

Key Achievements

- i) **First known measurement of the BGS in a rare earth-doped fiber. Rare earths cause a large broadening of the BGS.**
- ii) **Rule-of-thumb Brillouin gain coefficient (BGC) of $\sim 1.5 \times 10^{-11}$ m/W in a ‘typical’ Al co-doped Yb LMA fiber.**

We began by analyzing and comparing several Ge- and Nd-Ge-doped fibers that were already part of our internal stock of fibers to see how rare-earths influence the BGS. These results were published [U1]. Also, as proposed, we measured a series of Al co-doped Yb fibers from Nufern. However, these results remained unpublished due to proprietary issues by the manufacturer. A spectrum of a 35-micron Nufern Yb-doped fiber is provided as an example in Fig. 3.

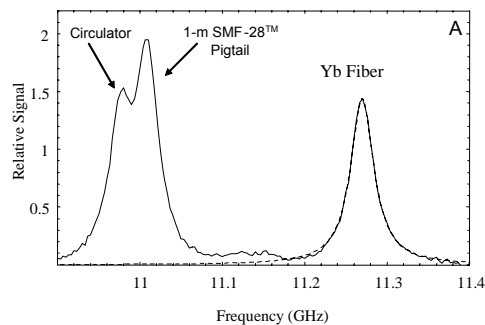


Fig. 3. BGS of a 35- μm Nufern Yb-Al co-doped fiber.

Our findings were that adding rare-earths to optical fiber broadens the BGS. In fact the BGS was found to broaden by about a factor of two for each weight percent of dopant, and that a good rule-of-thumb BGC for ‘typical’ Yb-doped fibers is $\sim 1.5 \times 10^{-11}$ m/W. This is due to a large acoustic-wave damping that is imparted by the rare earth. Our findings thus caused us to reconsider the effectiveness of the method described in [12], wherein by manipulating the doping profile of the core they realized a BGC of 0.9×10^{-11} m/W relative to an ‘expected’ value of 5.0×10^{-11} m/W; one that is widely reported in the literature [2]. We found that this ‘expected’ value is far too large, even for the bulk pure silica from which it is derived [2].

Another finding was that our measurements of the effect of Ge-doping on silica fiber acoustic velocities did not match others found in the literature [13]. Regardless of the manufacturer, our results were inter-consistent and different from those found elsewhere, and no clear consensus on how adding Ge exactly influences the acoustic velocity of silica could be found, other than it decreases it. It became very clear that the data found in the literature could not be trusted in designing a low-SBS fiber [14,15] since the available data is clearly unreliable.

Due to the complexity of the acoustically-profiled fibers that were proposed, that the profiles required tight tolerances to work, and that dopant data could not be trusted, we found it to be unwise to guess at compositions. As a result, we put more focus on understanding the dopants, their effects, and how they can be utilized in fiber design. This led to the development of the model presented in the next section.

3. A Model for Ge-doped Fibers

Key Achievements

- iii) **First model that calculates the Brillouin gain as a function of dopant concentration.**
- iv) **New explanation of the ‘anomalous’ broadening of the BGS in single mode fibers based on a viscous acoustic-wave damping model.**

Based on extensive experimental work, we developed the first model, to the best of our knowledge, which calculates the BGC for a Ge-doped fiber. This model can be applied to other dopants and systems of multiple dopants. This will be described later in the report. A shortened version of the model [U2] is described below.

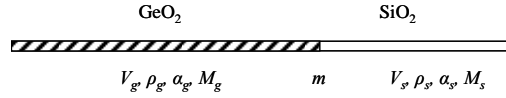


Fig. 4. Simplified separable-dopant model. This is an idealized view of a well-mixed glass.

In a well-mixed Ge-doped silica fiber, we may assume that a fraction m of the total volume is pure germania, as shown in Fig. 4. We can determine m in terms of the physical properties and $[Ge]$ (mol% of GeO_2) as

$$m = \frac{\frac{M_g}{M_s} \rho_s [Ge/100]}{\rho_g + [Ge/100] \left(\frac{M_g}{M_s} \rho_s - \rho_g \right)}. \quad (2)$$

Here, M is the molar mass, and subscripts s and g refer to silica and germania, respectively. We start with the average density for this glass, determined from Fig. 4 to be

$$\rho = m\rho_g + (1-m)\rho_s. \quad (3)$$

The acoustic velocity is found by determining a total ‘time-of-flight’ through both segments of fiber in Fig. 4

$$V_a = \frac{V_g}{\frac{V_g}{V_s} + m \left(1 - \frac{V_g}{V_s} \right)}. \quad (4)$$

To determine the spectral width as a function of $[Ge]$, we begin with the determination of an average acoustic damping coefficient in the two pure segments as a function of frequency. We obtain this by summing the attenuation in each segment to arrive at

$$\alpha_{ave} = \left(\nu_a / \nu_{SMF} \right)^2 \left[\alpha_g m + \alpha_s (1 - m) \right]. \quad (5)$$

The scaling term $(\nu_a / \nu_{SMF})^2$ accounts for the frequency-squared dependence of the intrinsic linewidth [5], which in turn is proportional to the damping coefficient. The acoustic frequency is that of the propagating acoustic mode in the mixed fiber, not that in the pure materials. A reference frequency must be selected at which the damping coefficient is defined, in this case arbitrarily the measured (our data) acoustic frequency of the L_{01} mode in SMF-28™ at 1534 nm. Thus, α_g and α_s are the values at acoustic frequency ν_{SMF} , or 11.008 GHz (regardless of the optical wavelength). Finally, we also know that the damping coefficient is related to the Brillouin spectral bandwidth (FWHM) as

$$\Delta \nu_B = \frac{V_a \alpha_{ave}}{\pi}. \quad (6)$$

Finally, the Brillouin gain coefficient is determined from the well-known equation (not considering the overlap integral, so that this is for the material alone),

$$g_B(\nu_B) = \frac{2\pi n^7 p_{12}^2}{c \lambda^2 \rho V_a \Delta \nu_B}. \quad (7)$$

Fig. 5 (a) provides a plot of Eqn. (6), while Fig 5 (b) provides a plot of Eqn. (7) for Ge-doped silica.

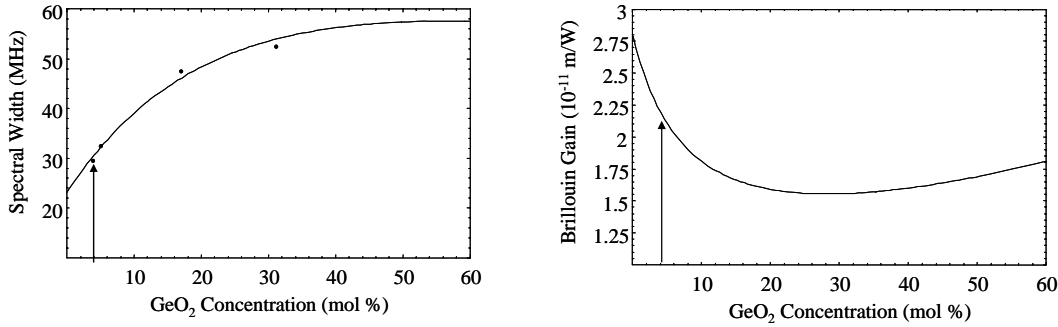


Fig. 5. (a) Spectral width vs. [Ge] and (b) g_B vs. [Ge] for Ge-doped silica. The arrow shows the position of Corning's SMF-28™ fiber.

We concluded that adding Ge to silica broadens the spectrum in a non-linear way, different from previous reports [13,16]. Spectral broadening results from the dynamic viscosity of germania that is about ten times that of silica. The non-linear nature of the spectral broadening is due to the fact that adding Ge to silica also decreases the acoustic velocity, thereby reducing the Brillouin frequency, and thus the acoustic damping coefficient, leading to the absolute minimum BGC observed in Fig. 5(b).

We believe that the 'anomalous broadening' observed in single mode fibers is not anomalous, but rather a consequence of doping. Germania has an acoustic-wave damping coefficient that is about 10

times larger than that of silica. While lengthwise variations in fiber can broaden the spectrum for long fibers [2], the broad spectra are not due to anomalous effects or the fiber's numerical aperture [17].

4. Validation

Key Achievements

- v) **Showed that the viscosity model presented above can be used in a variety of mode solvers to predict measured BGS and BGC very accurately.**
- vi) **Spectral width of silica in fiber form is not anomalous, but instead is right where it should be.**
- vii) **First explanation of the dependence of the Brillouin spectral width on acoustic mode number in optical fiber.**

Our results for the effect of Ge-doping on the acoustic velocity of silica were validated independently in [18]. Our own work to validate the model demonstrated that it can be used to calculate the BGS of a highly Ge-doped silica fiber utilizing both a step-wise approximation to the doping profile [U3] and a finite element analysis [U4]. The latter work was done in collaboration with Dr. Benjamin Ward, initiated at a JTO MRI Review. In principle, we showed that a doping profile, whether simplified or used exactly, can be converted into a set of velocity and spectral width (acoustic attenuation) profiles. How the acoustic modes overlap with these various regions gives rise to their observed spectral widths.

To expand on this, we have observed in both [U3] and [U4] that the Brillouin spectral width decreases with increasing mode number. In the case of these works, the higher-order acoustic modes (HOAMs) had greater overlap with regions of lower acoustic damping (larger relative concentration of silica), thus possessing narrower spectral widths. This represents, to the best of our knowledge, the first explanation of this phenomenon and the very first time a radial spectral width profile was applied to an SBS analysis.

5. Use of an Expanded Model

Key Achievements

- viii) **Comparison of models show that they can be expanded to 100% dopant endpoints.**
- ix) **Demonstration of model of the BGS and BGC including multiple dopants.**
- x) **First observation of a breakdown in the 'wavelength-squared law' of the Brillouin spectral width.**

B_2O_3 was previously determined to have a very large acoustic damping coefficient relative to silica [19], and this can be utilized to suppress SBS. Thus, a B-Ge-codoped silica fiber offered a reasonable way to test the model in a ternary system. To determine the influence of B_2O_3 on silica fiber properties, B_2O_3 fibers were drawn at four different temperatures from the same preform [U5] by Nufern. The different temperatures were chosen (1900 °C, 1950 °C, 2050 °C, and 2150 °C) in order to investigate the effect of draw temperature on fiber properties. The concentrations of B_2O_3 and GeO_2 in the core were measured via EPMA by Nufern to be $6.2 \pm 5\%$ wt% and $10.8 \pm 2\%$ wt%, respectively. Ge was added to raise the refractive index relative to the pure silica cladding. Fig. 6 provides the refractive index and acoustic velocity profiles for one of the fibers.

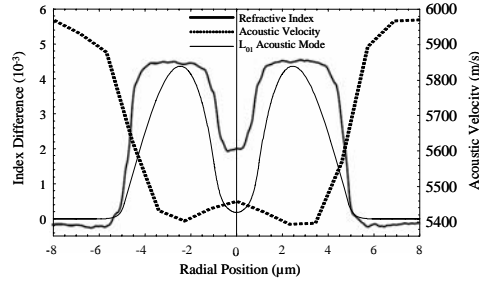


Fig. 6. Refractive index and acoustic velocity profiles of the fiber drawn at 2150 °C along with its calculated fundamental acoustic mode excited at an optical wavelength of 1534 nm.

First, it was found that, contrary to textbook knowledge [2], the Brillouin spectral width does not always follow an inverse-wavelength-squared dependence [U6]. In fact, we showed that only when the viscous damping processes have a peak attenuation at cryogenic temperatures (far from room temperature) does the wavelength-squared model hold. This is valid for ‘normal’ materials such as GeO_2 and SiO_2 . When the peak lies at elevated temperatures (such as for B_2O_3 [19]), this model breaks down. This leads to the Brillouin spectral width of B-doped fibers exhibiting the anomalous behavior of broadening with increasing temperature [U5], as compared, for example, with that of Ge-doped fibers whose spectra narrow with increasing temperature [16]. This can be a beneficial feature for high-power fiber lasers.

Next, the four different temperatures mainly showed that the acoustic velocity of the material decreases with decreasing draw temperature (meaning a larger draw tension). This is mainly due to a residual strain that remains after quenching [20]. Secondly, the spectral width of the BGS changes by very little, suggesting that despite the draw temperatures, the fiber fictive temperature remains about the same, probably close to the glass transition temperature (~ 1100 °C).

In order to simulate this ternary system, we expanded the model presented in subsection 3 above to a summation. As an illustrative example, the acoustic velocity summation becomes

$$V_a = \left(\sum_{i=1}^3 \frac{m_i - m_{i-1}}{V_{ai}} \right)^{-1} \quad (6)$$

where the fiber can be modeled as a separable group of multiple segments as shown in Fig. 4, and the m 's represent the positions of the boundaries. These calculations led to the set of curves that describes the BGC for any B-Ge-silica composition shown in Fig. 7. In summary, the results show that the BGC (for the material alone, not incorporating any addition SBS suppression methods) can fall to below 0.5×10^{-11} m/W for Yb-based systems and below 0.3×10^{-11} m/W for Tm systems (due to the anomalous behavior of B_2O_3). This suggests a promising development path however it is unclear if the spectroscopy of the rare earth would be adversely affected.

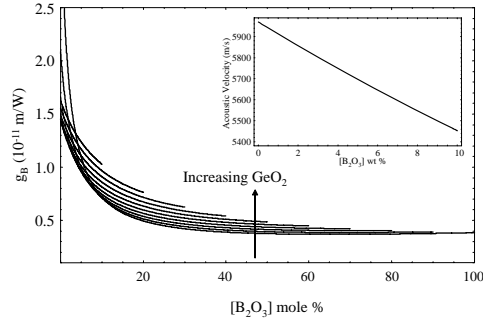


Fig. 7. Calculated Brillouin gain coefficient as a function of boric oxide concentration (mole%) for several GeO_2 concentrations, increasing from 0 to 90 mole % in steps of 10 mole%. The inset shows the acoustic velocity of B-doped silica (no GeO_2) as a function of B dopant.

While the model we have been using does seem to match experimental observations very well, it breaks down when inter-bonding effects alter the contributions of the individual species. Thus, in these cases, the more complex molecules can be treated as a single species in the model [U7]. Also, while the model presented above is the first, to the best of our knowledge, to provide a calculation of the BGC, it is not the only one to provide the acoustic velocity of a mixed material [21]. We performed a comparison of these models, and the results were published in [U8]. While it was found that the models can be forced to provide results consistent with experimental observations, the model of subsection 3 utilized fitting parameters most consistent with data found in the literature for the bulk material constituents.

6. Novel Materials

Key Achievements

- xi) **First measurements of the BGS in YAG-derived fibers.**
- xii) **Discovery of the first dopant since Al that increases the acoustic velocity when added to silica.**
- xiii) **Expanded elemental influences on the acoustic and optical indices.**

Clemson through another JTO program developed glassy fibers derived from doped YAG crystals. Details on the process can be found elsewhere [22]. Interestingly, these fibers contain much less silica than usually found in aluminosilicate Yb-doped fibers. This represented an opportunity to investigate the BGC of materials that have low photoelastic constants [23] as well as increased acoustic-wave damping, and low silica content. It was found that ‘typical’ YAG-derived fibers had BGC values in the vicinity of 0.5×10^{-11} m/W.

The multi-component model described in subsection 5 above was used to model the YAG-derived fiber system. We found that the value of BGC decreases rapidly with increasing Y and Al concentrations [U7], suggesting another promising development path. Also, we found that Y increases the acoustic velocity when doped in silica. This is only the second dopant shown to have this effect on silica-based fibers. Decades ago, Al was found to be the first dopant with this property. During this program, we have

added four elements, Y, Nd, Er, and Yb, to the well-known chart representing the effect of dopants on the optical and acoustic indices. This is shown in Table I. These results are based on experimental work on glass fiber. Utilizing the model developed during this program and bulk data found in the literature, this list grows considerably.

	Ge	P	Ti	B	F	Al	Y	Nd	Er	Yb
n_o	↑	↑	↑	↓	↓	↑	↑	↑	↑	↑
n_a	↑	↑	↑	↑	↑	↓	↓	↑	↑	↑

Table I.

Expanded effect

of dopant on the optical (n_o) and acoustic (n_a) indices.

7. On-Going and Future Work

Key Achievements

- xiv) **YAG-derived fiber amplifier experiments.**
- xv) **First calculation of temperature and strain-dependencies of any-order acoustic mode frequency for arbitrary doping profiles.**
- xvi) **First elucidation, to the best of our knowledge, of the photoelastic constants (p_{11} and p_{12}) of bulk P_2O_5 .**

Work is currently underway to characterize the amplifier performance of YAG-derived fibers. A key goal is to validate BGC measurements on the fibers with power transmission data. To continue in this area, fiber designs with increased Y and Al concentrations should be considered, and dual-cladding designs can be contemplated.

We consider the model described in subsection 3 to be very strong, and we have since expanded it to include both temperature- and strain-dependencies (i.e. dependence of the Brillouin frequency shift on applied temperature or strain). The simplest form of this model is to start with a step-wise approximation to the acoustic and optical profiles, and to apply a temperature- and/or strain-dependence to each of the bulk dopants. With this, one can calculate the effectiveness of applied strain or temperature gradients to suppress SBS in high-power fiber amplifiers for arbitrary dopant profiles. Utilizing this expanded model we have analyzed a heavily P-doped fiber and have shown that it very accurately calculates the unique temperature coefficients of all four measured acoustic modes [U9] (to within 2% error). Work is currently underway for the strain, and we believe for the first time, to the best of our knowledge, we have elucidated the photoelastic constants p_{11} and p_{12} of bulk P_2O_5 . This has eluded the community due to the instability of bulk P_2O_5 due to its being one of the most hygroscopic known materials [24].

The work done during this program should be expanded to include other less-common dopants and glass compositions. There is numerous, reliable, bulk-material data available in the literature, and many of them show significant promise if available in fiber form. This may require the development of new fiber fabrication and glass processing methods. And, there is the strong possibility of discovering new

materials that possess attributes more desirable for the suppression of SBS. In particular the utilization of low photoelastic-constant and large acoustic-wave damping-coefficient materials provide a very promising path towards low-SBS fibers with longitudinal uniformity and independence of the core diameter. This approach appears to be well-suited for CCC-type fibers.

B. Other Work

A very brief description of some other work performed during this program is provided in this section. These include investigations of optical glass defects and a remote sensing system.

1. Glass Defects

Key Achievements

- xvii) Showed that the presence of rare earth dopants increases the concentrations of various glass defects in fiber.**
- xviii) Showed that the rare earths are coordinated to these defects.**
- xix) The concentration of these defects depends on the dopant, and may explain why some rare-earth doped fibers (such as Er-doped) do not exhibit photodarkening.**

In the course of testing a narrow-linewidth pulse amplifier, visible (mainly reds and yellows) were observed being emitted by the fiber at high peak power. A search in the literature offered no description of this process in a fiber amplifier. Further investigation suggested that these observations were due to non-bridging oxygen hole centers (NBOHC) through a two-photon absorption process resulting in red photoluminescence [U10].

BOHC defects are broken-bond defects represented chemically as $[\equiv \text{Si} - \text{O} \bullet]$ where the symbol \equiv represents bonding to three oxygens and the symbol \bullet represents an unpaired electron. These centers are highly localized, have luminescence near 1.9 eV (thus otherwise known as *R*-centers or red centers), and absorption near 2.0eV. Photoluminescence may be attributed to a charge transfer transition between a non-bonding orbital of the non-bridging oxygen and one of the three ligand oxygens. NBOHC centers arise from the presence of dopants or contaminants that are network modifiers, such as expected from a large concentration of a rare earth dopant and requisite co-dopants. Consequently, an analysis on a number of passive and Yb-doped fibers disclosed that the addition of rare-earths to silica greatly increases the concentration of NBOHCs [U11], suggesting that they are coordinated in the network. Furthermore, this also suggests that an energy transfer (upconversion, transfer from multiple Yb sites to a defect center) process is possible for pumping defects in the glass.

As what was found with NBOHC may have implications in the photodarkening process of Yb-doped fibers at high power, several other experiments were performed to examine the presence of oxygen deficiency center (ODC) defects. Two main forms of ODC defects appear to be feasible. The first is known as ODC(I) and consists of an oxygen vacancy at a location of two bonded silicon atoms, represented chemically as $\equiv \text{Si} - \text{Si} \equiv$ (also known as the 'relaxed' vacancy). The other is type ODC(II) (B2 band) with two feasible configurations. The first is the silylene-type defect, represented as $:\text{Si} =$,

containing two oxygen vacancies on a single silicon atom. The other is represented as an oxygen vacancy on two unbonded Si sites, $\equiv\text{Si}\dots\text{Si}\equiv$ (the ‘unrelaxed’ vacancy). Our studies involved the ODC(II) type since it is well known to be involved in defect inter-conversion [25,26].

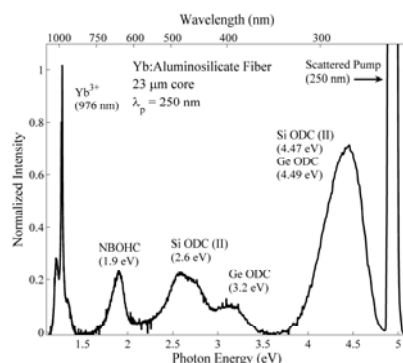


Fig. 8. Representative emission spectrum for a Yb-doped aluminosilicate fiber photoexcited at 250 nm (third harmonic of Ti:sapphire at 750 nm). Prominent features are identified, virtually all of which emanate from intrinsic defects in silica.

A series of experiments have shown that there exists an energy transfer mechanism (ODC→Yb) when pumping the ODC near 5 eV [U12]. A ‘typical’ spectrum of an Yb-doped fiber pumped at 248nm is shown in Fig. 8, along with the identifiable luminescence features. This was shown to be further evidence of a coordination of the rare earth dopant to optically-active defects. Energy transfer from multiple Yb sites can result in excitation of these defects, and possibly lead to color center formation or inter-conversion of defects.

We have subsequently found a linear relationship between the Yb dopant and defect concentrations in Yb-doped fibers, and we have been able to elucidate a defect concentration in Yb-doped fibers, for the first time to the best of our knowledge. We have also discovered that in Er-doped fibers, the defect concentration is far less than that of Yb-doped fibers. This may explain why photodarkening is not usually observed in Er-doped fibers. Work is ongoing to explain our observations, and a manuscript is in preparation.

2. He Lidar

A graduate student (PhD 2009) partly supported by this program leveraged some of the work done to develop a narrow-linewidth laser transmitter for the detection of upper-atmospheric helium for his PhD thesis [U13]. In the range of 300 – 1000 km altitude, atomic He is present, and is believed to contribute significantly to the global transport of energy. However, its time- and space-varying atmospheric concentration is not known and has to-date never been successfully measured. This work may open the door to these measurements for the very first time. Additionally, similar to the Na guide-star (at ~ 90 – 100 km in altitude), this work may represent a path to achieving a guide-star much further into space. This system may also lead to the possibility of space weather predictions at satellite-altitudes.

UIUC References

- [U1] P.D. Dragic, "Brillouin Spectroscopy of Nd-Ge co-doped Silica Fibers," *Journal of Non-Crystalline Solids*, vol. 355, pp. 403-413 (2009).
- [U2] P.D. Dragic, "Simplified model for the effect of Ge doping on silica fibre acoustic properties," *Electronics Letters*, vol. 45, iss. 5, pp. 256-257, 26 February 2009.
- [U3] P.D. Dragic, "Estimating the Effect of Ge Doping on the Acoustic Damping Coefficient via a Highly Ge-Doped MCVD Silica Fiber," *Journal of the Optical Society of America B*, vol. 26, no. 8, pp. 1614 – 1620, August 2009.
- [U4] P.D. Dragic and B.G. Ward, "Accurate Modeling of the Intrinsic Brillouin Linewidth via Finite Element Analysis," *IEEE Photonics Technology Letters*, vol. 22, no. 22, pp. 1698 – 1700, 15 November, 2010.
- [U5] P.D. Dragic, "Brillouin Gain Reduction Via B₂O₃ Doping," *Journal of Lightwave Technology*, vol. 29, no. 7, pp. 967 – 973, 2011.
- [U6] P.-C. Law and P.D. Dragic, "Wavelength dependence of the Brillouin spectral width of boron doped germanosilicate optical fibers," *Optics Express*, Vol. 18, no. 18, pp. 18852 – 18865, August, 2010.
- [U7] P. Dragic, P.-C. Law, J. Ballato, T. Hawkins, and P. Foy, "Brillouin spectroscopy of YAG-derived optical fibers," *Optics Express*, vol. 18, no. 10, pp 10055 – 10067, 2010.
- [U8] P.D. Dragic, "The Acoustic Velocity of Ge-Doped Silica Fibers: A Comparison of Two Models," *International Journal of Applied Glass Science*, Vol. 1, no. 3, pp. 330 – 337, September 2010.
- [U9] P.-C. Law, Y.-S. Liu, A. Croteau, and P.D. Dragic, "Acoustic coefficients of P₂O₅-doped silica fiber: acoustic velocity, acoustic attenuation, and thermo-acoustic coefficient," *Optical Materials Express*, vol. 1, no. 4, pp. 686-699, 2011.
- [U10] P.D. Dragic, "Observation of NBOHC Excitation in Pulsed Yb-Doped Fiber Amplifiers," *IEEE Photonics Technology Letters*, vol. 20, no. 21, pp. 1760-1762, 1 Nov. 2008.
- [U11] Peter D. Dragic, Chad G. Carlson, and André Croteau, "Characterization of defect luminescence in Yb doped silica fibers: part I NBOHC," *Optics Express*, vol. 16, no. 7, March 2008, pp. 4688-4697.
- [U12] C.G. Carlson, K.E. Keister, P.D. Dragic, A. Croteau, and J.G. Eden, "Photoexcitation of Yb-Doped Aluminosilicate Fibers at 250nm: Evidence for Excitation Transfer From Oxygen Deficiency Centers To Yb³⁺," *Journal of the Optical Society of America B*, vol. 27, no. 10, pp. 2087 – 2094, October 2010.
- [U13] **Invited Paper.** C.G. Carlson, P.D. Dragic, R.K. Price, J.J. Coleman, and G.R. Swenson, "A narrow-linewidth, Yb fiber-amplifier-based upper atmospheric Doppler temperature lidar," *IEEE Journal of Selected Topics in Quantum Electronics*, vol. 15, no. 2, pp. 451 – 461, March/April 2009.

Conference Papers

- [1] P.D. Dragic, "Proposed Model for the Effect of Ge-Doping on the Acoustic Properties of Silica Fibers" *presented at OFC/NFOEC 2009*, paper OWU4.
- [2] C.G. Carlson, K.E. Keister, J.G. Eden, and P.D. Dragic, "Defect Luminescence Spectroscopy in Yb Co-Doped Silica Fibers," *presented at Photonics West 2009*, paper 7195-29.
- [3] C.G. Carlson, P.D. Dragic, B.W. Graf, R.K. Price, J.J. Coleman, and G.R. Swenson, "High-power Yb-doped fiber laser-based lidar for space weather," *presented at SPIE Photonics West 2008*, paper 6873-19, 22 January, 2008.

Other References

- [1] R.G. Smith, "Optical power handling capacity of low loss optical fibers as determined by stimulated Raman and Brillouin scattering," *Appl. Opt.*, **11**, 2489-2494 (1972).
- [2] G.P. Agrawal, *Nonlinear Fiber Optics*, (Academic Press, 1995), Chapter 9.
- [3] A. Hadjifotiou and G.A. Hill, "Suppression of stimulated Brillouin backscattering by PSK modulation for high-power optical transmission," *IEE Proc. J* **133** 256-258 (1986).
- [4] L. Eskildsen, P.B. Hansen, U. Koren, B.I. Miller, M.G. Young, and K.F. Dreyer, "Stimulated Brillouin scattering suppression with low residual AM using a novel temperature wavelength-dithered DFB laser diode," *Electron. Lett.* **32**, 1387-1389 (1996).
- [5] Y.K. Chen, Y.L. Liu, and C.C. Lee, "Directly modulated 1.55 μm AM-VSB video EDFA-repeated supertrunking system over 110km standard singlemode fibre using split-band and wavelength division multiplexing techniques," *Electron. Lett.* **33**, 1400-1401 (1997).
- [6] K. Shiraki, M. Ohashi, and M. Tateda, "Suppression of stimulated Brillouin scattering in a fibre by changing the core radius," *Electron. Lett.* **31**, 668-669 (1995).
- [7] M. Ohashi and M. Tateda, "Design of a strain-free-fiber with nonuniform dopant concentration for stimulated Brillouin scattering suppression," *J. Lightwave Technol.* **11**, 1941-1945 (1993).
- [8] N. Yoshizawa, T. Horiguchi, and T. Kurashima, "Proposal for stimulated Brillouin scattering suppression by fibre cabling," *Electron. Lett.* **27**, 1100-1101 (1991).
- [9] P.D. Dragic, C.-H. Liu, G.C. Papen, and A. Galvanauskas, "Optical Fiber With an Acoustic Guiding Layer for Stimulated Brillouin Scattering Suppression," in *CLEO/QELS 2005*, Vol. 3 of 2005 Conference on Lasers and Electro-Optics, Paper CThZ3.

- [10] A. Kobayakov, S. Kumar, D. Chowdhury, A.B. Ruffin, M. Sauer, S. Bickham, and R. Mishra, "Design concept for optical fibers with enhanced SBS threshold," *Opt. Exp.* **13**, 5338-5346 (2005).
- [11] R.W. Tkach, A.R. Chraplyvy, and R.M. Derosier, "Spontaneous Brillouin scattering for single-mode fiber characterization," *Electron. Lett.* **22**, 1101 – 1113 (1986).
- [12] S. Gray, A. Liu, D.T. Walton, J. Wang, M.-J. Li, X. Chen, A. Ruffin, J. A. DeMeritt, and L.A. Zenteno, "502 Watt, single transverse mode, narrow linewidth, bidirectionally pumped Yb-doped fiber amplifier," *Opt. Exp.*, vol. 15, no. 25, pp. 17044-17050, 2007.
- [13] Y. Koyamada, S. Sato, S. Nakamura, H. Sotobayashi, and W. Chujo, "Simulating and Desinging Brillouin Gain Spectrum in Single-Mode Fibers," *J. Light. Technol.*, vol. 22, no. 2, pp. 631-639, 2004.
- [14] C.K. Jen, "Similarities and differences between fiber acoustics and fiber optics," *Proceedings of the IEEE Ultrasonics Symposium*, vol. 1985, pp. 1128-1133, 1985.
- [15] N. Shibata, Y. Azuma, T. Horiguchi, and M. Tateda, "Identification of longitudinal acoustic modes guided in the core region of a single-mode optical fiber by Brillouin gain spectra measurements," *Optics Letters*, vol. 13, no. 7, pp. 595-597, July 1988.
- [16] M. Niklès, L. Thévenaz, and P.A. Robert, "Brillouin Gain Spectrum Characterization in Single-Mode Optical Fibers," *J. Light. Technol.*, vol. 15, no. 10, pp. 1842-1851, 1997.
- [17] V.I. Kovalev and R.G. Harrison, "Waveguide-induced inhomogeneous spectral broadening of stimulated Brillouin scattering in optical fiber," *Opt. Lett.*, vol. 27, no. 22, pp. 2022-2024, 2002.
- [18] S. Herstrøm, L. Grüner-Nielson, and B. Pálsdóttir, "Acoustic index of Ge-doped optical fibers," *Opt. Lett.*, vol. 34, no. 23, pp. 3689-3691, 2009.
- [19] R.E. Youngman, J. Kieffer, J.D. Bass, and L. Duffrène, "Extended structural integrity in network glasses and liquids," *J. Non-Cryst. Sol.*, vol. 222, pp. 190-198, 1997.
- [20] W. Zou, Z. He, A.D. Yablon, and K. Hotate, "Dependence of Brillouin Frequency Shift in Optical Fibers on Draw-Induced Residual Elastic and Inelastic Strains," *Phot. Tech. Lett.*, vol. 19, no. 8, pp. 1389-1391, 2007.
- [21] A. Makishima and J.D. Mackenzie, "Calculation of bulk modulus, shear modulus, and Poisson's ratio of glass," *J. Non-Cryst. Sol.*, vol. 17, pp. 147-157, 1975.
- [22] J. Ballato, T. Hawkins, P. Foy, B. Kokuoz, R. Stolen, C. McMillen, M. Daw, Z. Su, T.M. Tritt, M. Dubinskii, J. Zhang, T. Sanamyan, and M.J. Matthewson, "On the fabrication of all-glass optical fibers from crystals," *J. Appl. Phys.*, vol. 105, pp. 053110-1-9, 2009.
- [23] V.R. Johnson and F.A. Olson, "Photoelastic Properties of YAG," *Proc. IEEE*, Vol. 55, pp. 709 – 710 (1967).

- [24] V.V. Brazhkin, J. Akola, Y. Katayama, S. Kohara, M.V. Kondrin, A.G. Lyapin, S.G. Lyapin, G. Tricot, and O.F. Yagafarov, "Densified low-hygroscopic form of P2O5 glass," *J. Mater. Chem.*, vol. 21, pp. 10442-10447, 2011
- [25] J.W. Lee, G.H. Sigel and J. Li, "Processing-induced defects in optical waveguide materials," *J. Non-Cryst. Solids*, vol. 239, pp. 57-65, 1998.
- [26] H. Imai, K. Arai, J. Isoya, H. Hosono, Y. Abe, and H. Imagawa, "Generation of E' centers and oxygen hole centers in synthetic silica glasses by γ irradiation," *Phys. Rev. B*, vol. 48, pp. 3116-3123 (1993).

3. High Brightness Pump Diode Development

Report of Fraunhofer, Center for Laser Technology, Stefan Heinemann

Duration: Oct. 2005 to Sept. 2011

Summary

High brightness pump diode lasers based on single emitter diodes of unprecedented performance were developed and a total of 4.2kW of pump power was installed at the laboratories of the University of Michigan. The first six (6) turn key systems deliver a total of 2.1 kW with an average power of 350W from a 200 μ m fiber with 0.2 NA for each unit. The second set of three (3) turn key systems delivers 700W from a 200 μ m fiber (0.2 NA) for each unit. Further, these units comprise the unique feature of an integrated beam switch allowing to either deliver 140W from each of the six (6) 100 μ m fibers (0.2NA) or 700W from one (1) 200 μ m fibers (0.2NA) and simultaneously 140W from one (1) 100 μ m fibers (0.2NA). These units are also very compact and comprise sophisticated controls and communication (CanBus) protocol.

Automated packaging technologies were also developed allowing consistent quality and short production time. A precision reflow process attaches up to 13 single emitter diodes with a tolerance of ± 5 μ m in a single manufacturing sequence. Automated lensing procedures and equipment was developed for fast and repeatable alignment of micro-lenses used for collimating the light from individual single emitter diodes. The developed manufacturing processes and equipment are worldwide unique and are now being adapted by several diode laser suppliers.

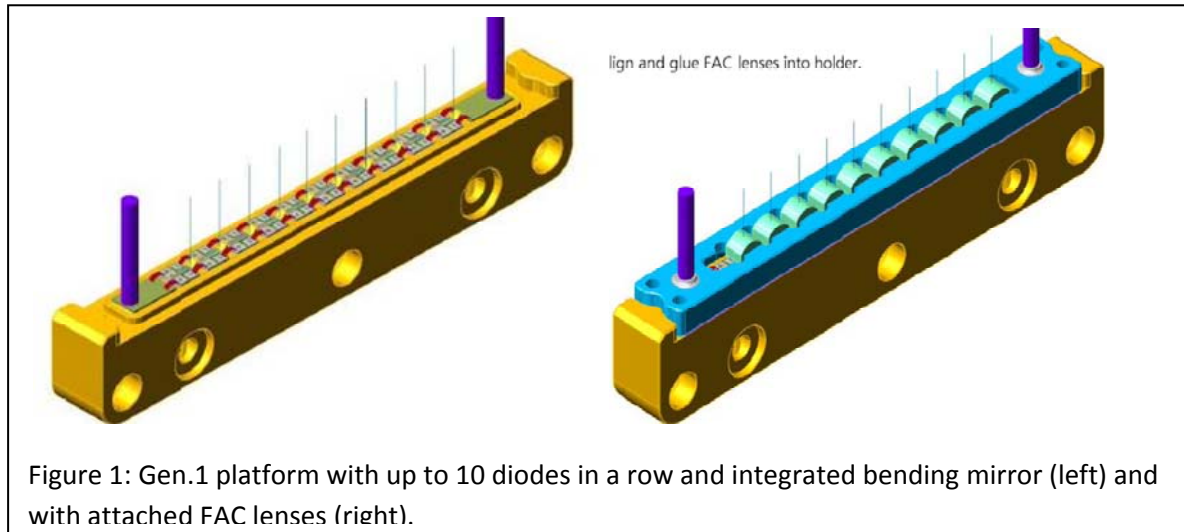
The work was complemented by support from DARPA, the State of Michigan and private industry.

Ultra High Brightness Diode Laser

Single emitter diodes enable highest brightness and power among all commercial diode lasers, since the output power from a given size facet is typically limited by temperature of the pn junction and not by catastrophic optical damage (COD). The thermal cross talk of bars and also its smile due to CTE mismatch between diode and heatsink are eliminated. Commercial single emitter diodes emit 11W from a 100 μ m aperture with a typical beam quality of $M^2=20$, while in fast axis, the beam is diffraction limited. This compares to about 5W from the size same emitter in a bar. Power scaling is achieved by stacking multiple single emitters in fast axis. Twelve single emitters can be efficiently stacked in fast axis to achieve a symmetric beam quality in both axis including manufacturing tolerances. A subsequent proprietary optical element performs optical stacking, slow axis collimation and beam cleaning in a single element (Figure 1). Optical losses and assembly time associated with conventional beam symmetrization is eliminated.

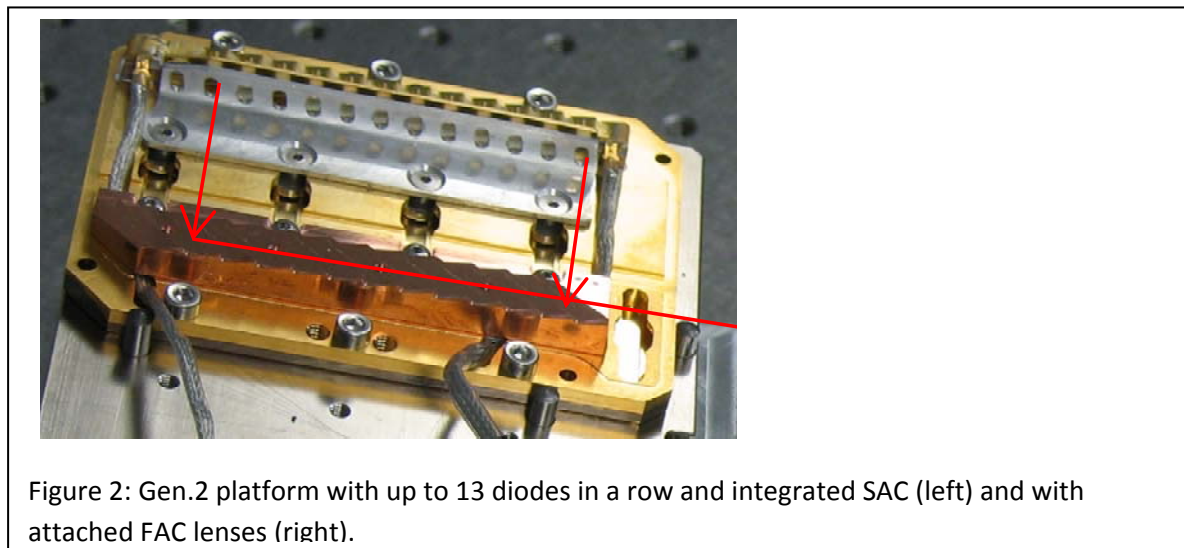
Two design iterations of the platform were developed over the course of the program. The first design uses FACs with a 2.7mm focal lens leading to a SAC with 115 mm focal lens that is imaged onto the end of a 200 μ m fiber with a 175 mm focusing parabola. The platform combines up to 10 diodes in a single

row and bending mirrors are integrated before the FAC to direct the beam perpendicular to the mounting plate of the diodes. (Fig. 1).



This approach is scalable to surface mount technology of large quantities, but results in a bulky laser system due to focal lenses with large focal lengths.

The second generation design uses a FAC of 0.9mm focal length and integrates the SAC with 38mm focal length into the platform, which is focused onto the end of a 200 μ m fiber with a 58 mm focal lens (Fig.2). The platform is either conduction or direct water cooled.



The SAC array of Gen.1 platform collimates and stacks 60 individual diode lasers. 5 platforms are therefore arranged in a 2 D stepped array and subsequently interleaved and collimated by the SAC (Fig.3).

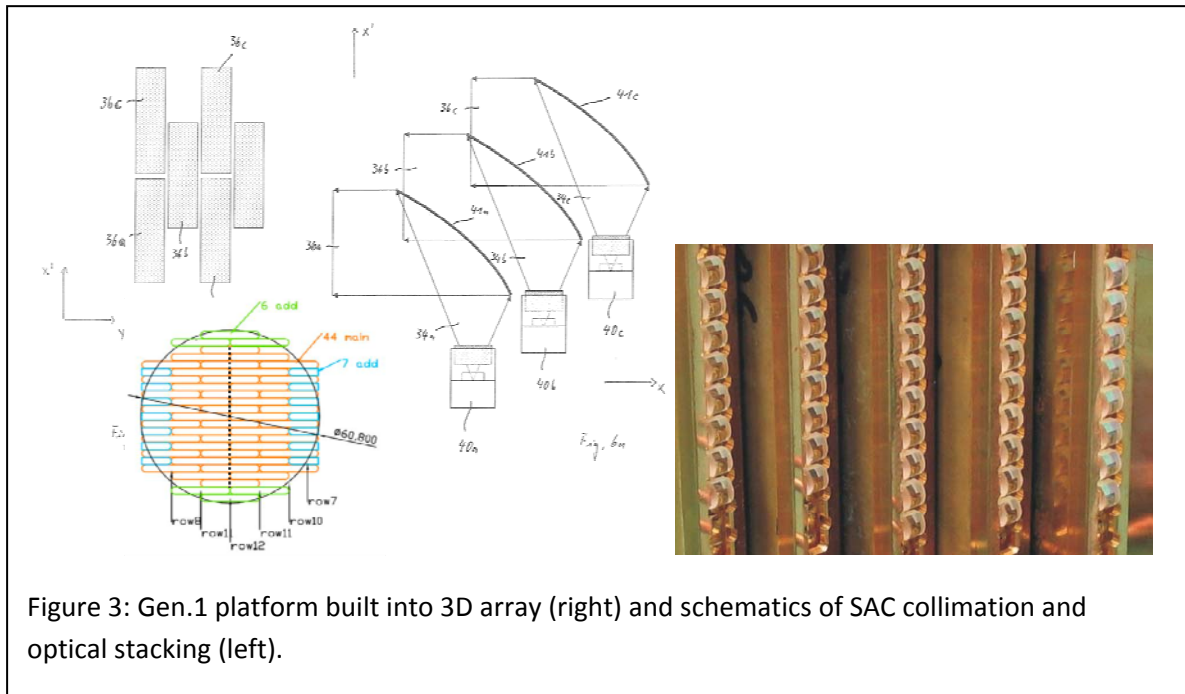


Figure 3: Gen.1 platform built into 3D array (right) and schematics of SAC collimation and optical stacking (left).

Both designs launch 120 single emitters into a 200 μ m fiber, 0.2 NA. Batch processing and/or automated lensing is paramount to enable the required precision and consistency. The two core manufacturing processes are a precision reflow process positioning all diodes of a platform with less than $\pm 5\mu$ m in slow axis direction and automated fast axis lensing. The accuracy of the reflow process is enabled by dedicated tooling pressing the submounts against a hardstop during the soldering process (Fig. 4)

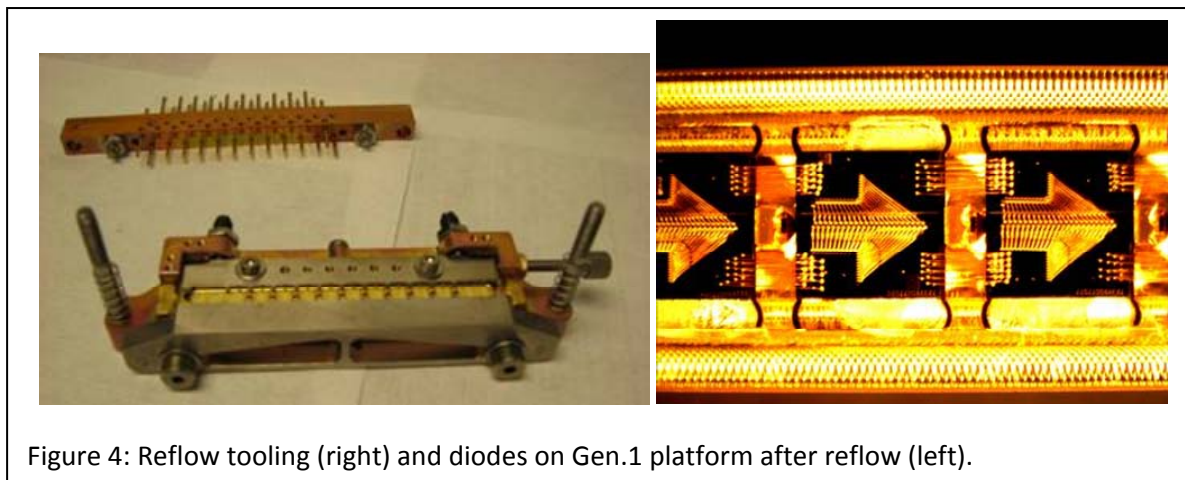


Figure 4: Reflow tooling (right) and diodes on Gen.1 platform after reflow (left).

A high precision lensing system was developed for alignment of the FACs. The near and farfield are simultaneously taken by cameras and image processing is deployed for automated alignment in less than

1.5 minutes per lens in 5 axis. Pointing and collimation errors were proven to be less than 10% of targeted spot size.

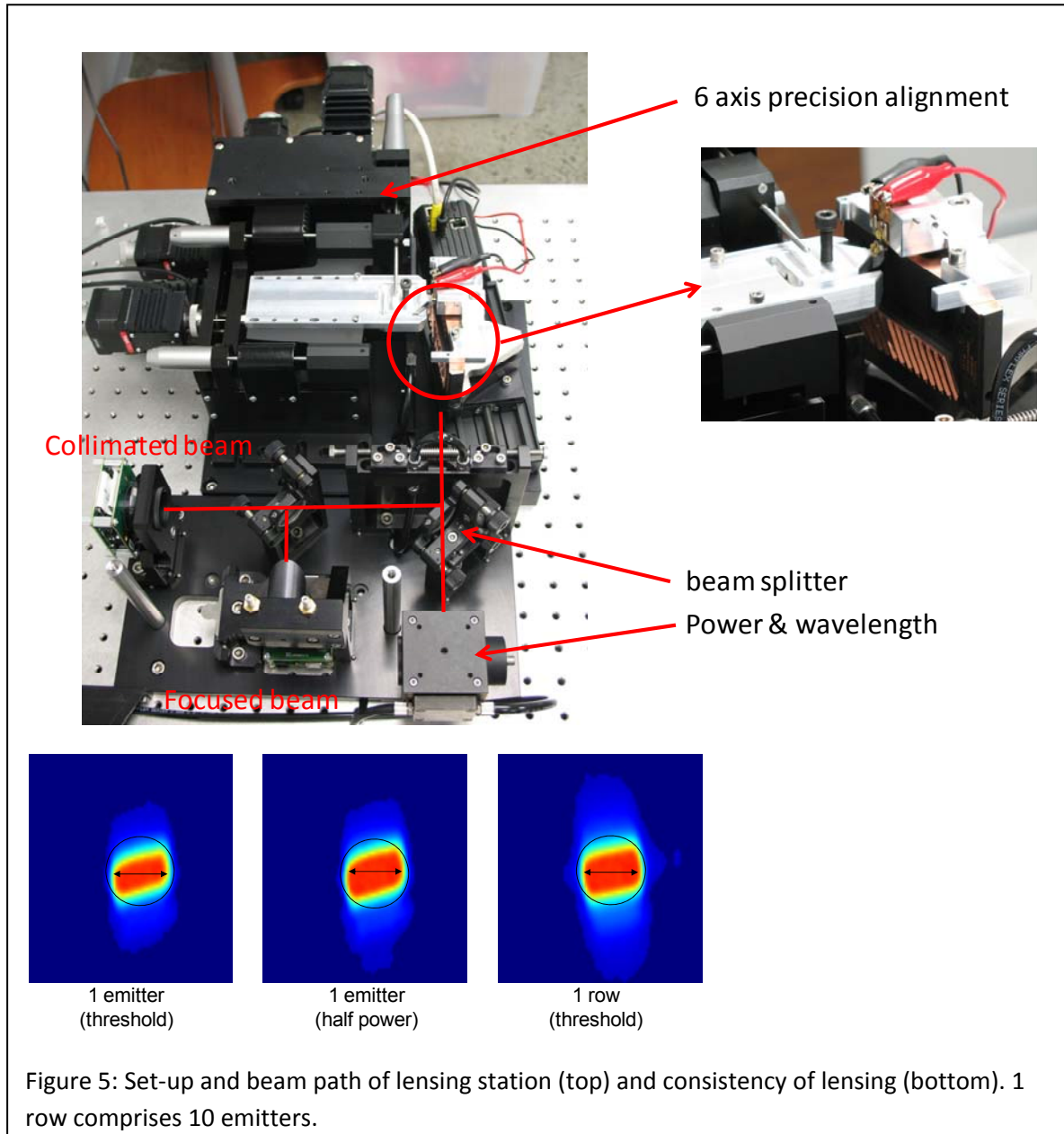


Figure 5: Set-up and beam path of lensing station (top) and consistency of lensing (bottom). 1 row comprises 10 emitters.

After lensing and optical stacking, polarization multiplexing is deployed. Gen.1 combines two 3D arrays, while Gen.2 combines two platforms and integrates the controller in one module (Fig.6). A Gen.1 3D array emits about 350W with 20 mm*mrad and a Gen.2 module emits 200W with 7 mm*mrad and smaller footprint.

Gen.1 uses a PC based controller and a Labview based user interface. Three user interfaces allow simultaneous or individual operation of 6 turnkey systems from different locations. Gen.2 has microcontrollers integrated into the diode platforms and uses a CanBus to communicate with the user

interface. The latter is a flexible modular approach allowing easy integration of an arbitrary number of modules.

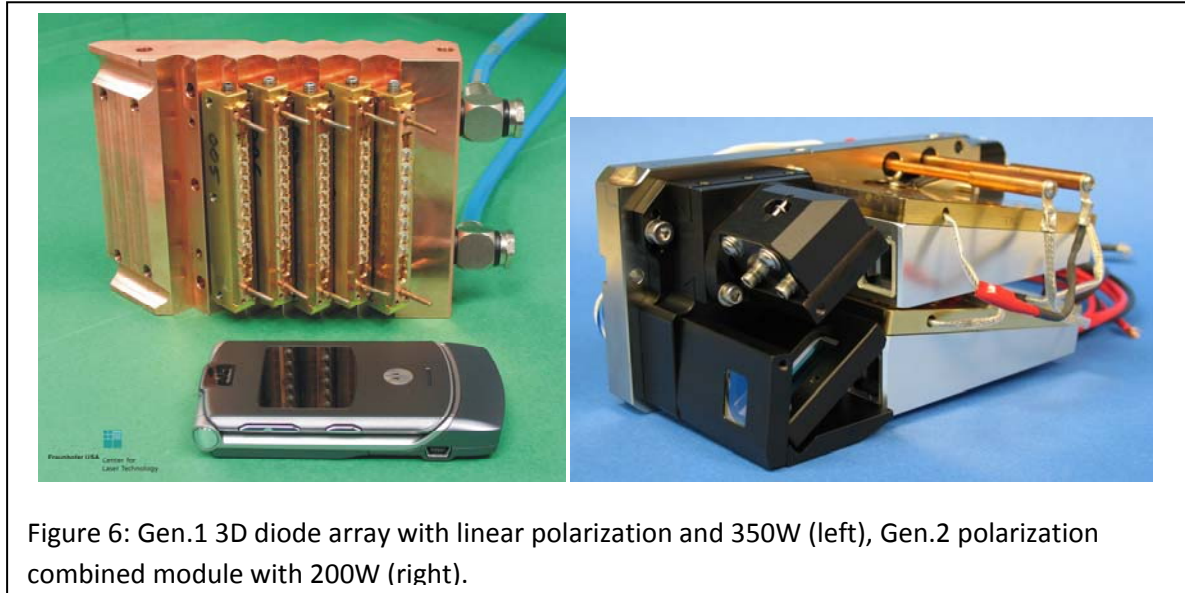


Figure 6: Gen.1 3D diode array with linear polarization and 350W (left), Gen.2 polarization combined module with 200W (right).

Fiber coupled turnkey systems with control were also developed. Gen.1 delivers 550W from the fiber and Gen. 2 delivers 700W from the fiber, both units at 976nm with 5nm linewidth. The Gen.1 turnkey system is about 3 times the size of the Gen.2 system.

Six systems based on Gen.1 design were installed (Fig.7), delivering a total of 2.1 kW from 6 200 μ m fiber, 0.2 NA. More than 4,000 operational hours were locked on these systems.

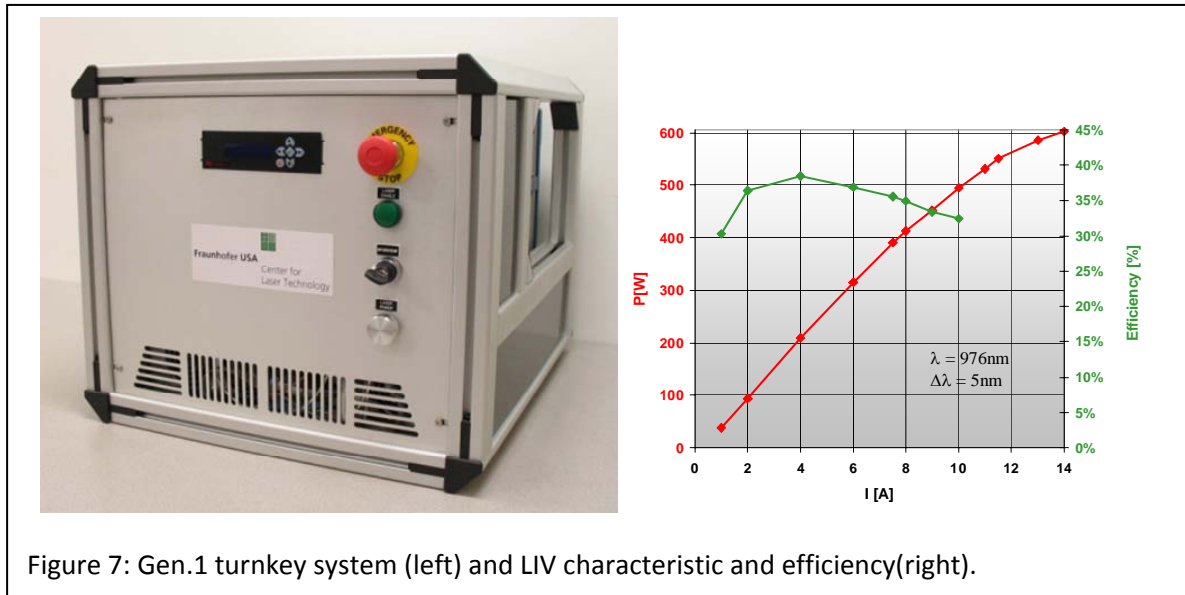


Figure 7: Gen.1 turnkey system (left) and LIV characteristic and efficiency(right).

The Gen.2 system has a unique motorized beam switch integrated, which allows to direct the light of five modules in either five individual 100 μ m fibers or optically stack the modules for delivery in a single 200 μ m fiber. A sixth module is also integrated into the turn key system (Fig.8). The user interface allows

individual control or simultaneous control of the six modules. 800W are obtained from the six 100 μ m fibers and 700W from the 200 μ m fiber (Fig.9). Three units are in the process of installation delivering a total of also 2.1 kW.

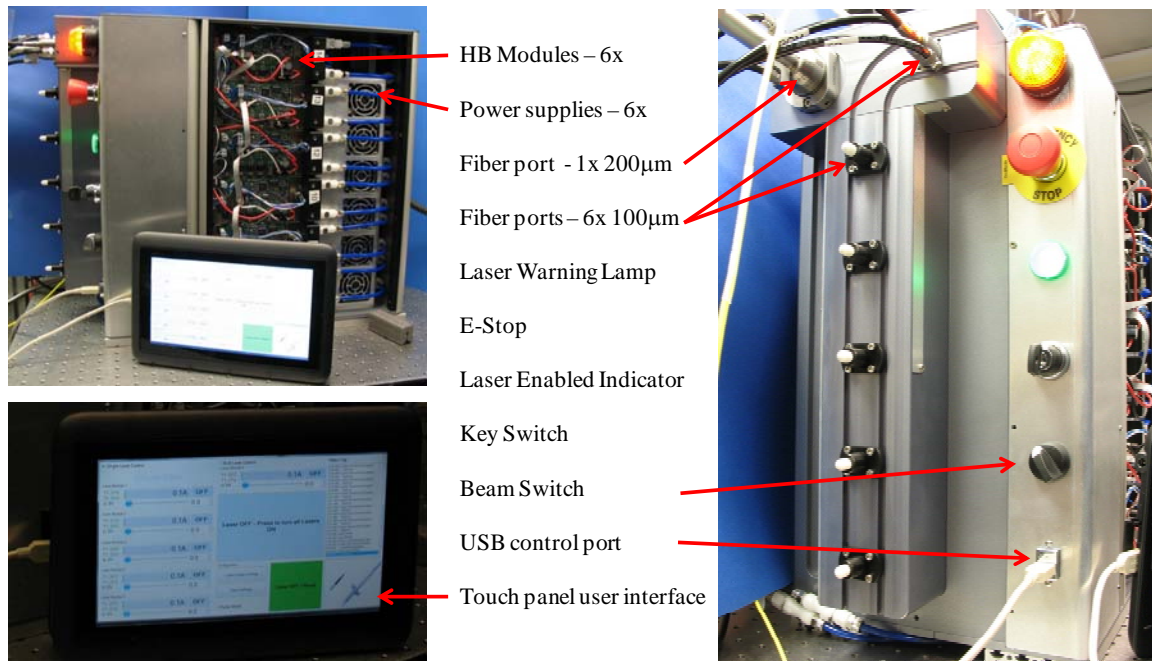


Figure 8: Gen.2 turnkey system with six 200W modules with integrated controller (upper left) and integrated beam switch for delivery in either six 100 μ m fibers or one 200 μ m fiber plus one 100 μ m fiber, all with 0.2 NA.

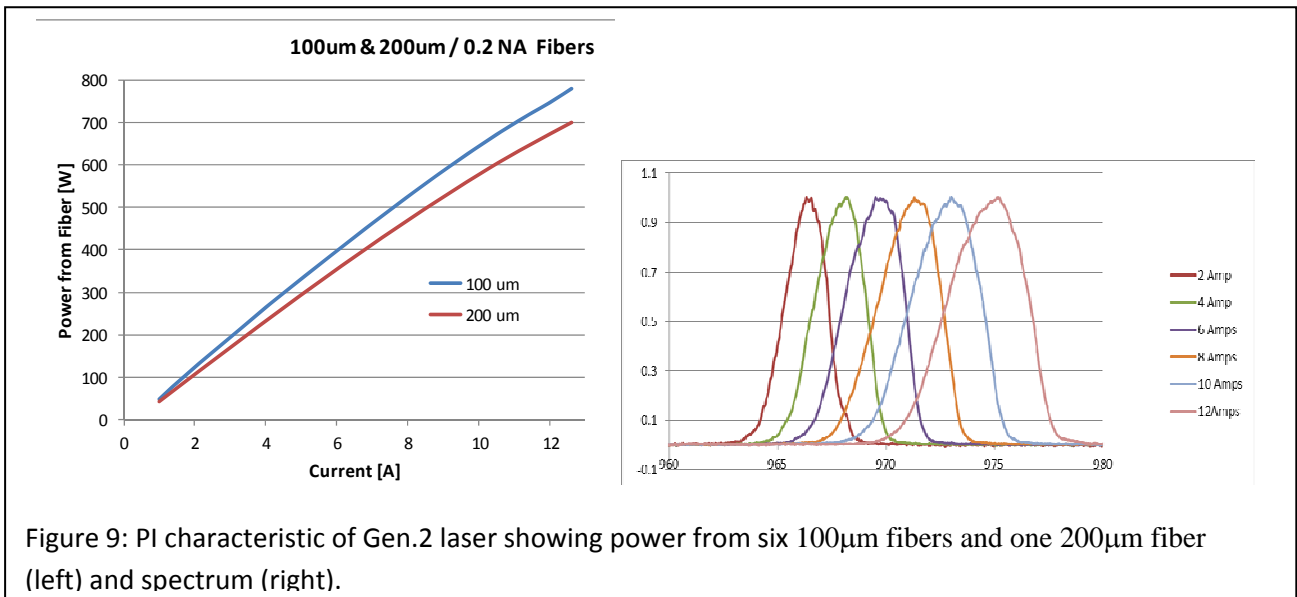


Figure 9: PI characteristic of Gen.2 laser showing power from six 100 μ m fibers and one 200 μ m fiber (left) and spectrum (right).

Appendix A

I. Additional Analysis and Derivation for Choosing the Helical Reference Frame in CCC Structure

In order to describe QPM conditions in CCC structures, it is necessary to investigate the eigenmodes in CCC structure. In the fixed laboratory reference frame with Cartesian coordinates $\{x, y, z\}$, whose z-axis is oriented along the central axis of CCC fiber, there is no eigenmode solution along the propagating direction (i.e. z-direction), because CCC structure has z-dependent variance. However, in this section it is shown that, in the helical reference frame with rotating helical coordinates $\{X, Y, Z\}$:

$$\begin{cases} X = x \cdot \cos \alpha z - y \cdot \sin \alpha z, \\ Y = x \cdot \sin \alpha z + y \cdot \cos \alpha z, \\ Z = z, \end{cases} \quad (S1)$$

, where the helical reference frame's rotation rate equals to the CCC rotation rate $\alpha = K$, the CCC structure becomes z-independent and, consequently, the eigenmode solutions can be obtained by applying conventional mode-solving techniques for electromagnetic wave propagating in a straight longitudinally invariant waveguide.

We can assume CCC fiber cladding is homogeneous and isotropic, and both the central core and side core are isotropic step index profiles. Then, in the fixed reference frame with Cartesian coordinates $\{x, y, z\}$, we have the dielectric permittivity tensor $\hat{\epsilon}(x, y, z)$ expressed as:

$$\hat{\epsilon}(x, y, z) = \begin{pmatrix} \epsilon_{clad} & 0 & 0 \\ 0 & \epsilon_{clad} & 0 \\ 0 & 0 & \epsilon_{clad} \end{pmatrix} + \begin{pmatrix} \Delta\epsilon_1(x, y) & 0 & 0 \\ 0 & \Delta\epsilon_1(x, y) & 0 \\ 0 & 0 & \Delta\epsilon_1(x, y) \end{pmatrix} + \begin{pmatrix} \Delta\epsilon_2(x, y, z) & 0 & 0 \\ 0 & \Delta\epsilon_2(x, y, z) & 0 \\ 0 & 0 & \Delta\epsilon_2(x, y, z) \end{pmatrix} \quad (S2)$$

, where ϵ_{clad} is the dielectric constant of the homogeneous cladding, $\Delta\epsilon_1(x, y)$ describes transversal profile of the cylindrically symmetric central core without z-dependence, and $\Delta\epsilon_2(x, y, z)$ describes three dimensional profile of the helical side core with z-dependence.

In general, it can be shown [A1, A2] that from the covariance of Maxwell's equations it follows that in any generalized coordinate system they can be expressed in a mathematical form identical to their expression in Cartesian coordinates, reference-frame difference being solely captured by the change in the tensor form of permittivity and permeability in these equations. Therefore, keeping the same mathematical form for Maxwell's equations, we have the new dielectric permittivity tensor $\hat{\epsilon}_{helical}(X, Y)$ in the helical reference frame expressed as:

$$\hat{\epsilon}_{helical}(X, Y) = \tilde{J} \cdot \hat{\epsilon}(x, y, z) \cdot \tilde{J}^T = \hat{\epsilon}_{helical}^{straight}(X, Y) + \hat{\epsilon}_{helical}^{rotate}(X, Y) \quad (S3)$$

$$\hat{\epsilon}_{helical}^{straight}(X, Y) = \begin{pmatrix} \epsilon_{clad} & 0 & 0 \\ 0 & \epsilon_{clad} & 0 \\ 0 & 0 & \epsilon_{clad} \end{pmatrix} + \begin{pmatrix} \Delta\epsilon_1(X, Y) & 0 & 0 \\ 0 & \Delta\epsilon_1(X, Y) & 0 \\ 0 & 0 & \Delta\epsilon_1(X, Y) \end{pmatrix} + \begin{pmatrix} \Delta\epsilon_2(X, Y) & 0 & 0 \\ 0 & \Delta\epsilon_2(X, Y) & 0 \\ 0 & 0 & \Delta\epsilon_2(X, Y) \end{pmatrix} \quad (S4)$$

$$\hat{\epsilon}_{helical}^{rotate}(X, Y) = [\epsilon_{clad} + \Delta\epsilon_1(X, Y) + \Delta\epsilon_2(X, Y)] \cdot \begin{pmatrix} Y^2\alpha^2 & -XY\alpha^2 & -Y\alpha \\ -XY\alpha^2 & X^2\alpha^2 & X\alpha \\ -Y\alpha & X\alpha & 0 \end{pmatrix} \quad (S5)$$

, where \tilde{J} and \tilde{J}^T are the Jacobian matrix [A2] and its transpose matrix of the coordinates transformation. For the central core, due to the rotational invariance of the cylindrical symmetry, the distribution remains exactly the same $\Delta\epsilon_1(X, Y) = \Delta\epsilon_1(x, y)$. For the side core, since helical coordinates X and Y are rotating following the same rotating distribution of the side core, the longitudinal variance of the side core in the helical coordinates disappears as $\Delta\epsilon_2(X, Y) = \Delta\epsilon_2(x, y, z = 0)$, which verifies the intuitive conclusion that the geometry of side core becomes “unwound” and should be represented by a straight and Z-axis independent waveguide. Instead, Eq. (S3), (S4) and (S5) indicate that the disappeared rotation effect in geometry is transferred into the dielectric permittivity tensor $\hat{\epsilon}_{helical}(X, Y)$, which has the contribution from two tensor terms in Eq. (S3): the first tensor term $\hat{\epsilon}_{helical}^{straight}(X, Y)$ is the part that acts exactly like a straight homogeneous isotropic fiber core, while the second tensor term $\hat{\epsilon}_{helical}^{rotate}(X, Y)$ is truly the rotation effect.

Now, we have two conclusions regarding the CCC structure in the helical reference frame. The first one is that, in the helical reference frame, the CCC structure becomes longitudinally invariant, which allows us applying conventional mode-solving techniques to find the eigenmodes for the CCC structure. Indeed, this is the main reason why choice of helical coordinates is advantageous here. By using standard finite-element-method (FEM) modal solver in a medium characterized by the permittivity tensor in Eq. (S3), we found CCC fiber modes numerically. This approach allows to find exact modal profiles and propagation constants (including imaginary parts which directly describe modal loss) of either individual CCC-structure waveguides or composite-modes of the complete structure. Examples of numerically calculated CCC-structure modes are shown in Fig. 1 in Ref. [A3]. The second conclusion is that, in Eq. (S3), the first tensor term $\hat{\epsilon}_{helical}^{straight}(X, Y)$ is essentially dominating the second term $\hat{\epsilon}_{helical}^{rotate}(X, Y)$, because the rotation of CCC structure is usually “slow”, in a sense that the helix pitch is in millimeters while the helix offset is usually in tens of micrometers. It means that we can first analytically solve the modal field for the first tensor term as in straight homogeneous isotropic fiber core, and then treat the second tensor term as perturbation and employ the couple mode equations to obtain the analytical modal solution for the total dielectric tensor. This is an analytical approach to solve for the eigenmodes in CCC structure.

The two approaches to obtain the eigenmode of CCC structure, namely numerical and analytical, are quantitatively giving exactly the same results in terms of both vector modal field distribution and propagation constants. Although the numerical approach with FEM mode solver is more rigorously

solving the Maxwell equations, the analytical approach is more insightful, because it gives us the analytical expression of the eigenmodes in CCC fibers, which is necessary to explain the QPM conditions.

II. Additional Analysis and Derivation for Analytical Expression of Eigenmodes in CCC Structure

As has been mentioned in last section, solving modal equations with the first tensor term $\hat{\epsilon}_{helical}^{straight}(X, Y)$ in Eq. (S3) leads to standard modal solutions of straight core fibers. For cylindrically symmetric fibers with step index profile, the analytical modal solutions for vector modal fields are well known: they are conventionally named as Transverse Electric modes designated as TE_{0m} , Transverse Magnetic modes designates as TM_{0m} , and so called Hybrid modes designated as HE_{nm} and EH_{nm} [A4 – A6] with indices n and m standing for azimuth and radial modal numbers $n = +1, +2, \dots$ and $m = +1, +2, \dots$. Each HE_{nm} or EH_{nm} mode is doubly-degenerate with respect to two orthogonal electric-field's azimuthal distributions. The electric field azimuthal distributions for each set of degenerate HE_{nm} modes are [A4 – A6]:

$$\begin{cases} HE_{nm}^o \\ HE_{nm}^e \end{cases}: \quad E_z \sim \begin{cases} \cos n\theta \\ \sin n\theta \end{cases} \hat{e}_z, E_x \sim \begin{cases} -\cos(n-1)\theta \\ -\sin(n-1)\theta \end{cases} \hat{e}_x, E_y \sim \begin{cases} \sin(n-1)\theta \\ -\cos(n-1)\theta \end{cases} \hat{e}_y, \quad n = +1, +2 \dots \quad (S6)$$

, and for each degenerate EH mode set are [A4 – A6]:

$$\begin{cases} EH_{nm}^o \\ EH_{nm}^e \end{cases}: \quad E_z \sim \begin{cases} \cos n\theta \\ \sin n\theta \end{cases} \hat{e}_z, E_x \sim \begin{cases} \cos(n+1)\theta \\ \sin(n+1)\theta \end{cases} \hat{e}_x, E_y \sim \begin{cases} \sin(n+1)\theta \\ -\cos(n+1)\theta \end{cases} \hat{e}_y, \quad n = +1, +2 \dots \quad (S7)$$

, where superscript “o” and “e” are used to designate two degenerate modes with “odd” oriented distribution (cosine function) and “even” oriented distribution (sine function). Although in the weakly guiding limit [A7], TE_{0m} modes and TM_{0m} modes have approximately the same propagation constants, they are essentially not degenerate and each is represented by a unique field distribution.

As has also been pointed out in last section, the second tensor term $\hat{\epsilon}_{helical}^{rotate}(X, Y)$ in Eq. (S3), namely the slow rotation effect, can be treated as a perturbation to the straight fiber modes solved with the first tensor term $\hat{\epsilon}_{helical}^{straight}(X, Y)$. Indeed, this perturbation will cause coupling between the degenerate pair of straight fiber modes, such as $HE_{nm}^{o,e}$ degenerate mode pair and $EH_{nm}^{o,e}$ degenerate mode pair, and this coupling is described by the following coupled-mode equations (CME) for the n -th order:

$$\begin{cases} \frac{\partial A_{c,s}^o}{\partial z} = i\beta_{c,s}^n A_{c,s}^o - A_{c,s}^e \cdot n\alpha \\ \frac{\partial A_{c,s}^e}{\partial z} = A_{c,s}^o \cdot n\alpha + i\beta_{c,s}^n A_{c,s}^e \end{cases} \quad (S8)$$

, where $A_{c,s}^o$ and $A_{c,s}^e$ are modal amplitudes for odd and even modes, and $\beta_{c,s}^n$ is the propagation constant of the n -th order degenerate pair. Subscripts “c” and “s” stand for “central core” and “side

core" respectively, since each core has its own set of CME. Different from the straight central core, the derivation from the second tensor term in Eq. (3S) shows that the off-center side core acquires a helical correction factor $\beta_s^n \cong \beta_{straight}^n \cdot \sqrt{1 + K^2 R^2}$, which is also quite intuitive when considering the projection of the helical path onto the z-axis. By diagonalizing the CME in Eq. (S8), we have the n -th order helically-symmetric modal solutions for both central and side core:

$$\vec{E}_{nm}^{\pm} = (\vec{E}_{nm}^o \pm j\vec{E}_{nm}^e) \cdot e^{-j(\beta_{c,s}^n \pm nK)z} \quad (S9)$$

Here we can see that, the degeneracy is broken, the degenerate modes are mixed, and we have a new set of modes designated as " \pm ", whose propagation constants also acquire additional increment $\Delta\beta = \pm nK$ for the n -th order.

By direct calculation it can be shown that electric-field's azimuthal dependence for HE_{nm}^{\pm} modes is:

$$E_z \sim e^{\pm jn\theta} \cdot \hat{e}_z, E_x \pm jE_y \sim e^{\pm j(n-1)\theta} \cdot [\hat{e}_x \pm j\hat{e}_y], n = +1, +2, \dots \quad (S10)$$

, and for EH_{nm}^{\pm} modes it is:

$$E_z \sim e^{\pm jn\theta} \cdot \hat{e}_z, E_x \pm jE_y \sim e^{\pm j(n+1)\theta} \cdot [\hat{e}_x \mp j\hat{e}_y], n = +1, +2, \dots \quad (S11)$$

, where \hat{e}_x and \hat{e}_y are the unit vectors along X and Y axes respectively. It is well known that the term $e^{\pm j\ell\theta}$ describes an optical vortex carrying optical orbital angular momentum (OAM) [A8 – A10], and the term $\hat{e}_{\pm} = \hat{e}_x \pm j\hat{e}_y$ describes circular polarized light carrying spin-angular momentum (SAM) [A8, A9, A11]. Since the azimuthal angle and axial propagation are coupled in the CCC helical structure $\theta = \theta_0 + Kz$, the additional propagation constant increment $\Delta\beta$ due to OAM is $\pm(n-1)K$ for HE_{nm}^{\pm} modes and $\pm(n+1)K$ for EH_{nm}^{\pm} modes, and similarly additional propagation constant increment $\Delta\beta$ due to SAM is $\pm K$ for HE_{nm}^{\pm} modes and $\mp K$ for EH_{nm}^{\pm} modes. Therefore, as the summation of OAM-induced $\Delta\beta$ and SAM-induced $\Delta\beta$, the total additional propagation constant increment $\Delta\beta$ induced by the total angular momentum (OAM+SAM) is always equal to $\pm nK$ for n -th order HE_{nm}^{\pm} or EH_{nm}^{\pm} modes, which is derived in Eq. (S9). Rigorously solving modal equations in a helical reference frame with FEM modal solver has confirmed that total angular momentum induced $\Delta\beta$ for HE_{nm}^{\pm} and EH_{nm}^{\pm} modes is always equal to $\pm nK$, which is consistent with the OAM and SAM contributions. These results are summarized in Table (S1).

Mode Azimuth Number n	$n = 0$		$n = 1, 2, 3, \dots$			
Fiber Mode Designation	TE_{0m}	TM_{0m}	HE_{nm}^+	HE_{nm}^-	EH_{nm}^+	EH_{nm}^-
$\Delta\beta$ due to OAM	0	0	$(n - 1) K$	$-(n - 1) K$	$(n + 1) K$	$-(n + 1) K$
$\Delta\beta$ due to SAM	0	0	K	$-K$	$-K$	K
Total $\Delta\beta$ due to OAM+SAM	0	0	$n K$	$-n K$	$n K$	$-n K$

Table S1: Fiber modes designation and their propagation constant increments $\Delta\beta$ due to Orbital Angular Momentum (OAM), Spin (Polarization) Angular Momentum (SAM), and total angular momentum (OAM+SAM). Note, that $n = 0$ corresponds to TE_{0m} modes and TM_{0m} modes which are azimuthally invariant but with no optical momentum, and that modes with $n = 1$ (which include fundamental HE_{11} modes) carry only spin-angular momentum.

III. Additional Analysis and Derivation of General Quasi-Phase-Matching (QPM) Conditions

For the sake of both mathematical expression convenience and practical experiment use, it is useful to group TE_{0m} modes, TM_{0m} modes, and HE_{nm} modes and EH_{nm} modes into so-called LP_{lm} modes (LP stands for “Linearly Polarized”) as shown in Fig. 13 . The LP_{lm} modes are customarily used in designating weakly-guiding cylindrically-symmetric fiber modes [A4, A5], which are groups of TE_{0m} modes, TM_{0m} modes, and HE_{nm} and EH_{nm} hybrid modes that become degenerate (their propagation constants β are equal) in the weakly guiding limit [A7].

LP modes	Azimuthal modal number l	Corresponding hybrid helically-symmetric modes
LP_{lm}	0	$HE_{1,m}^+$
		$HE_{1,m}^-$
	1	$HE_{2,m}^+$
		TE_{0m}
		TM_{0m}
		$HE_{2,m}^-$
	$l > 1$	$HE_{l+1,m}^+$
		$EH_{l-1,m}^+$
		$EH_{l-1,m}^-$
		$HE_{l+1,m}^-$

Table (S2): Group Rules of LP_{lm} : Three different grouping scenarios depending the l -value of LP_{lm} mode.

This grouping into LP_{lm} modes in a CCC structure remains valid and has been summarized in Table (S2), where helically-symmetric HE_{nm}^\pm and EH_{nm}^\pm modes are used. However, it is important to note that there is an essential distinction between the LP_{lm} modes in CCC structures and in conventional cylindrical fibers. Indeed, by comparing Table (S1) and Table (S2), one can see that the degeneracy within the LP_{lm} mode group in CCC structures is broken in the helical reference frame, and when they interact with each other, the modes carrying different orbital- and spin-angular momentum combinations (in terms of magnitudes and polarities) in one LP_{lm} mode group in CCC structures will act as they are not degenerate any more. Of course, when no interaction between the cores of CCC structure is considered (namely outside quasi-phase matched resonances), modal degeneracy within each core is still valid.

In order to determine QPM conditions between modes in a CCC structure, we have developed a rigorous analytical theory based on Maxwell's equations in helical reference frame, with which we have

formulated the coupled-mode equations (CME) describing inter-core coupling between different helically-symmetric vector modes from Table (S1) and Table (S2), and derived exact QPM conditions for each interacting modal pair. The derived expressions for these helically-symmetric vector modes turn out to be quite complicated. However, we discovered that the QPM expressions could be quite simple if interacting modes are grouped according to LP -grouping prescription in Table (S2). Essentially, all possible QPM conditions of coupling between LP_{lm} modal groups involve all possible combinations of orbital- and spin- angular momentum values and polarities within each LP_{lm} group. In terms of propagation constant and angular momentum matching, this can be expressed as following:

$$\beta_{l_1 m_1} - \beta_{l_2 m_2} \cdot \sqrt{1 + K^2 R^2} - \Delta m \cdot K = 0 \quad (\text{S12})$$

, where $\beta_{l_1 m_1}$ and $\beta_{l_2 m_2}$ are the propagation constants of $LP_{l_1 m_1}$ and $LP_{l_2 m_2}$ in straight central and side cores respectively, and $\sqrt{1 + K^2 R^2}$ is a helical correction factor for the side core. The parameter Δm follows $\Delta m = \Delta l + \Delta s$: the values of Δl run through four possible combinations $\Delta l = \pm l_1 \pm l_2$, and the values of Δs run through five possible integers $\Delta s = -2, -1, 0, +1, \text{ and } +2$. For example, interaction between central-core LP_{01} group and side core LP_{11} group is described by $\Delta m = -3, -2, -1, 0, +1, +2, +3$, while the same situation but with side core LP_{21} group gives $\Delta m = -4, -3, -2, -1, 0, +1, +2, +3, +4$. Both these interaction examples correspond to experimentally verified situation shown in Fig. 13.

Physical origin of the multitude of QPM resonances illustrated in Eq. (S12) is two-fold: First, it is actually two groups of modes that are interacting with each other in terms of LP_{lm} modes, as has been discussed above. Second, there are three different types of perturbations that are causing three different types of coupling between center and side core modes, which can be theoretically studied by performing detailed finite-element analysis of induced birefringence in CCC fiber. By comparing theoretical results with the experimental observations, we achieve the following conclusions: The first type of perturbation is simply a perturbation of a mode by the presence of another core, i.e. center-core modes are perturbed by the helical side core and side-core modes are perturbed by the central core. This causes coupling between the modes with the same circular polarization, i.e. RCP to RCP and LCP to LCP. In the above formula Eq. (S12), this corresponds to Δm values with $\Delta s = 0$. The second type of perturbation arises from local linear birefringence created in the spacing between the two cores due to the difference in the thermal expansion between the two cores and the cladding during the fiber draw process. This perturbation causes coupling between orthogonally polarized modes, i.e. RCP to LCP and vice versa. In Eq. (S12), this corresponds to Δm values with $\Delta s = -2$ and $+2$. The third type of perturbation is associated with the local “shear” birefringence created in the spacing between the two cores due to the spinning of a hot fiber perform during CCC fiber draw. This perturbation causes mixing between longitudinal and transverse modal field components (similar to the case of a twisted cylindrically-symmetric conventional fiber [A12] and is described by Δm values with $\Delta s = -1$ and $+1$.

References for Appendix A

- [A1] J. L. Wilson et al., IEEE Trans. Microwave Theory Tech. 57,130 (2009).
- [A2] A. Nichlet et al., Eur. Phys. J. Appl. Phys. 28, 153 (2004).
- [A3] Xiuquan Ma, Chi-Hung Liu, Guoqing Chang, and Almantas Galvanauskas, "Angular-momentum coupled optical waves in chirally-coupled-core fibers," Opt. Express, 19, 26515-26528 (2011).
- [A4] E. Snitzer, J. Opt. Soc. Am. 51, 491 (1961).
- [A5] J. A. Buck, Fundamentals of Optical Fibers, 2nd Edition (Wiley, New Jersey, 2004).
- [A6] Katsunari Okamoto, Fundamentals of Optical Waveguides, 2nd Edition (Academic Press, MA, 2006).
- [A7] D. Gloge, Appl. Optics 10, 2252 (1971).
- [A8] L. Allen et al., Optical Angular Momentum (I.O.P. Publishing, London, 2003).
- [A9] L. Marrucci et al., Phys. Rev. Lett. 96, 163905 (2006).
- [A10] L. Allen et al., Phys. Rev. A 45, 8185 (1992).
- [A11] R. A. Beth, Phys. Rev. 50, 115 (1936).
- [A12] R. Ulrich, and A. Simon, Appl. Optics 18, 2241 (1979).